

See discussions, stats, and author profiles for this publication at: <https://www.researchgate.net/publication/315655740>

Simulink model development, validation and analysis of high altitude airship

Technical Report · March 2017

DOI: 10.13140/RG.2.2.11844.22400

CITATIONS

2

READS

10,811

2 authors:



Raghavendra P. Kukillaya

Indian Institute of Technology Kanpur

12 PUBLICATIONS 222 CITATIONS

[SEE PROFILE](#)



Abhay Pashikar

National Aerospace Laboratories

87 PUBLICATIONS 499 CITATIONS

[SEE PROFILE](#)

Some of the authors of this publication are also working on these related projects:



Intelligent Aircraft Flight Controller Design [View project](#)



Dynamics of Insect Running [View project](#)



Simulink model development, validation and analysis of high altitude airship

RAGHAVENDRA KUKILAYA, ABHAY PASHILKAR
Flight Mechanics and Control Division

PD-FMC/2017/1000
March 2017



ISO 9001:2008
CERTIFIED

वैज्ञानिक तथा औद्योगिक अनुसंधान परिषद्
Council of Scientific & Industrial Research
राष्ट्रीय वांतरिक्ष प्रयोगशालाएं
National Aerospace Laboratories
बैंगलूरु/ Bangalore-560 017, भारत/ India

Simulink model development, validation and analysis of high altitude airship

Contents

1. Introduction
2. System-level mathematical modelling of a High Altitude Airship
 - 2.1. Airship hull geometry
 - 2.2. Aerostatics
 - 2.3. Aerodynamics
 - 2.4. Apparent mass and inertia
 - 2.5. Equations of motion
 - 2.6. Equations of motion in the Earth-Centered Inertial (ECI) frame
 - 2.7. External environment: solar radiation
 - 2.8. External environment: atmosphere, wind and turbulence
 - 2.9. Power and Propulsion System (PPS): PV arrays
 - 2.10. PPS: Electrolyser, storage, and fuel cell
 - 2.11. PPS: Electric motor and gearbox
 - 2.12. PPS: Propeller design and dynamics
3. Simulink model development
 - 3.1. Airship flight dynamics: subsystems
 - i. Forces and Moments: Aerodynamics
 - ii. Forces and Moments: Buoyancy and Gravity
 - iii. Forces and Moments: Propulsive components
 - iv. Forces and Moments: Coriolis and Centrifugal components
 - v. Inertia Coefficients
 - vi. Mass and Inertia
 - vii. Mass and Inertia matrix
 - viii. Equations of motion
 - ix. Quaternion kinematics and Angular transformations
 - x. Earth and Navigation (Flat-Earth case)
 - xi. Velocity transformation: Body to Wind axes
 - xii. Atmosphere
 - xiii. System integration (Flat-Earth case)
 - 3.2. Solar radiation and PV arrays: subsystems

- i. Declination angle
 - ii. Sunrise and Sunset timings
 - iii. Solar Intensity
 - iv. Variation with altitude
 - v. Sun position
 - vi. Transformation: ENU to NED to Body frame
 - vii. PV array calculations
 - viii. Shadow model
 - ix. System integration
- 3.3. Propulsion (including storage): subsystems
- i. Electrolyser, storage, and fuel cell
 - ii. Motor and propeller system
 - iii. Smaller / Larger motor-propeller unit
 - iv. Propeller operating conditions
 - v. Motor dynamics (Electrical)
 - vi. Motor (Mechanical) and Propeller dynamics
 - vii. Blade-pitch dynamics
 - viii. Propeller characteristics
 - ix. System integration
4. System integration, dynamic analysis and control
 5. Conclusions and Future Work
 6. Appendix: system parameters and data
 7. References

1. Introduction

In recent years, due to the technology development in various areas, flight at high altitudes (18 km and higher) for an extended duration of time (months to years) has been considered a subject of interest. Potential applications include surveillance, communication, and remote sensing purposes. An airship is a unique candidate for such a high altitude long endurance flight vehicle, mainly due to the following two reasons: a) airships, unlike aircrafts, generate lift through buoyancy effect, and not through aerodynamics. This means that, to remain aloft, an airship need not be in motion; b) an airship also has the ability to carry heavy payloads with minimal volume constraints.

A High Altitude Airship (HAA) is designed to perform roving and hovering, and hence finds its potential in the areas of surveillance, communication, and remote sensing. It has several advantages over satellites such as it can maintain a geostationary location much closer to the earth (geostationary satellites are about 1700 times farther away) and can match any longitude and latitude on the globe. Satellites in low orbit can also do the job but a constellation of satellites is required which in turn requires huge investment. In addition to this, HAA can be grounded, repaired, and returned to the mission once again, or with a new payload for another mission.

One of the main daunting tasks in realizing such a flight vehicle is the actual design of an HAA which has to be feasible, considering the various constraints, and also, should meet the specified user requirements. As per the requirement, what we are looking at is to develop an almost-fully autonomous stratospheric airship, which has to operate at altitudes ranging between 18 and 22 km using power from a renewable source of energy and a propulsion system which can efficiently run at those altitudes.

In this work, we develop a fairly-detailed system-level mathematical model of a High Altitude Airship (HAA) considering all the essential subsystems, and successfully implement it using the MATLAB-Simulink simulation framework. This model/simulation works as a powerful design/analysis tool which can be used to study/design/verify an entire HAA configuration or any of its subsystems/features such as power and propulsion system, flight dynamics, stability, and control, feasibility and sizing issues, and aerostatic and aerodynamic performance. Here, solar energy is the renewable source. The required power is derived from solar arrays installed on the surface of the airship hull. The operating altitude is around 21 km above the earth's surface where there are no clouds to block the sunlight and wind speeds are relatively lower.

In a previous project report [1], the outcome of a detailed literature survey on airships has been captured, in the form of different mathematical models and their technical descriptions, for the various essential components of a high altitude airship (HAA) system. Subsequently, Simulink models have been developed for each component and integrated together to build the full HAA dynamic system. While building these Simulink models, many of the mathematical models have been updated or modified in order to obtain correct dynamic behaviour and performance of these subsystems. The detailed description of each model from

the previous report has been reproduced here in Section 2, along with the essential details of each model's modifications. Development of the Simulink models, their validation results, and individual integration of the three dynamic subsystems of the HAA system, i.e. Flight Dynamics, Power and Propulsion, is the subject matter of Section 3. The step-by-step procedure taken towards building the full integrated system dynamics model and the results obtained from the dynamics and control analysis are given in Section 4. Conclusions from this project and future directions are discussed in Section 5. Section 6, which is the Appendix, contains all the required details of various system equations, parameters, and data. All the publications that have been referred to in the main text are included in Section 7.

2. System-level mathematical modelling of a high altitude airship

In this section the mathematical models of various subsystems, which are used in this work to build a system-level simulation of a High Altitude Airship (HAA), are described. In an earlier report [1], the details of each of these models have been discussed. Here the essential model details from that report are reproduced along with the specific modifications that these models have undergone during the Simulink implementation. For further details on any of these models, please refer to [1]. The particular HAA system, which is being simulated in this project, has the following design characteristics:

- 1) The hull is modeled as two, axisymmetric ellipsoid halves (Figure 1). Each ellipsoid has the same semi-minor axis, b , but different semi-major axes, a_1 and a_2 .
- 2) The other major structural parts of the airship are a hanging gondola, power and propulsion system, and tail fins for stability and control.
- 3) The power and propulsion system (propulsor) chosen is a photovoltaic/fuel-cell system powering electric motors to drive a propeller for generating thrust.
- 4) As per the design, thin-film solar arrays are used, and they are installed on the upper surface of the airship hull on the envelope material itself.
- 5) Four propulsor units have been chosen for this configuration. Each propulsor unit is a self-sufficient system, i.e. it receives 25% of the power produced by the solar arrays, has an electrolyzer to convert this electric power into Hydrogen and Oxygen, which in turn are sent to the storage tanks. Note that these storage tanks are also a part of the propulsor unit, and whenever there is a power demand from the control system for propulsion or for payload requirements, a fuel cell system starts converting the stored H_2 and O_2 into electric power either for the motor to run the propellers or for running some payload unit.

In the rest of this section, mathematical models of all the various components of the airship are described in short, focusing on the essential details and modifications.

2.1. Airship hull geometry

First of all, the particular shape or geometry of the airship, to be simulated, has to be chosen. Among various options, the simplest airship can have a spherical, an ellipsoidal or a double-ellipsoidal geometry.

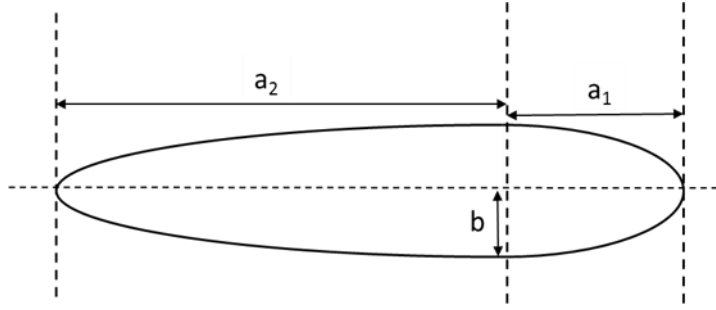


Figure 1: 2D view of a double-ellipsoidal hull geometry

Here the double-ellipsoidal geometry, shown in Figure 1, is chosen for the airship hull. It consists of two, axis-symmetric ellipsoidal halves. Each ellipsoid has the same semi-minor axis, b but different semi-major axes, a_1 and a_2 ($a_2 > a_1$). The maximum diameter of this shape is $D = 2b$, and the length is $L_h = a_1 + a_2$. Volume of an airship hull with such a shape is given by the following formula.

Equation 1: Volume of a double-ellipsoidal airship hull

$$\Lambda = \frac{2}{3}\pi b^2(a_1 + a_2)$$

2.2. Aerostatics

In this work, since the primary objective is to achieve successful operation of the airship system (stable hover and flying at speeds ranging up to 55 m/s) at an altitude of 21 km, the modelling of ballonets has not been included. It is assumed that the entire hull volume is filled with helium gas, and an upward buoyancy force, corresponding to this volume and air density at an altitude of 21 km, is acting on the airship.

2.3. Aerodynamics

In order to develop an aerodynamic model of an airship, the double-ellipsoidal geometry of Figure 1 has been used to define the shape of the airship hull. By measuring backwards from the airship's nose, the centre of volume (CV or centroid of volume) location along the centerline ($y_{cv} = 0$) is given as $d_{cv} = a_1 + \frac{3}{8}(a_2 - a_1)$. Aerodynamic forces (X , Y and Z) and moments (L , M and N) acting on the airship are defined about a body-fixed frame of reference, centered at the CV, as shown in Figure 2. Thus, the aerodynamic model presented here ([2], [6]) includes expressions for these 3 forces and 3 moments which are acting on an axis-symmetric double-ellipsoidal airship hull with 4 equally-sized tail fins – 2 horizontal and 2 vertical. The equations are valid only for un-separated flow.

The geometric configuration of the complete airship with fins and gondola is shown in Figure 2. It is flying at an air-speed V_o , an angle of attack α , and sideslip β . The forces and moments on the hull are evaluated from the nose to the start of the fins. Aft of this point, the hull and fins are evaluated together. The origin of the body frame is located at the airship's centre of volume (CV). The equations for the aerodynamic forces and moments are the same

as given in the previous report [1] except for the axial force equation. The X force equation has been modified as below to include a drag term due to β .

Equation 2: Expression for axial force (X)

$$X = \frac{1}{2} \rho V_0^2 \left[C_{X1} \cos^2 \alpha \cos^2 \beta + C_{X2} \sin 2\alpha \sin \frac{\alpha}{2} + C_{X3} \sin 2\beta \sin \frac{\beta}{2} \right]$$

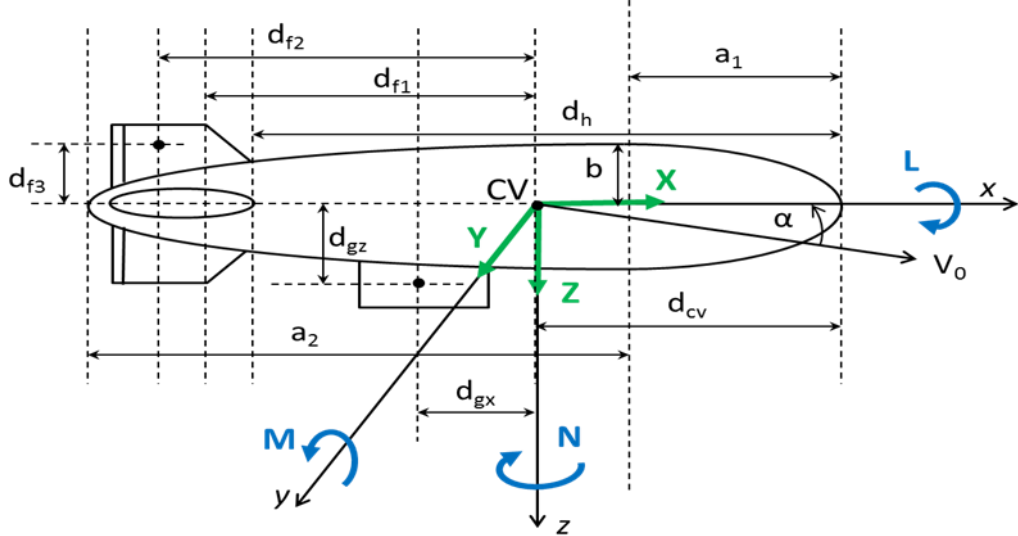


Figure 2: Steady-state aerodynamic model of an airship [2]

Let δ_{RUDT} and δ_{RUDB} indicate the deflections of the top and bottom trailing-edge flaps of the rudder. Similarly, let δ_{ELVL} and δ_{ELVR} be the deflections of the left and right trailing-edge flaps of the elevator. The other five equations for the aerodynamic forces and moments are added below.

Equation 3: Expression for lateral force (Y)

$$Y = \frac{1}{2} \rho V_0^2 C_Y = \frac{1}{2} \rho V_0^2 \left[C_{Y1} \cos \frac{\beta}{2} \sin 2\beta + C_{Y2} \sin 2\beta + C_{Y3} \sin \beta \sin |\beta| + C_{Y4} (\delta_{RUDT} + \delta_{RUDB}) \right]$$

Equation 4: Expression for normal force (Z)

$$Z = \frac{1}{2} \rho V_0^2 C_Z = \frac{1}{2} \rho V_0^2 \left[C_{Z1} \cos \frac{\alpha}{2} \sin 2\alpha + C_{Z2} \sin 2\alpha + C_{Z3} \sin \alpha \sin |\alpha| + C_{Z4} (\delta_{ELVL} + \delta_{ELVR}) \right]$$

Equation 5: Expression for rolling moment (L)

$$L = \frac{1}{2} \rho V_0^2 [C_{L1} (\delta_{ELVL} - \delta_{ELVR} + \delta_{RUDB} - \delta_{RUDT}) + C_{L2} \sin \beta \sin |\beta|]$$

Equation 6: Expression for pitching moment (M)

$$M = \frac{1}{2} \rho V_0^2 C_M = \frac{1}{2} \rho V_0^2 \left[C_{M1} \cos \frac{\alpha}{2} \sin 2\alpha + C_{M2} \sin 2\alpha + C_{M3} \sin \alpha \sin |\alpha| + C_{M4} (\delta_{ELVL} + \delta_{ELVR}) \right]$$

Equation 7: Expression for yawing moment (N)

$$N = \frac{1}{2} \rho V_0^2 C_N = \frac{1}{2} \rho V_0^2 \left[C_{N1} \cos \frac{\beta}{2} \sin 2\beta + C_{N2} \sin 2\beta + C_{N3} \sin \beta \sin |\beta| + C_{N4} (\delta_{RUDT} + \delta_{RUDB}) \right]$$

The aerodynamic coefficients are direct functions of the airship geometry. Each of these coefficients is defined below in tabular form (**Table 1**), and the parameters appearing in these coefficient equations are defined in **Table 2**. Among the expressions given below in **Table 1** for various force and moment coefficients, one has been corrected as given below.

Equation 8: Modification in the first moment coefficient (Pitch and Yaw)

$$C_{M1} = -C_{N1} = (k_1 - k_2) I_3 \eta_h S_h (a_1 + a_2)$$

Table 1: Definition of aerodynamic coefficients

	Equation no.	Aerodynamic coefficients	Definition (in terms of airship geometry and other parameters)
Force coefficients	1	C_{X1}	$-[C_{Dh_0} S_h + C_{Df_0} S_f + C_{Dg_0} S_g]$
	2	$C_{X2} = C_{Y1} = C_{Z1}$	$(k_2 - k_1) I_1 \eta_h S_h$
	3	$C_{Y2} = C_{Z2}$	$-\frac{1}{2} \left(\frac{\partial C_L}{\partial \alpha} \right)_f \eta_f S_f$
	4	C_{Y3}	$-[C_{Dch} J_1 S_h + C_{Dcf} S_f + C_{Dcg} S_g]$
	5	$C_{Y4} = C_{Z4}$	$-\frac{1}{2} \left(\frac{\partial C_L}{\partial \delta} \right)_f \eta_f S_f$
	6	C_{Z3}	$-[C_{Dch} J_1 S_h + C_{Dcf} S_f]$
Moment coefficients	7	C_{L1}	$\left(\frac{\partial C_L}{\partial \delta} \right)_f \eta_f S_f d_{f3}$
	8	C_{L2}	$-C_{Dcg} S_g d_{gz}$
	9	C_{M1}	$(k_1 - k_2) I_3 \eta_h S_h (a_1 + a_2)$
	10	C_{M2}	$-\frac{1}{2} \left(\frac{\partial C_L}{\partial \alpha} \right)_f \eta_f S_f d_{f1}$
	11	C_{M3}	$-[C_{Dch} J_2 S_h (a_1 + a_2) + C_{Dcf} S_f d_{f2}]$
	12	C_{M4}	$-\frac{1}{2} \left(\frac{\partial C_L}{\partial \delta} \right)_f \eta_f S_f d_{f1}$
	13	C_{Nj}	$-C_{Mj}$

Table 2: Definition of parameters which appear in the aerodynamic coefficient equations

Parameter	Definition
C_{Dh_0}	Zero-incidence drag coefficient for hull
C_{Df_0}	Zero-incidence drag coefficient for fin
C_{Dg_0}	Zero-incidence drag coefficient for gondola
C_{Dch}	Cross-flow drag coefficient for hull
C_{Dcf}	Cross-flow drag coefficient for fins
C_{Dcg}	Cross-flow drag coefficient for gondola
$\left(\frac{\partial C_L}{\partial \alpha}\right)_f$	Derivative of fin-lift coefficient with respect to the angle-of-attack at zero incidence
$\left(\frac{\partial C_L}{\partial \delta}\right)_f$	Derivative of fin-lift coefficient with respect to the flap deflection angle
S_h	Hull reference area, $\Lambda^{2/3}$
S_f	Fin reference area
S_g	Gondola reference area
d_{f1}	x -distance from origin to aerodynamic center of fins
d_{f2}	x -distance from origin to geometric center of fins
d_{f3}	y, z -distance from origin to geometric center of fins
d_{gx}	x -distance from origin to geometric center of gondola
d_{gz}	z -distance from origin to geometric center of gondola
d_h	Length of the hull from its nose up to the leading edge of the fins
η_f	Fin efficiency factor accounting for the effect of the hull on the fins
η_h	Hull efficiency factor accounting for the effect of the fins on the hull
a_1	Semi-major axis of the front half-ellipsoid
a_2	Semi-major axis of the rear half-ellipsoid
b	Semi-minor axis of both the ellipsoid halves
k_1, k_2, k_3	Inertia factors for given hull geometry
I_1, I_3, J_1, J_2	Specific integrals to be evaluated over the surface of the airship hull

The variables k_1 (for translational motion in x direction), k_2 (for translational motion in y or z direction) and k_3 (for rotational motion about y or z axis) are the inertia factors for the given double-ellipsoidal hull geometry (Figure 2). The inertia factors for a single axisymmetric ellipsoid are pure functions of the semi-major axis, a and semi-minor axis, b . A complete derivation of these factors may be found in a 1926 NACA report by Tuckerman [7]. Here, the same results are adopted for the double-ellipsoid by defining a as the mean value of a_1 and a_2 . First, the following parameters are defined:

Equation 9: Definition of parameters to be used in the expressions for inertia factors

$$e = \sqrt{1 - \left(\frac{b}{a}\right)^2}$$

$$\alpha_0 = \left(\frac{1-e^2}{e^3} \right) \left[\log \left(\frac{1+e}{1-e} \right) - 2e \right]$$

$$\beta_0 = \frac{1}{e^2} - \left(\frac{1-e^2}{2e^3} \right) \log \left(\frac{1+e}{1-e} \right)$$

Using these parameters, the inertia factors for this mean ellipsoid are given by the following expressions.

Equation 10: Computation of inertia factors

$$k_1 = \frac{\alpha_0}{2 - \alpha_0}$$

$$k_2 = \frac{\beta_0}{2 - \beta_0}$$

$$k_3 = \frac{1}{5} \times \frac{(b^2 - a^2)^2 (\alpha_0 - \beta_0)}{2(b^2 - a^2) + (b^2 + a^2)(\beta_0 - \alpha_0)}$$

Also, the surface integrals I_1 , I_3 , J_1 and J_2 are defined as follows:

Equation 11: Definition of surface integrals

$$I_1 = \frac{1}{S_h} \int_{-a_1}^{d_h - a_1} \frac{dA(\zeta)}{d\zeta} d\zeta$$

$$I_3 = \frac{1}{S_h L_h} \int_{-a_1}^{d_h - a_1} \zeta \frac{dA(\zeta)}{d\zeta} d\zeta$$

$$J_1 = \frac{1}{S_h} \int_{-a_1}^{d_h - a_1} 2r(\zeta) d\zeta$$

$$J_2 = \frac{1}{S_h L_h} \int_{-a_1}^{d_h - a_1} 2r(\zeta) \zeta d\zeta$$

Here $A(\zeta)$ is area and $r(\zeta)$ is radius of the airship hull's circular cross-section at each ζ , where ζ is measured backwards from the nose ($\zeta = -a_1$) to the leading edge of the fins ($\zeta = d_h - a_1$). Using the double-ellipsoid geometry, the solutions to these integrals are expressed as analytical functions of the geometry parameters.

Equation 12: Solutions to the integrals expressed as analytical functions

$$I_1 = \frac{\pi b^2}{\Lambda^{\frac{2}{3}}} (1 - f^2)$$

$$I_3 = \frac{\pi b^2}{3L_h \Lambda^{\frac{2}{3}}} (a_1 - 2a_2 f^3 - 3a_1 f^2) - \frac{d_{cv}}{L_h} I_1$$

$$J_1 = \frac{b}{2\Lambda^{\frac{2}{3}}} \left(a_1 \frac{\pi}{2} + a_2 f \sqrt{1 - f^2} + 2a_2 \sin^{-1}(f) \right)$$

$$J_2 = J_1 \frac{a_1 - d_{cv}}{L_h} + \frac{2b}{3L_h\Lambda^{\frac{2}{3}}} \left(a_2^2 - a_1^2 - a_2^2(1 - f^2)^{\frac{3}{2}} \right)$$

Here Λ is the volume of the airship hull, $d_{cv} = a_1 + \frac{3}{8}(a_2 - a_1)$ is the center of volume (CV) location along the centerline ($y_{cv} = 0$) measured backwards from the nose, the variable $f = (d_h - a_1)/a_2$, d_h is the length of the hull up to the leading edge of the fins, and $L_h = a_1 + a_2$ is the total length of the hull. The values of various aerodynamic parameters are given in the Appendix (Section 6).

During the Simulink model development, **Equation 3**, **Equation 4**, **Equation 6** and **Equation 7** have been further modified to include damping terms as shown in the expressions given below. The variables q and r are the airship pitch and yaw angular rates, respectively.

Equation 13: Modification of yaw force

$$Y' = \frac{1}{2}\rho V_0^2 C_Y + \frac{1}{4}\rho V_0 S_h (a_1 + a_2) C_{Y_r} r$$

Equation 14: Modification of normal force

$$Z' = \frac{1}{2}\rho V_0^2 C_Z + \frac{1}{4}\rho V_0 S_h (a_1 + a_2) C_{Z_q} q$$

Equation 15: Modification of pitching moment

$$M' = \frac{1}{2}\rho V_0^2 C_M + \frac{1}{4}\rho V_0 S_h (a_1 + a_2)^2 C_{M_q} q$$

Equation 16: Modification of yawing moment

$$N' = \frac{1}{2}\rho V_0^2 C_N + \frac{1}{4}\rho V_0 S_h (a_1 + a_2)^2 C_{N_r} r$$

2.4. Apparent mass and inertia

Introduction

A body in motion, even in an ideal fluid, displaces that fluid. Each fluid particle is displaced in the direction of motion of the body. The magnitude of that movement is related to the distance from the path of the body. The fluid therefore gains kinetic energy, which can be calculated using potential flow theory ([8], [9]). The weight added to a system due to the fact that, an accelerating or decelerating body, as it moves, must move some volume of surrounding fluid along with it, is called the added (virtual) mass or inertia. The virtual mass and inertia effects are actually described by the derivatives of aerodynamic force and moment with respect to linear and angular acceleration perturbations. Consider the component of axial force owing to virtual mass effects in a linear axial acceleration perturbation \dot{U} , axial force component = $\frac{\partial X}{\partial \dot{U}} \dot{U} \equiv \overset{o}{X}_u \dot{U}$. Here, $\overset{o}{X}_u$ is the added mass, and the apparent mass in the x -direction is written as below.

$$m_x = m - \overset{o}{X}_u$$

Note that m is the actual mass of the body. Similarly, $\overset{o}{X}_v$ is the added mass along x -axis due to acceleration \dot{v} along y -axis.

Added mass matrix

The three-dimensional nature of the body-fluid interaction implies that the added mass is not a simple scalar, but must account for the accelerations in all six degrees of freedom (DOF) that result from each of the forces and moments. Thus, the general form of an added mass matrix has 36 elements to completely describe the ratio of extra force to acceleration in each combination of DOF, and is given as:

Equation 17: General form of an added mass matrix

$$\begin{bmatrix} X_{\dot{u}} & X_{\dot{v}} & X_{\dot{w}} & X_{\dot{p}} & X_{\dot{q}} & X_{\dot{r}} \\ Y_{\dot{u}} & Y_{\dot{v}} & Y_{\dot{w}} & Y_{\dot{p}} & Y_{\dot{q}} & Y_{\dot{r}} \\ Z_{\dot{u}} & Z_{\dot{v}} & Z_{\dot{w}} & Z_{\dot{p}} & Z_{\dot{q}} & Z_{\dot{r}} \\ L_{\dot{u}} & L_{\dot{v}} & L_{\dot{w}} & L_{\dot{p}} & L_{\dot{q}} & L_{\dot{r}} \\ M_{\dot{u}} & M_{\dot{v}} & M_{\dot{w}} & M_{\dot{p}} & M_{\dot{q}} & M_{\dot{r}} \\ N_{\dot{u}} & N_{\dot{v}} & N_{\dot{w}} & N_{\dot{p}} & N_{\dot{q}} & N_{\dot{r}} \end{bmatrix}$$

Note that, as per the above definition of added mass matrix, it would be added (not subtracted) to the actual mass matrix. This implies that, relative to the definition of added mass terms given in the next Section 2.5, $X_{\dot{u}} = -\overset{o}{X}_{\dot{u}}$, $L_{\dot{p}} = -\overset{o}{L}_{\dot{p}}$, $L_{\dot{r}} = -\overset{o}{L}_{\dot{r}}$, etc.

For any rigid body, actually there are only 21 unique elements in the added mass matrix. This is because it is symmetric about the diagonal, i.e. $X_{\dot{v}} = Y_{\dot{u}}$, $Y_{\dot{q}} = M_{\dot{v}}$, $M_{\dot{r}} = N_{\dot{q}}$, etc. ([10], [11]). In order to simplify the structure of this matrix, the added mass terms are computed with respect

to a body-fixed frame of reference with its origin at the centre of volume (CV) of the airship hull and its x, y, z axes directed along the principal axes of the double ellipsoid. Then, like the case here, if the body or vehicle has port-starboard symmetry about the x - z plane, 9 out of the 21 coefficients will be zero. These include $X_v, X_p, X_r, Y_w, Y_q, Z_p, Z_r, L_q$ and M_r . The value of X_w is also zero, i.e. when the airship experiences a force in the surge (x) direction, there is no direct acceleration in the heave (z) direction. Thus, for the airship configuration chosen here, there are 11 non-zero added mass coefficients and the added mass matrix reduces to:

$$\begin{bmatrix} X_u & 0 & 0 & 0 & X_q & 0 \\ 0 & Y_v & 0 & Y_p & 0 & Y_r \\ 0 & 0 & Z_w & 0 & Z_q & 0 \\ 0 & Y_p & 0 & L_p & 0 & L_r \\ X_q & 0 & Z_q & 0 & M_q & 0 \\ 0 & Y_r & 0 & L_r & 0 & N_r \end{bmatrix}$$

Comparing with **Equation 23** in Section 2.5, it is clear that this matrix is the added-mass component of the apparent mass matrix M_a , i.e.

$$M_{added} = \begin{bmatrix} X_u & 0 & 0 & 0 & X_q & 0 \\ 0 & Y_v & 0 & Y_p & 0 & Y_r \\ 0 & 0 & Z_w & 0 & Z_q & 0 \\ 0 & Y_p & 0 & L_p & 0 & L_r \\ X_q & 0 & Z_q & 0 & M_q & 0 \\ 0 & Y_r & 0 & L_r & 0 & N_r \end{bmatrix} \equiv \begin{bmatrix} {}^oX_u & 0 & 0 & 0 & {}^oX_q & 0 \\ 0 & {}^oY_v & 0 & {}^oY_p & 0 & {}^oY_r \\ 0 & 0 & {}^oZ_w & 0 & {}^oZ_q & 0 \\ 0 & {}^oY_p & 0 & {}^oL_p & 0 & {}^oL_r \\ -{}^oM_u & 0 & -{}^oM_w & 0 & -{}^oM_q & 0 \\ 0 & -{}^oN_v & 0 & -{}^oN_p & 0 & -{}^oN_r \end{bmatrix}$$

Added mass computation

For determining these added mass and inertia terms for a body moving through a fluid, the general method is to find the inertia coefficients, these being the constant coefficients in the expression for kinetic energy of the fluid in terms of the body's component linear and angular velocities relative to body-fixed axes. This method is based on potential flow theory by which air is considered as an inviscid (zero viscosity), incompressible (uniform density) fluid with irrotational flow. The fluid flow around the body can be described with a velocity potential (ϕ) or streamline function. Once the velocity potential of the moving fluid is determined, the kinetic energy of the fluid can be computed using the integral given below [12].

Equation 18: Computation of kinetic energy (T) of the fluid using velocity potential (ϕ)

$$T = -\frac{\rho}{2} \int \phi \frac{d\phi}{dn} dS$$

Here, integration is done over the surface of the body, ϕ being the velocity potential, ρ the density of the fluid and dn an element of the normal to the surface dS drawn into the fluid. This kinetic energy of the fluid surrounding a moving rigid body can also be expressed as a

quadratic function of the six velocity components of the body (3 translations and 3 rotations in body-fixed axes) $\nu = (u, v, w, p, q, r)^T$ as given below ([12], [13]).

$$\begin{aligned} T &= \frac{1}{2} \nu^T M_{added} \nu \\ &\equiv \frac{1}{2} (Au^2 + Bv^2 + Cw^2 + 2A'vw + 2B'wu + 2C'uv + Pp^2 + Qq^2 + Rr^2 \\ &\quad + 2P'qr + 2Q'rp + 2R'pq + 2p(Fu + Gv + Hw) + 2q(F'u + G'v + H'w) \\ &\quad + 2r(F''u + G''v + H''w)) \end{aligned}$$

Here, M_{added} is the added mass matrix (same as in Equation 17 above), and the 21 coefficients $A, B, C, A', B', C', P, Q, R, P', Q', R', F, G, H, F', G', H', F'', G'', H''$ are called the inertia coefficients of the body. Note that these coefficients are exactly the same as the 21 unique entries of the added mass matrix given in **Equation 17**. The coefficients A, B, C, P, Q, R are the diagonal terms, and all other coefficients are the off-diagonal terms (2 each because of the symmetry). These coefficients can be determined by computing the kinetic energy of the fluid using Equation 18.

The inertia coefficients are well known for the case of an ellipsoid with semi-axes a, b, c when the axes of reference are the principal axes of the ellipsoid [7]. As given below, only the diagonal terms are non-zero.

Equation 19: Added mass terms for an ellipsoid

$$\begin{aligned} A = X_{\dot{u}} &= \frac{\alpha_0}{2 - \alpha_0} m, & B = Y_{\dot{v}} &= \frac{\beta_0}{2 - \beta_0} m, & C = Z_{\dot{w}} &= \frac{\gamma_0}{2 - \gamma_0} m, \\ P = L_p &= \frac{(b^2 - c^2)^2(\gamma_0 - \beta_0)}{2(b^2 - c^2) + (b^2 + c^2)(\beta_0 - \gamma_0)} \frac{m}{5}, \\ Q = M_q &= \frac{(c^2 - a^2)^2(\alpha_0 - \gamma_0)}{2(c^2 - a^2) + (c^2 + a^2)(\gamma_0 - \alpha_0)} \frac{m}{5}, \\ R = N_r &= \frac{(a^2 - b^2)^2(\beta_0 - \alpha_0)}{2(a^2 - b^2) + (a^2 + b^2)(\alpha_0 - \beta_0)} \frac{m}{5}, \end{aligned}$$

where $m = \frac{4}{3}\pi\rho abc$ is the mass of fluid displaced by the ellipsoid and

$$\begin{aligned} \alpha_0 &= abc \int_0^\infty \frac{d\lambda}{(a^2 + \lambda)\Delta}, & \beta_0 &= abc \int_0^\infty \frac{d\lambda}{(b^2 + \lambda)\Delta}, & \gamma_0 &= abc \int_0^\infty \frac{d\lambda}{(c^2 + \lambda)\Delta}, \\ \Delta &= \sqrt{(a^2 + \lambda)(b^2 + \lambda)(c^2 + \lambda)} \end{aligned}$$

The general solution is evaluated using elliptic integrals. However for an ellipsoid of revolution ($b = c$), which is relevant for airships, computation of the inertia coefficients is simplified as follows (e.g. a prolate spheroid, $a > b = c$):

Equation 20: Modifications in the added mass terms for a prolate spheroid ($a > b = c$)

$$B = C, \quad P = 0, \quad Q = R = \frac{a^2 e^4 (\beta_0 - \alpha_0)}{2e^2 + (2 - e^2)(\alpha_0 - \beta_0)} \frac{m}{5},$$

$$\alpha_0 = \frac{(1 - e^2)}{e^3} \left[\log \frac{1 + e}{1 - e} - 2e \right], \quad \beta_0 = \gamma_0 = \frac{1}{e^2} - \frac{(1 - e^2)}{2e^3} \log \frac{1 + e}{1 - e}$$

Here, $e = \sqrt{1 - \left(\frac{b}{a}\right)^2}$ is the eccentricity of the longitudinal section of the prolate spheroid.

Thus, for a body shaped as a prolate ellipsoid, the added mass matrix will be strictly diagonal, and Equation 19 and Equation 20 can be used to calculate the added mass terms. But the added mass matrix of an airship, even if its hull is shaped as a prolate ellipsoid, is not strictly diagonal due to the presence of fins and gondola; however, the non-diagonal terms of the added mass matrix are much smaller than its diagonal terms, and hence they could be safely ignored. Now for a generic-shaped airship hull, computation of the added-mass terms is quite difficult. The common method is to fit the hull shape with an ellipsoid of revolution with the same meridian cross-sectional area S_h and length L_h as the hull ([14], [15]). The thickness ratio of this ellipsoid will be $b/a = 4S_h/\pi L_h^2$. The inertia coefficients of this ellipsoid in the axial ($A = X_{\dot{u}}$), lateral ($B = Y_{\dot{v}} = C = Z_{\dot{w}}$), and rotational motion about a transverse axis ($Q = M_{\dot{q}} = R = N_{\dot{r}}$) can be calculated using Equation 19 and Equation 20.

In the current work, an axis-symmetric double-ellipsoidal airship hull has been chosen (Section 2.3, Figure 2). The inertia coefficients for this airship have been calculated using Equation 19 and Equation 20 by defining a as the mean value of a_1 and a_2 of the double-ellipsoidal hull model. The inertia factors (k_1, k_2, k_3) of Section 2.3 (Equation 9 and Equation 10) are related to the inertia coefficients of Equation 19 and Equation 20 as follows:

$$A = X_{\dot{u}} = k_1 * m_{de}, \quad B = Y_{\dot{v}} = C = Z_{\dot{w}} = k_2 * m_{de}, \quad Q = M_{\dot{q}} = R = N_{\dot{r}} = k_3 * m_{de},$$

where $m_{de} = \frac{2}{3}\pi\rho(a_1 + a_2)b^2$ is the mass of fluid displaced by the double ellipsoid. Thus, with reference to Equation 23 of next Section 2.5, the off-diagonal added-mass terms are all zero, and the diagonal terms are given as follows:

$$\begin{aligned} {}^o X_{\dot{u}} &= -A = -\frac{\alpha_0}{2 - \alpha_0} m_{de}, & {}^o Y_{\dot{v}} &= -B = -\frac{\beta_0}{2 - \beta_0} m_{de} = {}^o Z_{\dot{w}}, \\ {}^o L_{\dot{p}} &= 0, & {}^o M_{\dot{q}} &= -Q = -\frac{a^2 e^4 (\beta_0 - \alpha_0)}{2e^2 + (2 - e^2)(\alpha_0 - \beta_0)} \frac{m_{de}}{5} = {}^o N_{\dot{r}}. \end{aligned}$$

Here, $a = \frac{a_1 + a_2}{2}$ and the parameters α_0, β_0 are calculated from Equation 20.

2.5. Equations of motion

Let U , V and W denote the components of the airship's velocity (V_0) along the x , y and z axes, respectively. Also, let p , q and r denote the angular velocities about the x , y and z axes, respectively. Thus the airship's dynamic state can be defined as $\mathbf{x} = [U \ V \ W \ p \ q \ r]^T$. The airship has reached this state due to a perturbation from an equilibrium condition corresponding to the state $\mathbf{x}_0 = [U_e \ V_e \ W_e \ 0 \ 0 \ 0]$. If u , v and w are the corresponding perturbations in the three velocity components, we can write the following:

$$U = U_e + u, \quad V = V_e + v \quad \text{and} \quad W = W_e + w.$$

Now, the apparent mass of the airship along the three translational degrees of freedom (x , y and z) are defined as given below. Note that m is the actual mass of the airship, and X , Y and Z denote the forces along the x , y and z axes, respectively. Also, the aerodynamic derivatives used here and in the previous section are defined as follows: e.g. $\overset{o}{X}_{\dot{u}} = \frac{\partial X}{\partial \dot{u}}$.

$$\text{Axial direction, } m_x = m - \overset{o}{X}_{\dot{u}}$$

$$\text{Lateral direction, } m_y = m - \overset{o}{Y}_{\dot{v}}$$

$$\text{Normal direction, } m_z = m - \overset{o}{Z}_{\dot{w}}$$

The apparent moments of inertia for the three rotational degrees of freedom (roll (x), pitch (y) and yaw (z)) are defined as given below. Here, L , M and N denote the moments about the x , y and z axes, respectively.

$$\text{Rolling motion about the } x\text{-axis, } J_x = I_x - \overset{o}{L}_{\dot{p}}$$

$$\text{Pitching motion about the } y\text{-axis, } J_y = I_y - \overset{o}{M}_{\dot{q}}$$

$$\text{Yawing motion about the } z\text{-axis, } J_z = I_z - \overset{o}{N}_{\dot{r}}$$

Also, the apparent products of inertia are defined as given below. But, since the airship is symmetric about the x - z plane, $J_{xy} = 0$ and $J_{yz} = 0$.

$$J_{xy} = I_{xy} + \overset{o}{L}_{\dot{q}} \equiv I_{xy} + \overset{o}{M}_{\dot{p}}$$

$$J_{yz} = I_{yz} + \overset{o}{M}_{\dot{r}} \equiv I_{yz} + \overset{o}{N}_{\dot{q}}$$

$$J_{zx} = I_{zx} + \overset{o}{N}_{\dot{p}} \equiv I_{zx} + \overset{o}{L}_{\dot{r}}$$

Airship flight dynamics is governed by a set of differential equations as given below. This set of six nonlinear first-order ordinary differential equations can be written in matrix form

([4], [5], [16]) as given in Equation 21. The variables used in this equation are defined in Table 3.

Equation 21: Governing equations for the dynamics of airship flight

$$M_a \dot{\mathbf{x}} = F_d + F_a + F_b + F_g + F_c + F_p + F_f$$

Table 3: Definition of different variables used in Equation 21

Variable	Definition
\mathbf{x}	Dynamic system state vector (6x1 vector)
M_a	Mass and Inertia matrix (6x6 matrix)
F_d	Coriolis and centrifugal terms of the dynamic model (6x1 vector)
F_a	Aerodynamic forces and moments due to hull and fins (6x1 vector)
F_b	Buoyancy forces and moments (6x1 vector)
F_g	Gravitational forces and moments (6x1 vector)
F_c	Aerodynamic forces and moments due to control surfaces (6x1 vector)
F_p	Propulsive forces and moments (6x1 vector)
F_f	Forces and moments due to the fluids' inertial motion (6x1 vector)

As defined above, $\mathbf{x} = [U \ V \ W \ p \ q \ r]^T$. The force vector of Coriolis and centrifugal terms is defined as follows: $F_d = [f_1 \ f_2 \ f_3 \ f_4 \ f_5 \ f_6]^T$ where the individual f_i 's are defined as given below.

Equation 22: Components of the force vector, F_d

$$f_1 = -m_z q W + m_y r V + m a_x (q^2 + r^2) - m a_z r p$$

$$f_2 = -m_x r U + m_z p W - m a_x p q - m a_z q r$$

$$f_3 = -m_y p V + m_x q U - m a_x r p + m a_z (p^2 + q^2)$$

$$f_4 = (J_y - J_z) q r + J_{xz} p q + m a_z (r U - p W)$$

$$f_5 = (J_z - J_x) r p + J_{xz} (r^2 - p^2) + m a_x (p V - q U) - m a_z (q W - r V)$$

$$f_6 = (J_x - J_y) p q - J_{xz} q r - m a_x (r U - p W)$$

The mass and inertia matrix M_a is a 6×6 matrix with entries as given below. Here, a_x and a_z are the coordinates of the center of gravity (CG) relative to the center of volume (CV). Note that since the airship being studied is symmetric about the XZ plane, the lateral coordinate $a_y = 0$.

Equation 23: Mass and Inertia matrix

$$M_a = \begin{bmatrix} m_x & 0 & 0 & 0 & ma_z - \dot{X}_{\dot{q}}^o & 0 \\ 0 & m_y & 0 & -ma_z - \dot{Y}_{\dot{p}}^o & 0 & ma_x - \dot{Y}_{\dot{r}}^o \\ 0 & 0 & m_z & 0 & -ma_x - \dot{Z}_{\dot{q}}^o & 0 \\ 0 & -ma_z - \dot{L}_{\dot{v}}^o & 0 & J_x & 0 & -J_{xz} \\ ma_z - M_{\dot{u}}^o & 0 & -ma_x - M_{\dot{w}}^o & 0 & J_y & 0 \\ 0 & ma_x - N_{\dot{v}}^o & 0 & -J_{xz} & 0 & J_z \end{bmatrix}$$

Now, rest of the force vectors in Equation 21 can be written in the form given below. Here, j stands for a, b, g, c, p or f (Table 3). For each j , X_j, Y_j and Z_j are the components of the corresponding force along the three axes, and L_j, M_j and N_j are the components of the corresponding moment about the three axes.

$$F_j = [X_j \ Y_j \ Z_j \ L_j \ M_j \ N_j]^T$$

First we shall discuss and define the static forces, i.e., buoyancy and gravitational forces. They are almost constant (slowly varying), and not a function of the dynamics of the airship. Essentially, the components of the force/moment vectors F_b and F_g are functions of the airship's rotational angles (Euler angles) with respect to an inertial (earth) frame of reference. Here, we consider these two force/moment vectors together. Let θ_e be the equilibrium pitch angle of the airship, and let B denote the net buoyancy force acting on it. Also, b_x and b_z are used as the coordinates of center of buoyancy (CB) relative to CV. Note that since the airship being studied is symmetric about the XZ plane, the lateral coordinate $b_y = 0$. The equations used for determining the buoyancy and gravitational forces and moments are given below.

Equation 24: 3-axis components of buoyancy and gravitational forces and moments [4]

$$X_b + X_g = -(mg - B) \sin(\theta + \theta_e)$$

$$Y_b + Y_g = (mg - B) \sin \phi \cos(\theta + \theta_e)$$

$$Z_b + Z_g = (mg - B) \cos \phi \cos(\theta + \theta_e)$$

$$L_b + L_g = -(mga_z - Bb_z) \sin \phi \cos(\theta + \theta_e)$$

$$M_b + M_g = -(mga_z - Bb_z) \sin(\theta + \theta_e) - (mga_x - Bb_x) \cos \phi \cos(\theta + \theta_e)$$

$$N_b + N_g = (mga_x - Bb_x) \sin \phi \cos(\theta + \theta_e)$$

Note that Equation 21, Equation 22 and Equation 23 have been reproduced from the work done by Gomes and Ramos [5], whereas Equation 24 has been obtained from the book by Khouri and Gillett [4]. Also, as in [4], here the aerodynamic forces and moments are divided into two groups, one due to the hull and fins (F_a) and the other due to control actuation (F_c).

Note that in the specific aerodynamic model that was described in Section 2.3, these two contributions are considered together. The aerodynamic coefficients defined in Equation 2 to Equation 7 contain all the terms due to hull, fins and control surfaces (Table 1). Thus, here the mathematical expressions for F_a & F_c from [4] will not be discussed. Instead, these quantities can be directly calculated from the equations (Equation 2 to Equation 7) given in Section 2.3, i.e. $F_a + F_c = [X \ Y \ Z \ L \ M \ N]^T$.

Forces and moments on the airship are also produced by the propulsion units that are used to propel the airship forward or in a required direction. These are captured in the vector F_p . This particular airship has four engines (propulsors), two of them some distance ahead of the CG and the other two the same distance behind the CG. In each pair (front or rear), one propulsor is fixed on the port side (sp , left) of the gondola and the other on the starboard side (ss , right). The force equations are as given in Equation 25, and the moment equations are shown in Equation 26. (The subscripts f and r denote front and rear, respectively.)

Equation 25: Forces due to the propulsive units

$$X_p = T_{ssf} \cos \mu_{ssf} + T_{spf} \cos \mu_{spf} + T_{ssr} \cos \mu_{ssr} + T_{spr} \cos \mu_{spr}$$

$$Y_p = 0$$

$$Z_p = -T_{ssf} \sin \mu_{ssf} - T_{spf} \sin \mu_{spf} - T_{ssr} \sin \mu_{ssr} - T_{spr} \sin \mu_{spr}$$

Equation 26: Moments due to the propulsive units

$$L_p = (T_{spf} \sin \mu_{spf} - T_{ssf} \sin \mu_{ssf}) d_{fy} + (T_{spr} \sin \mu_{spr} - T_{ssr} \sin \mu_{ssr}) d_{ry}$$

$$M_p = T_{spf} (d_{fz} \cos \mu_{spf} + d_{fx} \sin \mu_{spf}) + T_{ssf} (d_{fz} \cos \mu_{ssf} + d_{fx} \sin \mu_{ssf}) \\ + T_{spr} (d_{rz} \cos \mu_{spr} - d_{rx} \sin \mu_{spr}) + T_{ssr} (d_{rz} \cos \mu_{ssr} - d_{rx} \sin \mu_{ssr})$$

$$N_p = (T_{spf} \cos \mu_{spf} - T_{ssf} \cos \mu_{ssf}) d_{fy} + (T_{spr} \cos \mu_{spr} - T_{ssr} \cos \mu_{ssr}) d_{ry}$$

Here d_{fx} , d_{rx} , d_{fy} , d_{ry} , d_{fz} and d_{rz} are the coordinates of the points of action of the thrust (both on the port and starboard sides; these six quantities are defined as positive distances from the center of volume). T_{ssf} , T_{ssr} , T_{spf} and T_{spr} are the thrust magnitudes and μ_{ssf} , μ_{ssr} , μ_{spf} and μ_{spr} are the corresponding pitch-vectoring angles defining the direction of each thrust in its pitch plane.

The last forces and moments vector F_f is defined as given below in Equation 27. These expressions have been derived based on the work done in [17], [18] and [19].

Equation 27: Forces and Moments due to fluids' inertial motion

$$X_f = \bar{m}_z q W_f - \bar{m}_y r V_f$$

$$Y_f = \bar{m}_x r U_f - \bar{m}_z p W_f$$

$$Z_f = \bar{m}_y p V_f - \bar{m}_x q U_f$$

$$L_f = -(\bar{J}_y q_f r - \bar{J}_z qr_f) - \bar{J}_{xz} p_f q$$

$$M_f = -(\bar{J}_z r_f p - \bar{J}_x rp_f) - \bar{J}_{xz}(rr_f - pp_f)$$

$$N_f = -(\bar{J}_x p_f q - \bar{J}_y pq_f) + \bar{J}_{xz} qr_f$$

These expressions are sufficient only for the typical case when the center of buoyancy (CB) is coincident with the center of volume (CV) of the airship, i.e. $b_x = 0$ and $b_z = 0$. Here the variables U_f , V_f , W_f and p_f , q_f , r_f are the inertial linear and angular velocities of the surrounding fluid, expressed in body-fixed axes. Further, the apparent masses, inertias and products of inertia of the displaced fluid are defined as follows:

$$\text{Axial direction, } \bar{m}_x = \bar{m} - \overset{o}{X}_{\dot{u}}$$

$$\text{Lateral direction, } \bar{m}_y = \bar{m} - \overset{o}{Y}_{\dot{v}}$$

$$\text{Normal direction, } \bar{m}_z = \bar{m} - \overset{o}{Z}_{\dot{w}}$$

$$\text{Rolling motion about the } x\text{-axis, } \bar{J}_x = \bar{I}_x - \overset{o}{L}_{\dot{p}}$$

$$\text{Pitching motion about the } y\text{-axis, } \bar{J}_y = \bar{I}_y - \overset{o}{M}_{\dot{q}}$$

$$\text{Yawing motion about the } z\text{-axis, } \bar{J}_z = \bar{I}_z - \overset{o}{N}_{\dot{r}}$$

$$\text{And, } \bar{J}_{zx} = \bar{I}_{zx} + \overset{o}{N}_{\dot{p}} \equiv \bar{I}_{zx} + \overset{o}{L}_{\dot{r}}$$

Note that $\bar{m} = \rho_a * \frac{2}{3}\pi b^2(a_1 + a_2)$ is the actual mass of the displaced fluid, and \bar{I}_x , \bar{I}_y , \bar{I}_z and \bar{I}_{zx} are its moment of inertia parameters about different axes.

2.6. Equations of Motion in the Earth-Centered Inertial (ECI) frame

Effect of Earth's rotation and ellipsoidal shape of Earth

To accurately simulate navigation of a high altitude airship as part of the present system simulation, the effect of the Earth's rotation about its own axis and the changes due to the ellipsoidal shape of the Earth will have to be considered as part of the airship dynamics. For this, equations of motion have to be derived in an Earth-Centered Inertial (ECI) frame (inertial or i frame). These equations for velocity dynamics and angular velocity dynamics are different from those given in Equation 21. With the help of a few references ([33], [45] and [46]), here we shall describe the essential details of this model, i.e. parameters, variables and final differential equations. The different variables involved in this model and the acronyms that are used in this section are defined in Table 4. Also, Table 5 lists the definitions and values of various constant parameters.

Table 4: Definitions of system variables and acronyms used

Variable / Acronym	Definition
ECI / inertial / i frame	Earth-Centered Inertial reference frame
i_x, i_y, i_z	Axis notation for inertial frame
ECEF / earth / e frame	Earth-Centered Earth-Fixed reference frame
e_x, e_y, e_z	Axis notation for earth frame
NED / n frame	North-East-Down local level reference frame
n_x, n_y, n_z	Axis notation for NED frame
b frame	Body-fixed reference frame
b_x, b_y, b_z	Axis notation for body-fixed frame
\bar{G}	Gravitation vector in ECI frame
\bar{g}	Gravity vector on a rotating Earth in local NED frame
R_m	Radius of curvature along line of constant longitude
R_n	Radius of curvature along line of constant latitude
J_1, J_2	Earth's gravitational constants, first and second
L	Longitude on Earth (0 deg to 360 deg)
GM	Greenwich Meridian ($L = 0$)
μ, μ_c	Geodetic latitude, Geocentric latitude [-90 deg (South Pole) to +90 deg (North Pole)]
λ	Angle between earth frame and inertial frame at any particular time instant (0 deg to 360 deg)
ϕ, θ, ψ	Euler angles defining the body orientation with respect to the local NED frame
q_0, q_1, q_2, q_3	Quaternion angles defining the body orientation with respect to the local NED frame
$\bar{()}$	bar, denotes a vector variable
(\cdot) ^{superscript}	superscript, denotes the coordinate frame in which the vector is expressed
C_i^j	Direction Cosine Matrix (DCM), the rotation matrix which transforms a vector from frame i to frame j
$\bar{\omega}_{ij}^k = [\omega_{ij,x}^k \omega_{ij,y}^k \omega_{ij,z}^k]^T$	Angular velocity of frame j relative to frame i , expressed in the k coordinate frame, typically $k = i$ or j
Ω_{ij}^k	The skew-symmetric matrix corresponding to $\bar{\omega}_{ij}^k$

Table 5: Definitions and numerical values of system parameters

Parameter	Definition	Value
ω_e	Angular velocity of Earth's rotation about its own axis. Note that $\lambda = \omega_e$.	7.29×10^{-5} radians/sec
R_e	Radius of the Earth at the equator	6378137 m
R_p	Radius of the Earth at the poles	6356752 m
ϵ	Eccentricity of ellipsoidal Earth	0.0818
J_1	Earth's gravitational constant	$3.986005 \times 10^{+14}$ m ³ /sec ²
J_2	Second gravitational constant	1.08263×10^{-3}
g_{WGS_0}	Gravity at equator	9.78033 m/sec ²
g_{WGS_1}	Gravity formula constant	0.00193185

As mentioned earlier, Newton's equations of motion have to be derived with respect to the Earth-Centered Inertial (ECI) frame. This is a reference frame which does not rotate with the Earth but its origin stays fixed at the Earth's center as the Earth revolves around the sun. Its x and y axis lie in the equatorial plane and the z axis passes through the North Pole (Figure 3). The Earth is rotating with respect to this reference frame with its angular velocity (ω_e , Table 5) directed along the positive z axis (i_z or e_z). A second reference frame is defined, called Earth-Centered Earth-Fixed (ECEF) frame, which remains fixed to the Earth as it rotates, its z axis passes through the North Pole, x axis is taken to be directed along the Greenwich Meridian (GM), and y axis is such that the three axes form an orthogonal set. Thus, at any time instant t , ECEF frame makes an angle $\lambda = \omega_e t$ with the ECI frame. So at $t = 0$, i_x and e_x coincide with each other. Thus, if we are running a system simulation of the airship at a particular place on Earth's surface for a 24 hour period, $t = 0$ can be defined to be the instant when the actual time at that place hits 8:00 AM. Since this is the starting point of the simulation, i_x and e_x will be directed along the GM. Once the simulation starts, the e frame will rotate with the Earth while the i frame will remain fixed in inertial space with orientations corresponding to the starting point.

The local NED frame is defined at the place where we want to simulate the system. The b frame is a body-fixed frame with its origin at the center of gravity (CG). Its axes are directed along the airship's longitudinal (forward), lateral (right) and directional (down) axes (similar to a typical aircraft). The origin of the NED frame would be fixed at a point on the Earth's surface directly below the airship CG. The NED frame is obtained starting from earth frame by first rotating around the e_z axis through the longitude, L and subsequently rotating about the new $-e'_y$ axis through the latitude angle μ and an additional $\pi/2$.

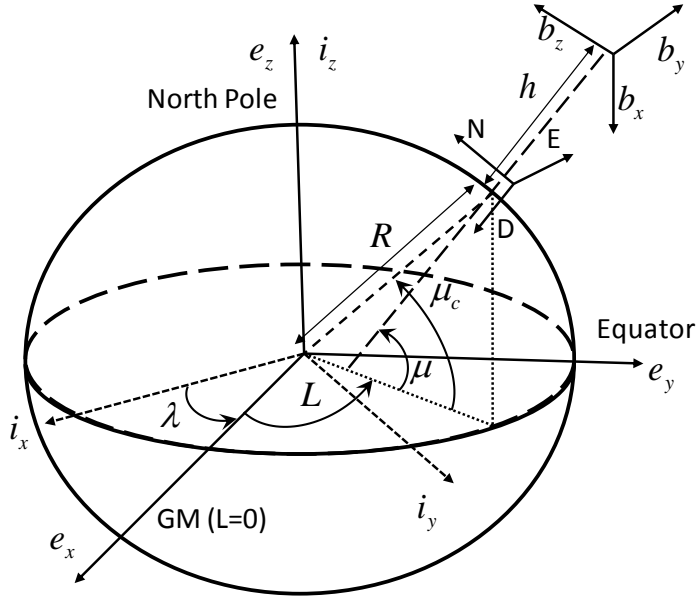


Figure 3: The inertial frame is spanned by i_x, i_y and i_z . The earth frame is the inertial frame rotated around the i_z axis through the angle λ . The NED frame is the earth frame rotated around the e_z axis through the longitudinal angle L , and thereafter rotated negatively around the new e'_y axis through the latitude angle μ and another $\pi/2$.

For studying airship dynamics by considering Earth's rotation, the variables of interest are the following:

- Absolute angular velocity with respect to the ECI frame
- Relative linear velocity with respect to the ECEF frame (equivalently, in the NED frame), \bar{V}
- Relative angular velocity with respect to the local NED frame

Also, the dynamical equations have been derived based on the following assumptions:

- Mass of the airship is constant, i.e. $\dot{m} = 0$
- Origin of the body frame is fixed at the CG
- Earth's rotation rate ω_e is assumed to be constant
- Effect of other celestial bodies (Sun, other stars and planets) on the current Earth-Airship system is ignored.
- The airship is considered to be a rigid body

The translational dynamics of the body with respect to the ECEF frame is described by the differential equation given below. Here notations similar to those defined in Section 2.5 have been used. Note that the applied forces $[X \ Y \ Z]^T$ are in the body frame, as was the case in Equation 21.

Equation 28: Translational dynamics

$$\bar{F}^b = \begin{bmatrix} X \\ Y \\ Z \end{bmatrix}^b = m \left[\dot{\bar{V}}^b + \bar{\omega}_{ib}^b \times \bar{V}^b + \bar{\omega}_{ie}^b \times \bar{V}^b + C_e^b (\bar{\omega}_{ie}^e \times (\bar{\omega}_{ie}^e \times \bar{r}^e)) \right]$$

Here the rate of change of body position in the ECEF frame, $\dot{\bar{r}}^e$ is calculated using the equation, $\dot{\bar{r}}^e = C_b^e \bar{V}^b$. Also, the definitions and formulae of different variables used in the above equation are as follows: velocity of the body with respect to ECEF frame, expressed in body frame, $\bar{V}^b = [u \ v \ w]^T$, relative angular rates of the body with respect to NED frame, expressed in body frame, $\bar{\omega}_{nb}^b = [p \ q \ r]^T$, Earth's rotation rate, $\bar{\omega}_{ie}^i = \bar{\omega}_{ie}^e = [0 \ 0 \ \omega_e]^T$, angular rates of the body with respect to ECI frame, expressed in body frame, $\bar{\omega}_{ib}^b = \bar{\omega}_{nb}^b + C_i^b \bar{\omega}_{ie}^i + C_n^b \bar{\omega}_{en}^n$, and angular rates of NED frame with respect to earth (ECEF) frame, expressed in NED or n frame,

$$\bar{\omega}_{en}^n = \begin{bmatrix} \dot{L} \cos \mu \\ -\dot{\mu} \\ -\dot{L} \sin \mu \end{bmatrix} = \begin{bmatrix} V_E / (R_n + h) \\ -V_N / (R_m + h) \\ -V_E \tan \mu / (R_n + h) \end{bmatrix}$$

The rotational dynamics of the body expressed in the body-fixed frame are given below, where the applied moments are L , M and N , and the inertia tensor I is determined with respect to the origin of b frame.

Equation 29: Rotational dynamics

$$\bar{T}^b = \begin{bmatrix} L \\ M \\ N \end{bmatrix}^b = I \dot{\bar{\omega}} + \bar{\omega} \times (I \bar{\omega}), \quad \text{where } \bar{\omega} = \bar{\omega}_{ib}^b$$

For the present case of airship dynamics, Equation 28 and Equation 29 will get modified as follows. In the translational dynamics, mass m will get substituted by the 3×3 diagonal matrix $\begin{bmatrix} m_x & 0 & 0 \\ 0 & m_y & 0 \\ 0 & 0 & m_z \end{bmatrix}$ (refer Equation 23). Also, in the rotational dynamics, inertia I will get

substituted by the 3×3 matrix $\begin{bmatrix} J_x & 0 & -J_{xz} \\ 0 & J_y & 0 \\ -J_{xz} & 0 & J_z \end{bmatrix}$. Referring to Equation 23, note that all other off-diagonal terms are zero, because the off-diagonal added-mass-and-inertia terms are anyway zero (Section 2.4) and also, the equations of motion described above are valid only for the case when the body-frame origin is at the airship CG ($a_x = 0 = a_z$).

For non-zero a_x and a_z , Equation 28 and Equation 29 will get further modified based on Equation 22 and Equation 23. Essentially, the vector $[\bar{F}^b \ \bar{T}^b]^T$ from Equation 28 and Equation 29 directly corresponds to the sum $F_a + F_b + F_g + F_c + F_p$ of Equation 21. The F_d and F_f terms have been taken to the other side, and thus $M_a \dot{x} - F_d - F_f$ of Equation 21 substitutes the terms on the right hand side of Equation 28 and Equation 29. The final set of differential equations that have been implemented in our Simulink model, to describe translational and rotational dynamics of the airship, can be written as given below.

Equation 30: Equations of motion

$$\begin{bmatrix} \bar{F}^b \\ \bar{T}^b \end{bmatrix} = F_a + F_c + F_b + F_g + F_p = M_a \dot{x} - F_d - F_f$$

Here the aerodynamic forces and moments vector $F_a + F_c$ is defined in Equation 2 to Equation 7, $F_b + F_g$ is given in Equation 24, F_p is defined in Equation 25 and Equation 26, M_a is given in Equation 23, F_d is defined in Equation 22, and F_f is defined in Equation 27. Note that, in these equations, the integrated state describing the rotational dynamics is $\bar{\omega}_{ib}^b$, angular velocity with respect to the ECI frame, same as in Equation 29. But the integrated state describing the translational dynamics is $\bar{V}_{eci}^b = [u_i \ v_i \ w_i]^T$, linear velocity with respect to the ECI frame, different from that in Equation 28. The NED velocity is calculated using the following equation:

$$\bar{V}^b = \bar{V}_{eci}^b - C_e^b (\bar{\omega}_{ie}^e \times \bar{r}^e)$$

Thus the state vector $\mathbf{x} = [u_i \ v_i \ w_i \ p_i \ q_i \ r_i]^T$, and the same ECI linear and angular velocities go as input into the equations for F_d and F_f .

Finally, the differential equations governing the rotational kinematics remain unchanged as given below. The body orientation can be determined in terms of the quaternion angles by integrating these equations ($\bar{\omega} = \bar{\omega}_{nb}^b$).

$$\begin{bmatrix} \dot{q}_0 \\ \dot{q}_1 \\ \dot{q}_2 \\ \dot{q}_3 \end{bmatrix} = -\frac{1}{2} \begin{bmatrix} 0 & \bar{\omega}_x & \bar{\omega}_y & \bar{\omega}_z \\ -\bar{\omega}_x & 0 & -\bar{\omega}_z & \bar{\omega}_y \\ -\bar{\omega}_y & \bar{\omega}_z & 0 & -\bar{\omega}_x \\ -\bar{\omega}_z & -\bar{\omega}_y & \bar{\omega}_x & 0 \end{bmatrix} \begin{bmatrix} q_0 \\ q_1 \\ q_2 \\ q_3 \end{bmatrix}$$

Now we will look at some additional equations and formulae which accompany the equations of motion described above. The mathematical expressions for the various DCMs are as given below (coordinate transformations).

$$C_n^b = \begin{bmatrix} 1 & 0 & 0 \\ 0 & \cos \phi & \sin \phi \\ 0 & -\sin \phi & \cos \phi \end{bmatrix} \begin{bmatrix} \cos \theta & 0 & -\sin \theta \\ 0 & 1 & 0 \\ \sin \theta & 0 & \cos \theta \end{bmatrix} \begin{bmatrix} \cos \psi & \sin \psi & 0 \\ -\sin \psi & \cos \psi & 0 \\ 0 & 0 & 1 \end{bmatrix}$$

$$C_e^b = C_n^b \begin{bmatrix} \cos\left(\mu + \frac{\pi}{2}\right) & 0 & \sin\left(\mu + \frac{\pi}{2}\right) \\ 0 & 1 & 0 \\ -\sin\left(\mu + \frac{\pi}{2}\right) & 0 & \cos\left(\mu + \frac{\pi}{2}\right) \end{bmatrix} \begin{bmatrix} \cos L & \sin L & 0 \\ -\sin L & \cos L & 0 \\ 0 & 0 & 1 \end{bmatrix}$$

$$C_i^b = C_e^b \begin{bmatrix} \cos \lambda & \sin \lambda & 0 \\ -\sin \lambda & \cos \lambda & 0 \\ 0 & 0 & 1 \end{bmatrix}$$

The equations for determining radii of curvature (Earth model) are

$$R_m = \frac{R_e(1 - \epsilon^2)}{(1 - \epsilon^2 \sin^2 \mu)^{\frac{3}{2}}}$$

$$R_n = \frac{R_e}{(1 - \epsilon^2 \sin^2 \mu)^{\frac{1}{2}}}$$

Geodetic and geocentric latitudes are related through the following expression:

$$\tan \mu_c = (1 - \epsilon^2) \tan \mu$$

The equations for x - y - z coordinates in the ECEF frame are as follows (navigation equations):

$$x^e = (R + h) \cos \mu \cos L$$

$$y^e = (R + h) \cos \mu \sin L$$

$$z^e = (R(1 - \epsilon^2) + h) \sin \mu$$

$$R = \frac{R_e}{(1 - \epsilon^2 \sin^2 \mu)^{\frac{1}{2}}}$$

Here, R is the radial distance from the center of the Earth to the particular point on Earth's surface. Also, a nominal gravity model is used in this system simulation by which the magnitude of gravity on Earth's surface can be expressed in the following form [46]:

$$g = g_{WGS_0} \frac{(1 + g_{WGS_1} \sin^2 \mu)}{(1 - \epsilon^2 \sin^2 \mu)^{\frac{1}{2}}}$$

Here g_{WGS_0} is the gravity at equator, and g_{WGS_1} is the gravity formula constant. The values of these parameters are given in Table 5. For navigation, dynamic evolution of velocity, position and attitude is required in a local navigation frame similar to the NED / n frame used here.

2.7. External environment: Solar Radiation

In this section and the next, the mathematical models, which will be used to determine various environment-related parameters for the airship system simulation, are described. The two significant environmental factors, that drive the design and capabilities of a high altitude airship, are winds and solar radiation. The former will be discussed in the next section. First we look at modeling the solar radiation environment which is the main factor that dictates the amount of electric power produced by photovoltaic cells.

The incident solar radiation, in fact, is very predictable and can be modeled with significant accuracy. The solar radiation that is received by a particular solar array, which is installed on the airship, is a constantly changing quantity. Essentially, it depends on the following parameters:

1. Solar elevation angle, which in turn is dependent on the time of year and the airship's operational latitude

2. Solar intensity, which also changes throughout the year due to slight variations in the distance of the Earth from the Sun
3. Specific location of a given photovoltaic cell on the airship and the shape of the airship
4. Time of day, time of year, latitude, and airship orientation
5. Environmental factors

The solar intensity (SI) or solar flux at Earth's orbital location is, on average, $SI_m = 1352 \text{ W/m}^2$. The actual flux will vary throughout the year as the Earth orbits the Sun. This variation is caused by the orbit not being exactly circular. The variation in Earth's orbital radius (r_{orb}) from the mean orbital radius ($r_{orb,m}$) is represented by the eccentricity (ϵ) of Earth's orbit which has a value of 0.017. The mean orbital radius of Earth is $r_{orb,m} = 1.496 \times 10^8 \text{ km}$. The actual orbital radius is given by the following equation:

Equation 31: Earth's orbital radius, r_{orb}

$$r_{orb} = \frac{r_{orb,m}(1 - \epsilon^2)}{1 + \epsilon \cos \gamma}$$

Here the day angle (γ) is defined as 0° on January 4th (perihelion of Earth's orbit) and increases by 0.98° per day. Finally, the actual solar flux in W/m^2 for a particular day of the year is determined using Equation 31 and Equation 32.

Equation 32: Solar intensity, SI

$$SI = SI_m \left(\frac{r_{orb,m}^2}{r_{orb}^2} \right)$$

To determine the amount of power produced by the solar array, the incident flux on the array has to be found out. The other parameters, which affect the solar array output, are listed above and further explained using Figure 4. Flight latitude is denoted by ϕ , time of year decides the declination angle δ , time of day decides the solar elevation angle θ , environmental factors are modeled as atmospheric attenuation τ , and finally, the solar cell has a conversion efficiency η .

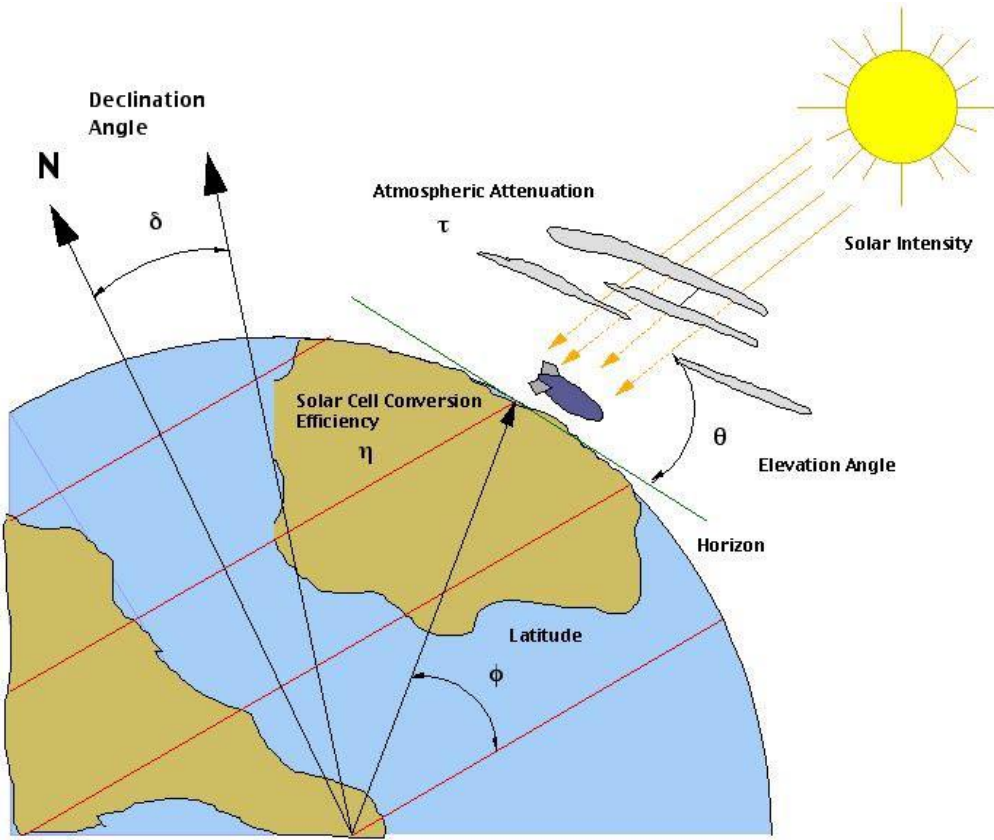


Figure 4: Factors that affect the airship's power production capabilities

Also, the solar array produces power by using only the normal component of the solar flux incident on its surface. Due to the particular shape of the airship, the intra-day variation in the solar elevation angle, and the changes in the position and orientation of the airship, this incident angle will be different along the array (from the side of the airship to the top) and will vary throughout the day. Determining this incident angle is a critical factor in modeling the output power produced by the solar arrays.

The particular model described here has been obtained from the work done by [20]. This model has been developed based on the following assumptions:

1. It is assumed that the airship is a cylinder capped with a hemispherical surface on the front and rear (Figure 5). The solar array is assumed to be only on the upper-half surface of the cylindrical portion.
2. The airship is assumed to be oriented horizontal (parallel to the local surface) with no pitching of the nose upward or downward.
3. Further, it is assumed that a strip of solar cells on the cylindrical portion parallel to the central axis of the airship from the nose to the tail will all make the same angle with the sun at any given moment. The only variation in the incident angle will occur as we move on the surface from one strip to another along a particular cross-section of the cylinder starting from the top to the sides.

Thus to calculate the total power from the solar arrays, the power output or the normal component of the solar flux has to be calculated incrementally and then summed over the surface of the airship. The geometry of an incremental section of the solar array is shown in Figure 5.

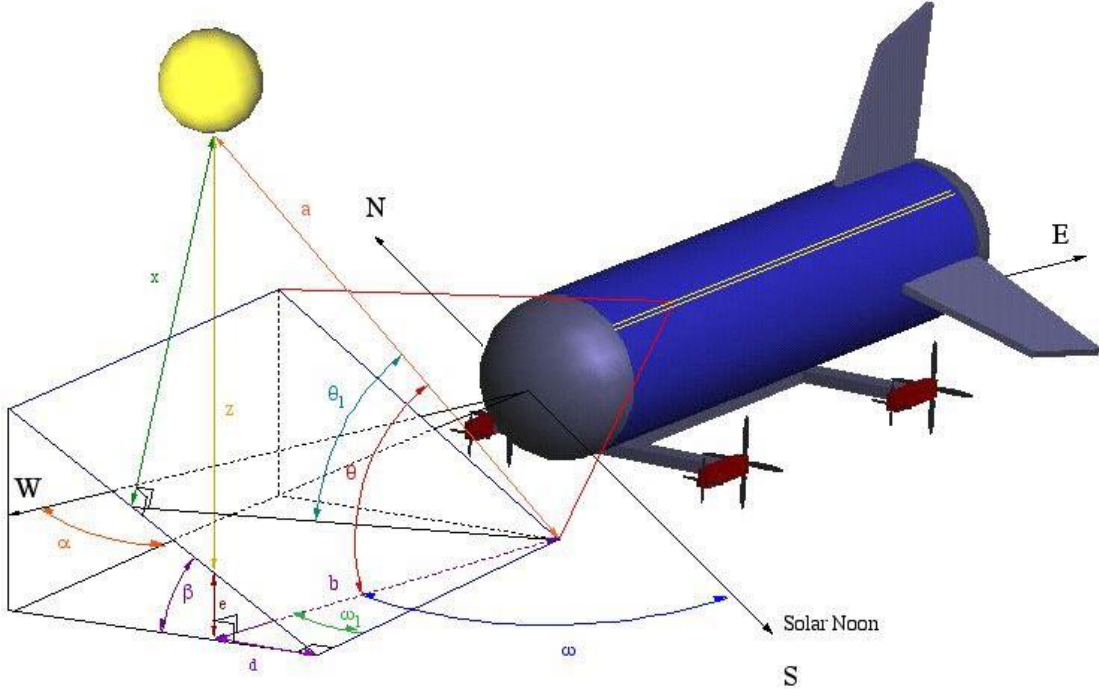


Figure 5: Incident flux geometry for the solar arrays [20]

The incident solar flux or power (P_n in W/m^2) on the entire solar array structure at a specific time during the day is given by Equation 33. Atmospheric attenuation is assumed to be 15% ($\tau = 0.15$). θ_i is the local solar elevation angle as seen from a specific segment of array which has an inclination angle of β_i and an orientation angle of α . In fact the orientation angle is a characteristic of the airship, and hence it is the same for all the array segments. The inclination angle β_i ranges from $\pi/2$ to 0 starting from one side (south-facing side in Figure 5) to the top of the hull, and further ranges from 0 to $-\pi/2$ for the solar strips installed from the top to the other side (north-facing side in Figure 5). Also note that, for the airship side which is in shadow, if the local solar elevation angle is less than the inclination angle for a particular solar strip ($\theta_i < \beta_i$), that portion of the solar array will be shadowed and will not produce any power.

Equation 33: Total power (solar flux) incident on the solar arrays

$$P_n = \sum_{\beta_i=\frac{\pi}{2}}^{\frac{\pi}{2}} SI(1 - \tau) \sin(\theta_i)$$

Using the geometry shown in Figure 5, the following expressions can be derived. An array segment's incident angle or local solar elevation angle (θ_i) can be computed using the equation,

Equation 34: Expression for local solar elevation angle (θ_i)

$$\sin \theta_i = \sin \theta \cos \beta_i - \sin \omega_i \sin \beta_i \cos \theta$$

where,

$$\theta = \frac{\pi}{2} - \cos^{-1}(C - D \cos \omega), \quad C = \sin \phi \sin \delta, \quad D = \cos \phi \cos \delta$$

The solar hour angle (ω) is a function of time of the day and is given by Equation 35, where time of the day (t_h) is in hours and is based on a 24-hour clock. The solar hour angle is defined such that it is 0 at noon, positive before noon, negative after noon, and each hour represents a 15° rotation.

Equation 35: Expression for solar hour angle (ω)

$$\omega = -\frac{2\pi t_h}{24} + \pi$$

The local hour angle is based on the sun's position as well as the orientation angle (α) of the airship. The expression for local hour angle is given by Equation 36, where the airship orientation angle is defined as being 0 when the airship is oriented west to east and $\pi/2$ when the airship is oriented north to south.

Equation 36: Expression for local hour angle (ω_i)

$$\omega_i = \alpha + \frac{\pi}{2} - \frac{2\pi t_h}{24}$$

2.8. External environment: Atmosphere, Wind, and Turbulence

Atmosphere

In order to use the airship system simulation for various tasks such as dynamical analysis, performance analysis and design, knowledge of vertical distribution (function of altitude) of such quantities as pressure, temperature, density, and speed of sound is required. Thus, a basic atmospheric model is essential for simulating the surrounding environment in which the airship is flying. Since the real atmosphere never remains constant at any particular time or place, a hypothetical model must be employed as an approximation to what may be expected. The model used here is based on the International Standard Atmosphere (ISA [41]). The air in the model is assumed to be devoid of dust, moisture and water vapor, and to be at rest with respect to the Earth, i.e. no winds or turbulence [40]. The wind profiles model and the turbulence models of next two sections, if required to simulate, will be added on top of this basic atmospheric model.

The ISA assumes the mean sea level (MSL) conditions as given in Table 6. The model has three zones with separate curve fits for the troposphere, the lower stratosphere, and the

upper stratosphere. The troposphere runs from the surface of the Earth to 11 km (geometric altitude). In the troposphere, the temperature T decreases linearly and the pressure p decreases exponentially. The rate of temperature decrease is called the lapse rate. In the troposphere, the curve-fits for pressure (in kPa) and temperature (in $^{\circ}\text{C}$) are as follows (geometric altitude h is in km, [42]):

Equation 37: Temperature and pressure variations in the troposphere ($h < 11 \text{ km}$)

$$\begin{aligned} T &= T_0 + \lambda_t(h - h_0) = 15 - 6.5 * hp = p_0 \left(1 + \lambda_t \frac{h - h_0}{T_0 + 273.15}\right)^{-10^3 * \left(\frac{g_0}{\lambda_t R}\right)} \\ &= 101.325 * \left(1 - \frac{6.5 * h}{288.15}\right)^{5.256} \end{aligned}$$

Table 6: International Standard Atmosphere (ISA): Mean Sea Level (MSL) conditions and other parameter values

Pressure (MSL)	$p_0 = 101325 \text{ N/m}^2 = 101.325 \text{ kPa}$
Density (MSL)	$\rho_0 = 1.225 \text{ kg/m}^3$
Temperature (MSL)	$T_0 = 288.15 \text{ }^{\circ}\text{K} (15 \text{ }^{\circ}\text{C})$
Speed of sound (MSL)	$a_0 = 340.294 \text{ m/s}$
Geometric altitude (MSL)	$h_0 = 0$
Acceleration due to gravity	$g_0 = 9.80665 \text{ m/sec}^2$
Pressure (Tropopause)	$p_t = 22.632 \text{ kPa}$
Temperature (Tropopause)	$T_t = 216.65 \text{ }^{\circ}\text{K} (-56.5 \text{ }^{\circ}\text{C})$
Geometric altitude (Tropopause)	$h_t = 11 \text{ km}$
Temperature lapse rate in troposphere	$\lambda_t = -6.5 \text{ }^{\circ}\text{C/km}$
Temperature lapse rate in upper stratosphere	$\lambda_s = 1 \text{ }^{\circ}\text{C/km}$

The lower stratosphere runs from 11 km to 20 km. In this zone, the temperature remains at a constant value of $-56.5 \text{ }^{\circ}\text{C}$, and the pressure decreases exponentially as per the equation given below (h in km and p in kPa, [42]).

Equation 38: Pressure variation in the lower stratosphere ($11 \text{ km} < h < 20 \text{ km}$)

$$p = p_t e^{-10^3 * \left(\frac{g_0(h-h_t)}{R(T_t+273.15)}\right)} = 22.632 * e^{10^3 * (1.73 - 0.157 * h)}$$

Here $p_t = 22.632 \text{ kPa}$ and $T_t = -56.5 \text{ }^{\circ}\text{C}$ are the ISA standard pressure and temperature at $h_t = 11 \text{ km}$ (Tropopause), and $R = 287.053 \text{ J/kg/K}$ is the universal gas constant. The temperature variations according to the International Standard Atmosphere are shown in Figure 6 and Figure 7, and the ISA pressure variation in the troposphere is shown in Figure 8.

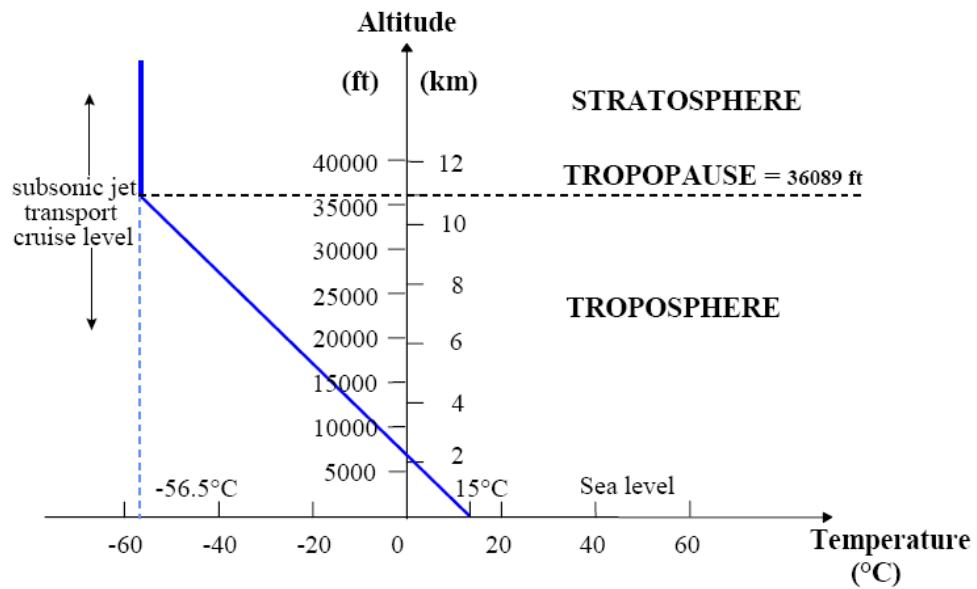


Figure 6: Temperature variation, as per ISA, for altitudes from MSL to 12 km

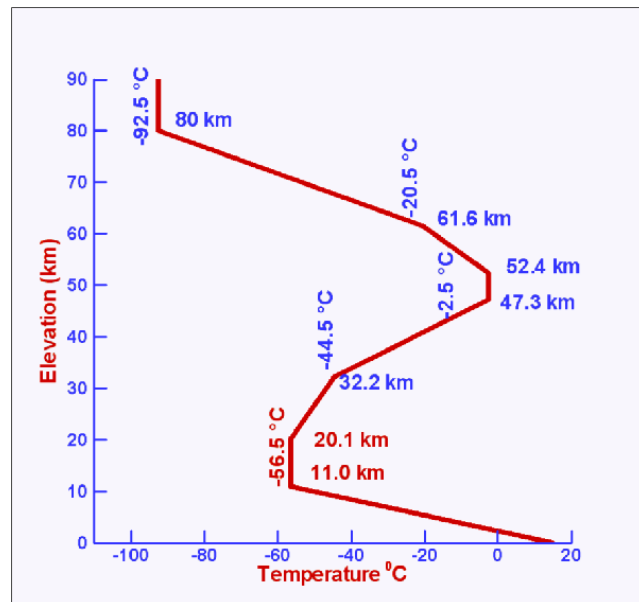


Figure 7: Temperature variation, as per ISA, for altitudes from MSL to 32 km and beyond

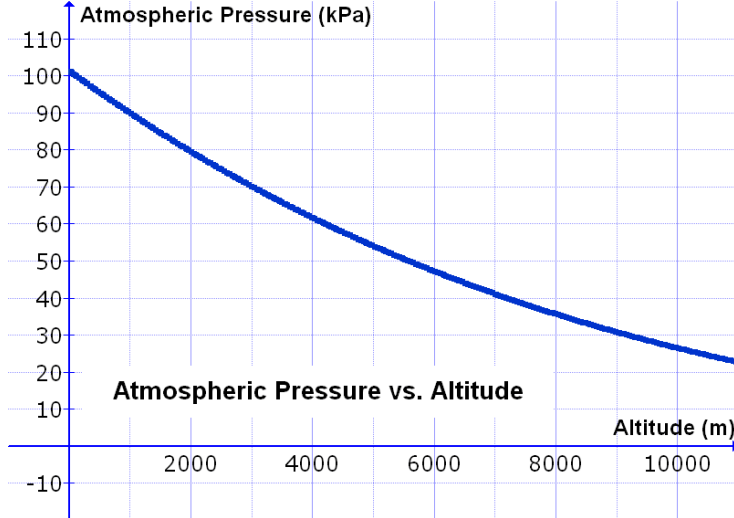


Figure 8: ISA pressure variation in the troposphere ($h < 11$ km)

The upper stratosphere model is used for altitudes above 20 km. In the upper stratosphere, the temperature increases slightly and the pressure decreases exponentially according to the equations given below (h in km, T in $^{\circ}\text{C}$, and p in kPa).

Equation 39: Temperature and pressure variations in the upper stratosphere ($h > 20$ km)

$$T = T_s + \lambda_s(h - h_s)p = p_s \left(1 + \lambda_s \frac{h - h_s}{T_s + 273.15}\right)^{-10^3 * \left(\frac{g_0}{\lambda_s R}\right)}$$

Here $p_s = 5.475$ kPa and $T_s = -56.5^{\circ}\text{C}$ are the ISA pressure and temperature at the boundary between lower and upper stratosphere ($h_s = 20$ km). In each zone, the density ρ can be calculated from the equation of state (p in kPa, T in $^{\circ}\text{C}$, and $R = 287.053$ J/kg/K):

$$\rho = \frac{p * 1000}{R * (T + 273.1)}$$

Wind profiles

Due to the large size of an airship, drag and therefore wind speeds at any particular altitude and throughout the desired period of operation are critical factors in the airship's design and capabilities. Thus, to accurately simulate the HAA system a detailed model of the wind environment is required. Wind speeds in Earth's environment depend on the particular location (longitude and latitude), time of year, and altitude. For the current HAA system simulation, the wind profiles are modeled using the data available from Strganac [43]. This contains all available wind data obtained over the years at specific locations in the US from the surface up to 31 km altitude. The data was presented seasonally and included mean, mean + 5%, mean - 5%, 95th percentile and 99th percentile winds. Two data samples, one each for the East and the West coast of US, are given in Table 7 below.

Table 7: Raw wind data sites [43]

Location	City	Latitude	Longitude	Data Collection Period	Total profiles sampled
East coast	Cape Kennedy, Florida	28°N	81°W	February 1950 to May 1970	16,424
West coast	Spokane, Washington	48°N	118°W	January 1950 to December 1970	11,144

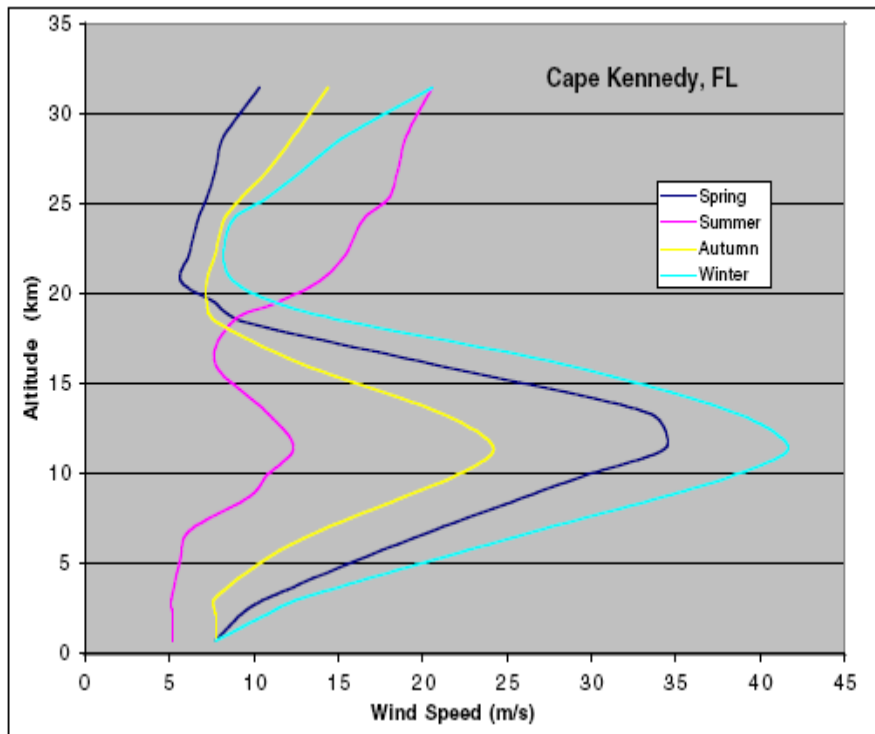


Figure 9: Mean wind profiles for Cape Kennedy, Florida during different seasons

An example of a mean wind profile is shown in Figure 9, which is for the location Cape Kennedy, Florida. This profile has been generated based on wind data collected from this location throughout the year. The wind model for this project has been taken from the work done by Colozza [20], which uses the data from Strganac [43] and provides mean and 99th percentile winds as a function of latitude and altitude. Colozza [20] has developed different models for the East and the West coast of US. For each coast, the equations are different for the four seasons. Thus, a total of 16 different equations have been generated in this work (mean and 99th percentile winds, 8 equations each). These equations represent mathematical surfaces of wind speed versus altitude versus latitude.

From Colozza [20], here we reproduce two wind profiles for the East coast of US during winter, one each for the mean and the 99th percentile wind velocity. Note that the mean wind velocity information is required to design the power and propulsion system for mean thrust

level or cruise power, and the 99th percentile wind velocity information is required to design the power and propulsion system for maximum thrust or peak power.

Mean wind velocity for winter on the East coast of US:

$$V = 0.5144(-10056.977 + 985.214629\phi - 30.129253\phi^2 + 0.12888569\phi^3 + 8.12247 \times 10^{-3}\phi^4 - 9.918 \times 10^{-5}\phi^5 + 0.05001086P + 2.31194 \times 10^{-3}P^2 - 9.575 \times 10^{-6}P^3 + 1.2515 \times 10^{-8}P^4 - 5.313 \times 10^{-12}P^5)$$

99th percentile wind velocity for winter on the East coast of US:

$$V = 0.5144(-23684.526 + 2333.24941\phi - 71.458827\phi^2 + 0.28778566\phi^3 + 0.02006288\phi^4 - 2.441 \times 10^{-4}\phi^5 - 0.3989153P + 7.1656 \times 10^{-3}P^2 - 2.462 \times 10^{-5}P^3 + 3.0389 \times 10^{-8}P^4 - 1.258 \times 10^{-11}P^5)$$

For these equations, latitude (ϕ) is in degrees, altitude is given in terms of atmospheric pressure (P , in mbar), and the wind velocity (V) is in m/s. The conversion of atmospheric pressure (P) in mbar to altitude (h) in km is given below.

$$h = -6.67 \ln \frac{P}{1118.3}$$

Note that the wind velocity equations given above are applicable only for a limited range of latitudes and altitudes. These limitations are based on the range of the data from which these equations were derived. Latitude range is from 28°N to 44°N and altitude range is from surface to 28 km. Thus, these equations can be used for various latitudes (within the limits given above) along the East coast of US to simulate winds at the operational altitude of 21.5 km that has been chosen for the current system simulation.

Wind turbulence

The model chosen to represent atmospheric turbulence is based on the set of power spectral density (PSD) functions (Equation 40 and Equation 41) of Dryden ([28], [29]). The Dryden wind turbulence model, also known as Dryden gusts, is a mathematical model of continuous gusts accepted for use by the US Department of Defense in certain aircraft design and simulation applications [27]. The Dryden model treats the linear and angular velocity components of continuous gusts as spatially-varying stochastic processes and specifies each component's power spectral density. Since the model is characterized by rational power spectral densities, exact filters can be designed that take white noise inputs and generate, as output, stochastic processes with the Dryden gusts' spectral densities.

For an aircraft flying at a speed V through a frozen turbulence field with a spatial frequency of Ω radians per meter, the circular frequency ω is calculated by multiplying V by Ω . The Dryden model is characterized by power spectral densities for three linear velocity components of gusts (u_g, v_g, w_g):

Equation 40: Power spectral density functions for three linear velocity components of gusts

$$\Phi_{u_g}(\omega) = \sigma_u^2 \frac{2L_u}{\pi V} \frac{1}{1 + \left(L_u \frac{\omega}{V}\right)^2}$$

$$\Phi_{v_g}(\omega) = \sigma_v^2 \frac{2L_v}{\pi V} \frac{1 + 12 \left(L_v \frac{\omega}{V}\right)^2}{\left(1 + 4 \left(L_v \frac{\omega}{V}\right)^2\right)^2}$$

$$\Phi_{w_g}(\omega) = \sigma_w^2 \frac{2L_w}{\pi V} \frac{1 + 12 \left(L_w \frac{\omega}{V}\right)^2}{\left(1 + 4 \left(L_w \frac{\omega}{V}\right)^2\right)^2}$$

where σ_j and L_j are the turbulence intensity and scale length, respectively, for the j^{th} linear velocity component. The gust angular velocity components (p_g, q_g, r_g) are defined as the variations of the linear velocity components along different vehicle axes as given below.

$$p_g = \frac{\partial w_g}{\partial y}, \quad q_g = \frac{\partial w_g}{\partial x}, \quad r_g = -\frac{\partial v_g}{\partial x}$$

The power spectral densities for the angular velocity components are as follows:

Equation 41: Power spectral density functions for three angular velocity components of gusts

$$\Phi_{p_g}(\omega) = \frac{\sigma_w^2}{2VL_w} \frac{0.8 \left(\frac{2\pi L_w}{4b}\right)^{\frac{1}{3}}}{1 + \left(\frac{4b\omega}{\pi V}\right)^2}$$

$$\Phi_{q_g}(\omega) = \frac{\pm \left(\frac{\omega}{V}\right)^2}{1 + \left(\frac{4b\omega}{\pi V}\right)^2} \Phi_{w_g}(\omega)$$

$$\Phi_{r_g}(\omega) = \frac{\mp \left(\frac{\omega}{V}\right)^2}{1 + \left(\frac{3b\omega}{\pi V}\right)^2} \Phi_{v_g}(\omega)$$

The variable b represents aircraft wingspan. It has to be appropriately redefined for airships before applying this model to our case of airship system simulation.

To introduce such air turbulence into the airship system simulation, signals with Dryden model's power spectral densities have to be generated in each of the six velocity components. If a linear time-invariant system with transfer function $G(s)$ is driven by a white-noise input that has unit variance, the power spectral density of its output $y(t)$ is given by

$$\Phi_y(\omega) = |G(i\omega)|^2, \text{ where } i^2 = -1$$

For rational power spectral densities, such as that of the Dryden model, a suitable transfer function can be found for each velocity component whose magnitude squared evaluated along the imaginary axis is the corresponding power spectral density. These transfer functions (forming filters) for the three linear and three angular velocity components, as per Dryden model, are given below.

Equation 42: Forming filters for six velocity components of gusts based on Dryden model

$$\begin{aligned} G_{u_g}(s) &= \sigma_u \sqrt{\frac{2L_u}{\pi V}} \frac{1}{1 + \frac{L_u}{V}s}, & G_{v_g}(s) &= \sigma_v \sqrt{\frac{2L_v}{\pi V}} \frac{1 + \frac{2\sqrt{3}L_v}{V}s}{\left(1 + \frac{2L_v}{V}s\right)^2} \\ G_{w_g}(s) &= \sigma_w \sqrt{\frac{2L_w}{\pi V}} \frac{1 + \frac{2\sqrt{3}L_w}{V}s}{\left(1 + \frac{2L_w}{V}s\right)^2}, & G_{p_g}(s) &= \sigma_w \sqrt{\frac{0.8}{V}} \frac{\left(\frac{\pi}{4b}\right)^{\frac{1}{6}}}{(2L_w)^{\frac{1}{3}} \left(1 + \frac{4b}{\pi V}s\right)} \\ G_{q_g}(s) &= \frac{\pm \frac{s}{V}}{1 + \frac{4b}{\pi V}s} G_{w_g}(s), & G_{r_g}(s) &= \frac{\mp \frac{s}{V}}{1 + \frac{3b}{\pi V}s} G_{v_g}(s) \end{aligned}$$

Driving these filters with independent, unit variance, band-limited white noise yields outputs with power spectral densities that match the spectra of velocity components of the Dryden model. These outputs can, in turn, be used as wind disturbance inputs to the airship dynamics [30], as part of the airship system simulation.

The Dryden model is parameterized by length scale (L_j) and turbulence intensity (σ_j). The combination of these two parameters determine the shape of the power spectral densities and therefore, the quality of the model's fit to spectra of observed turbulence. Many combinations of length scale and turbulence intensity give realistic power spectral densities in the desired frequency ranges. The US Department of Defense specifications include choices for both parameters, including their dependence on altitude [27]. For high altitude airships, the specifications corresponding to the “medium/high altitudes” range ($h > 2000$ feet) apply. The length scales and turbulence intensities are based on the assumption that the turbulence is isotropic. The length scales are represented by the following equation.

$$L_u = 2L_v = 2L_w = 1750 \text{ ft}$$

The turbulence intensities ($\sigma_u = \sigma_v = \sigma_w$) are parameterized by the probability of exceedance or the turbulence severity. A plot of turbulence intensity versus altitude (provided in the military specifications [27]) showing lines of constant probability of exceedance and ranges corresponding to different turbulence severities is given in Figure 10. The turbulence axes orientation in this region is defined as being aligned with the wind frame. A mean wind profile is generated based on the models discussed towards the end of this section. The

turbulent wind velocity profiles are generated as stochastic processes and superimposed on this background wind. These wind speeds have to be considered while calculating angle of attack and sideslip angle of the airship (Equation 2 to Equation 7).

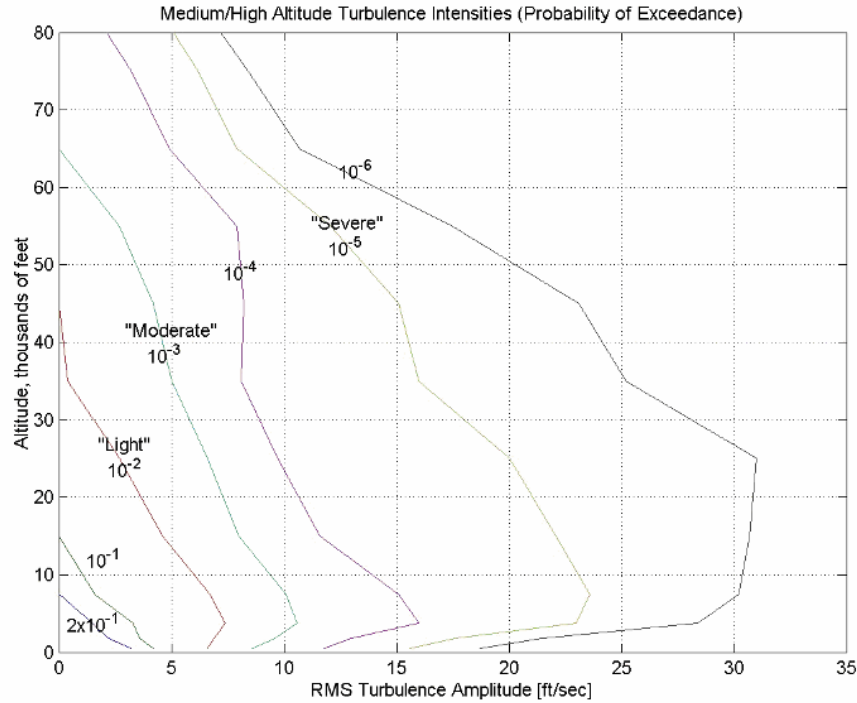


Figure 10: Turbulence intensity versus altitude [27]

2.9. Power and Propulsion System (PPS): PV arrays

The power and propulsion systems consist of all the components that collect, generate, and store energy and convert that energy into useable power and thrust. The propulsion system is the main power-consuming function on the airship, and hence the power and propulsion systems are intimately dependent on each other. Thus, to maximize efficiency and to optimize the airship design, they need to be designed and operated as a single system. Therefore, they will be referred to as a single system throughout this report.

The particular choice of power and propulsion system is driven by the specific requirements for our application (High Altitude Airship): long endurance, almost fully autonomous and use of renewable energy. The power and propulsion system chosen here is a photovoltaic/fuel-cell system powering electric motors to drive a propeller for generating thrust [20]. A hydrogen-oxygen-based fuel-cell/electrolyzer system has been identified as the storage and production system. The power and propulsion system can be broken down into individual components. The characteristics of each of these components must be known in order to size the system for various power/thrust requirements. Also, it must be understood how the components scale to different power or thrust levels.

The main components of this power and propulsion system are listed below.

- Photovoltaic Array
- Fuel Cell (Hydrogen/Oxygen, PEM)
- Electrolyzer
- Power Management
- Electric Motors / Gearbox
- Propeller

Due to the large size of a high altitude airship, a modular approach to the power and propulsion system design has been selected. The modular approach minimizes the need for long wire and piping runs within the airship, and provides redundancy in the systems. Each modular system would utilize a segment of the photovoltaic array that would be dedicated to its operation. Each modular unit would also have its own fuel cell, electrolyzer, gas storage tanks, control electronics, thermal management system, electric motors and propellers. The different components of this system are shown in Figure 11. Another advantage of such a modular system is that it allows more versatility while scaling the airship.

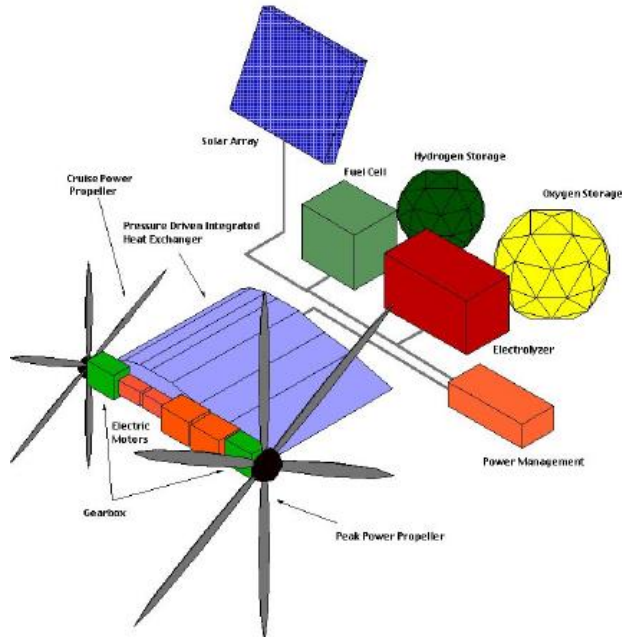


Figure 11: Component breakdown of a power and propulsion system module [20]

The components in each module can be scaled to meet a specific thrust need. However, the number of modules used on the airship can also be varied. Depending on the airship payload requirements and airship size, two, four, six or more system modules can be utilized. The ability to scale the system modules and to vary the numbers that are present on the airship enables significant flexibility in optimizing the power and propulsion system design. In the rest of this section, general characteristics of various components of a single power-and-propulsion-

system module are further described ([21], [22], [23]), and appropriate mathematical models for each of the components are identified for implementation in our HAA system simulation.

Solar PV array

The sun is the main power source for the airship, and the solar PV arrays are the means of converting this incoming energy to a useable form. Enough energy must be collected during daylight hours to meet the power needs of the complete day and night period. As per the baseline design for the system simulation, thin film arrays, which are lightweight and flexible, are to be used, and they are to be installed on the upper-half surface of the hull envelope.

The output of the solar array is determined by the incident solar radiation on the array, the geometry of the airship, and the performance characteristics of the array. The incident solar radiation analysis, given in Section 2.7, along with the efficiency of the solar array can be used to determine the output power profile for the array at various latitudes, times during the year, and airship orientations. Let S be the total surface area of the airship hull and p_{sc} be the percentage of the surface area which is covered with solar cells. With reference to Equation 31 to Equation 36, the total power output at any particular time instant during any day from the entire solar array structure is given by the following equation ([2], [20]):

Equation 43: Power output from the entire solar array structure

$$P_{sc} = \eta_{sc} * S * p_{sc} * P_n = \eta_{sc} * S * p_{sc} * \sum_{\beta_i=\frac{\pi}{2}}^{\beta_i=-\frac{\pi}{2}} f_{sh} * SI * (1 - \tau) * \sin(\theta_i)$$

Here η_{sc} is the solar cell efficiency, SI is the solar intensity received at the Earth's orbital location on any particular day of the year, $\tau = 0.15$ models the atmospheric attenuation, and β_i and θ_i are, respectively, the inclination angle and local solar elevation angle of each solar strip installed on the airship's upper surface (refer Section 2.7). Finally $f_{sh} = 0$ or 1 (a function of β_i and θ_i) is a factor which takes care of the fact that solar strips on one side of the hull, which are not in the line-of-sight of the sun, will actually be shadowed and will not be producing any power. The total energy generated over a 24 hour period is found by integrating P_{sc} from sunrise to sunset.

The shadowing affects the array output but it is mostly a concern in how the arrays will actually be wired on the airship. The output current of a given string of solar cells wired together in series will be equal to the lowest current producing cell in the string. If a string has 10 cells and one is shadowed, then this has the same effect as shadowing all 10 cells. Therefore, the wiring scheme for the solar array will need to take into account the shadowing of the array throughout the day. A wiring scheme will have to be devised that minimizes the effect of shadowing on the array output. The model described here is based on the assumption that only the shadowed solar cells do not produce any power. It does not take into account the combined effects of shadowing and series wiring of the cells.

It should be noted that the output profiles do not take into account any land features such as mountains or atmospheric features such as clouds that could obscure the sun near sunrise or sunset. Since the altitude of the airship is fairly high, these effects would be minimal and occur at times of low solar elevation angles. Therefore, they should not have a significant effect on the overall performance of the solar array.

2.10. PPS: Electrolyzer, Storage, and Fuel Cell

Fuel cell

The fuel cell is an electrochemical device that produces electricity through the combination of hydrogen and oxygen. The type of fuel cell that has seen the most commercial development and therefore would be a good candidate for the high altitude airship application is a polymer electrolyte membrane (PEM) fuel cell. Ideally the theoretical output voltage of a single fuel cell “cell” is 1.16 volts. This voltage represents the case in which all (100%) of the energy in the fuel is being turned into electricity. However, during real world operation this voltage will drop to some level below this ideal limit. The difference between this ideal voltage and the actual cell operating voltage translates into the efficiency of the fuel cell. For example, if the individual cell is operating at 0.7 volts then it is operating at approximately 60% efficiency.

The fuel cell stack itself is only one of the components that make up the fuel cell system. The complete system consists of the fuel cell stack, reactant tanks, valves, regulators, filters, piping and control electronics. For the present HAA system simulation, the conversion efficiency of fuel to electricity is assumed to be 70% ([20], [22]).

Electrolyzer and Energy storage system

An electrolyzer is a device that will break apart water into its constituent elements, hydrogen and oxygen. It works on the same principle as the fuel cell except, in this case electricity is put in and hydrogen and oxygen are generated, which is the reverse of what a fuel cell does. The electrolyzer will be used to fill and maintain the hydrogen and oxygen storage tanks with a sufficient amount of reactants to maintain continuous operation of the airship.

The power to run the electrolyzer will come entirely from the solar array. Whenever the fuel cell is operating, the electrolyzer will not be operational. Due to the efficiency losses in the fuel cell and electrolyzer, operating the fuel cell to run the electrolyzer to produce hydrogen will result in a net decrease in hydrogen. The electrolyzer will be sized to operate at the maximum output power of the solar array. This is necessary in order to fully utilize the solar array and maintain the energy balance for the airship operation. Thus the energy storage system consists of the electrolyzer unit, a heated water supply tank, and hydrogen and oxygen connections to their respective storage tanks. For the present HAA system simulation, the electrolyzer is assumed to be operated at a 70% efficiency level ([20], [22]).

Thus, by integrating P_{sc} (Equation 43) as a function of time from sunrise to sunset, the total energy that can be generated from the entire solar array structure in a 24 hour period, E_{sc} can be calculated as given below.

$$E_{sc} = \int_{t_i}^{t_f} P_{sc} * dt$$

Here t_i corresponds to a time just after sunrise and t_f corresponds to a time just before sunset. This energy is getting stored in the electrolyzer system in the form of hydrogen and oxygen. Since the electrolyzer system is operating at a 70% efficiency level, the equivalent energy that gets stored in the hydrogen and oxygen tanks is $E_{es} = 0.7 * E_{sc}$. Further, since the fuel-to-electricity conversion efficiency of the fuel cell system is 70%, the final energy that is available for a 24 hour period to run the propulsion system and other payloads is $E_{fc} = 0.7 * E_{es} = 0.49 * E_{sc}$.

2.11. PPS: Electric motor and Gearbox

Electric motor

An electric motor is used to drive the propellers that generate thrust. The efficiency and operational capabilities of the motor are major factors in the power consumption and overall capabilities of the airship. Since the solar array and the fuel cells put out DC power, the main power bus on the airship is DC. However, either of the two main types of electric motors, AC and DC, can be considered for the airship application. The different possible options are the standard DC motor, a brushless DC motor, or an AC induction motor.

Typically, the motor efficiency will vary as a function of the motor power and its RPM. A typical motor would operate efficiently at or near its design RPM, and will drop off in efficiency as it is operated off this design point. Another option is to use a gearbox with 95% efficiency to drive the propeller at an off-design RPM. Here both the electrical and mechanical parts of a DC electric motor are modeled, in terms of second-order ODEs, as described below.

DC motors (machines) consist of one set of a current-carrying conductive coil, called an armature, inside another set of a current-carrying conductive coils or a set of permanent magnets, called the stator. The input voltage can be applied to armature terminal (armature current-controlled DC motor), or to the conductive-coils terminals (field current controlled DC motor). This current will generate lines of flux around the armature and affect the lines of flux in the air gap between two coils, generating two magnetic fields, the interaction between these two magnetic fields (attract and repel one another) within the DC motor, results in a torque which tends to rotate the rotor (the rotor is the rotating member of the motor). As the rotor turns, the current in the windings is commutated to produce a continuous torque output resulting in motion.

DC machines are characterized by their versatility. By means of various combinations of shunt-, series-, and separately-excited field windings, they can be designed to display a wide variety of volt-ampere or speed-torque characteristics for both dynamic and steady-state operation. Because of the ease with which they can be controlled, systems of DC machines have been frequently used in many applications requiring a wide range of motor speeds and a precise output motor control [35]. The selection of motor for a specific application is dependent on many factors, such as the intention of the application, correspondingly allowable variation in speed and torque and ease of control, etc.

Here we model an armature-controlled Permanent Magnet DC (PMDC) motor. The PMDC motor is an example of an electromechanical system with both electrical and mechanical functional components. An equivalent simplified representation of this armature-controlled DC motor is shown in Figure 12.

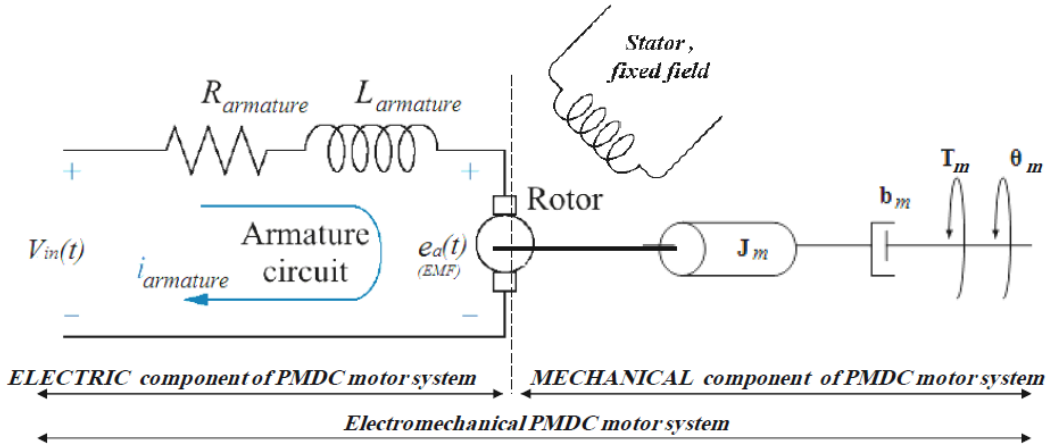


Figure 12: Electromechanical PMDC motor system

Electrical Characteristics of PMDC Motor

Applying a voltage to the motor coils produces a current in the armature. The torque developed by the motor, T_m is related to the armature current, i_a by a torque constant, K_t and is given by the following equation.

$$\text{Motor Torque, } T_m = K_t * i_a$$

The back electromotive-force (EMF) voltage e_a is induced due to the rotation of the armature windings in the fixed magnetic field, the polarity of the EMF voltage being opposite to the current that produces the motion. The EMF is related to the motor-shaft angular speed, ω_m by a linear relation as given below:

$$e_a(t) = K_b \frac{d\theta_m(t)}{dt} = K_b \omega_m$$

Here, K_b is the EMF constant. The differential equation that describes the electrical characteristics of a PMDC motor is as given below.

$$V_{in} = R_a i_a + L_a \frac{di_a}{dt} + K_b \frac{d\theta_m}{dt}$$

Mechanical characteristics of PMDC motor

The torque developed by the motor drives the motor-shaft-load system resulting in an angular velocity, $\omega_m = \frac{d\theta_m}{dt}$, the value of which depends on the moment of inertia J_m and the viscous damping b_m of the motor-shaft-load combination. The mathematical model in the form of differential equation which describes the mechanical characteristics of a PMDC motor system is as given below.

$$K_t * i_a - T_{Load} - J_m \frac{d^2\theta}{dt^2} - b_m \frac{d\theta}{dt} = 0$$

2.12. PPS: Propeller design and dynamics

The operation of the propeller is one of the more critical elements of the propulsion system. The efficiency and capabilities of the propeller directly affect the sizing of the power system as well as the other propulsion system components. The majority of the power produced and consumed by the airship is for the production of thrust. From the solar array to the energy storage system to the motors, the primary function of all these systems and their components is to drive the propellers. For the present work, the propeller model is chosen based on the work done by Colozza [21].

As shown in Figure 11, a dual propeller system is used. The dual propeller system allows thrust to be generated efficiently over a wide range of operational conditions. It also adds some redundancy to the propulsion system. The dual propeller system includes a smaller propeller that can be used for station-keeping under mean or low wind conditions and a larger propeller that can be used for high wind conditions and for producing increased thrust while maneuvering at high altitudes. The smaller propeller also provides a more efficient means of generating thrust and control at lower altitudes.

The important steps involved in and the different features of the propeller design achieved by Colozza ([20], [21]) are listed below.

- a) The propellers are designed for a given airship configuration and operational location.
- b) Since the propellers must be capable of producing the thrust necessary to overcome the wind-induced drag on the airship, the mean and 99th percentile wind speeds of Section 2.8 are used to size them.
- c) First, a general propeller configuration, representative of a high altitude propeller design and consistent with the thrust levels required by the airship, is chosen.

- d) Design parameters such as twist and chord-length variation along the blade and airfoil type are chosen for a particular flight environment, and they are not altered to optimize the propeller for a specific airship configuration.
- e) Other parameters such as number of blades, propeller diameter, and operational RPM are all adjustable to meet the needs of the specific airship configuration and flight environment.
- f) Propeller performance is generated using a vortex theory analysis code [21] for propeller configurations with 4, 5 and 6 blades.

The propeller geometry is given by the variation of chord length (c) and twist (β) along the length of the blade from the hub to the propeller tip.

Equation 44: Propeller blade geometry

$$c = (0.084241 - 0.85789r + 4.7176r^2 - 9.6225r^3 + 8.5004r^4 - 2.7959r^5)d\beta \\ = \Phi + 0.4387 + 0.3040r - 3.9616r^2 + 5.1180r^3 - 1.6284r^4 - 0.3244r^5$$

Here the blade station (r) is a normalized distance along the blade given by 0 at the center of the hub and 1 at the tip, and d is the diameter of the propeller. Since a variable-pitch propeller blade is assumed, the whole blade can be turned by the given pitch angle (Φ).

The airfoil selected for the propeller is the SP-8000PT, which has a good low-Reynolds-number performance that is desirable for high altitude operation [44]. The lift coefficient (C_l) versus angle of attack (α) and the lift coefficient versus drag coefficient (C_d) curves for this airfoil are shown in Figure 13 and Figure 14, respectively.

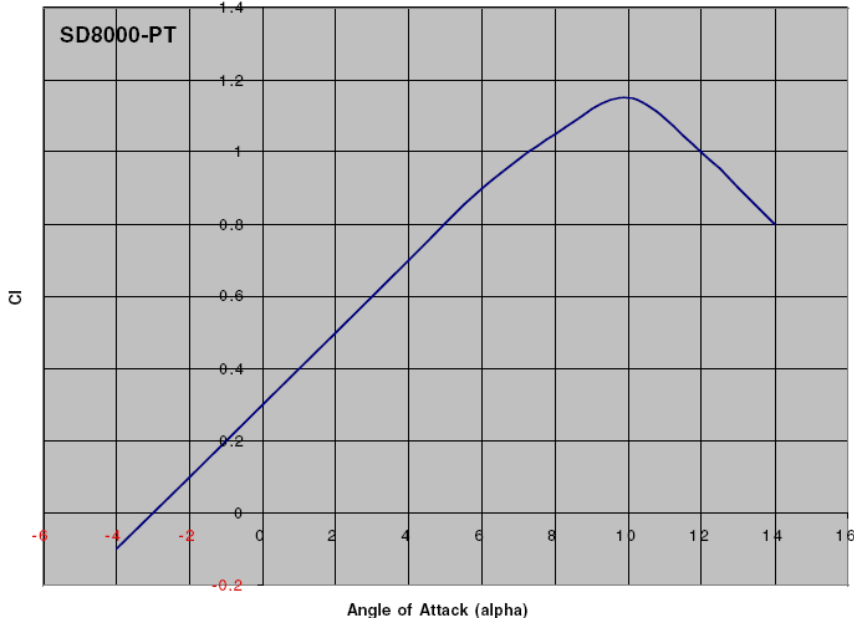


Figure 13: Lift coefficient (C_l) versus angle of attack (α) curve for SD8000-PT airfoil at a Reynolds number of 3×10^5 [44]

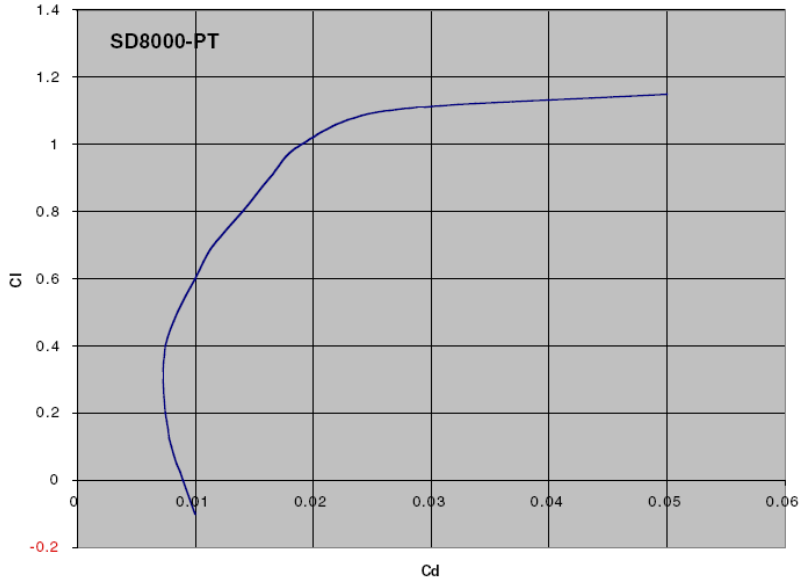


Figure 14: Lift coefficient (C_l) versus drag coefficient (C_d) for SD-8000PT airfoil at a Reynolds number of 3×10^5 [44]

Thus the operational thrust and power curves of this propeller can be obtained using the geometry relationships of Equation 44 and the airfoil data from Figure 13 and Figure 14. Colozza ([20], [21]) has done this for propeller configurations with 4, 5 and 6 blades. Here we reproduce the results for a 6-blade propeller (Figure 15 and Figure 16).

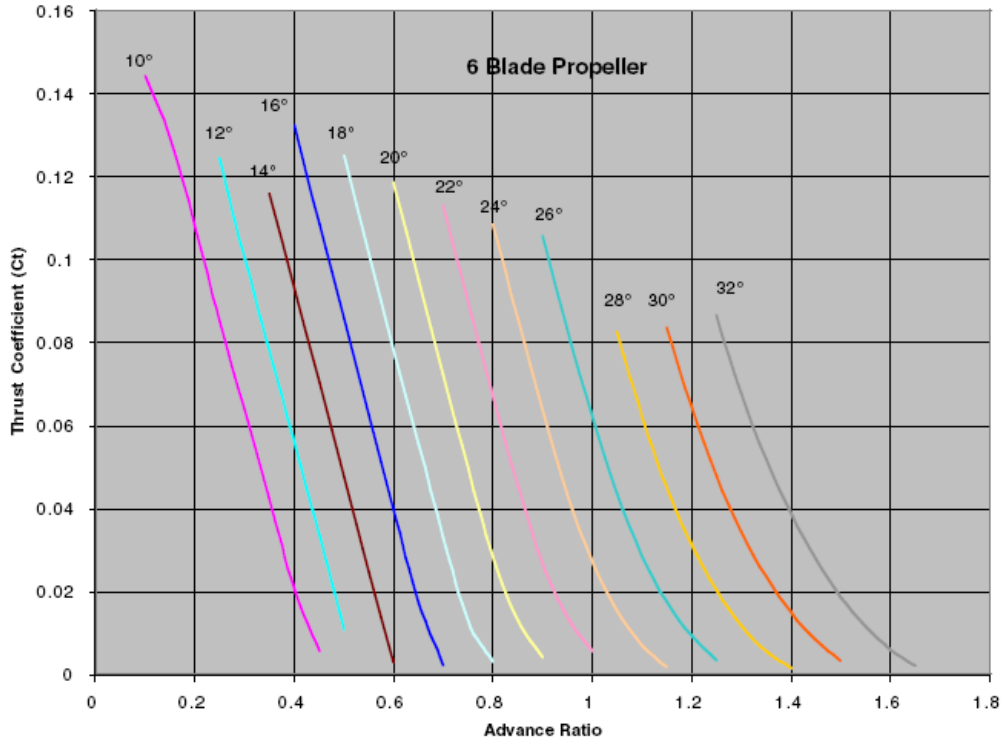


Figure 15: C_t versus J for a 6-blade propeller at different pitch angles

The curves in Figure 15 and Figure 16 show the thrust coefficient (C_t) and the power coefficient (C_p) as a function of the advance ratio (J) for a 6-blade propeller at various pitch

angles. The operational thrust of the propeller can be varied by changing the pitch of the propeller, its RPM or both. The change in pitch angle is accomplished by rotating the propeller blade, thereby adjusting the angle of attack of the propeller airfoil to the incoming air stream. In conclusion, the 6-blade propeller characteristics model includes the performance maps of Figure 15 and Figure 16 and the additional equations given below which define its various parameters such as thrust coefficient (C_t), power coefficient (C_p), advance ratio (J), propeller efficiency (η_{pr}) and propeller RPM.

Equation 45: Propeller model equations

$$C_t = \frac{T_{pr}}{\rho \left(\frac{\text{RPM}}{60}\right)^2 d^4}, \quad C_p = \frac{P_{pr}}{\rho \left(\frac{\text{RPM}}{60}\right)^3 d^5}$$

$$J = \frac{V}{\left(\frac{\text{RPM}}{60}\right) d}, \quad \text{RPM} = \frac{60}{\pi d} \sqrt{(MV_s)^2 - V^2}, \quad \eta_{pr} = \frac{C_t}{C_p} J$$

Note that ρ is the local atmospheric density and V is the air-reference speed of the airship. Here the thrust and power coefficients are expressed as a function of the thrust produced by the propeller (T_{pr}) and the power required to drive the propeller (P_{pr}), respectively. Propeller RPM is based on the maximum tip speed allowed for a given propeller diameter. The tip speed is calculated as the product of speed of sound (V_s) and Mach number (M) of the propeller tip. Maintaining a subsonic tip speed is necessary for the propeller's stability and to achieve higher propeller efficiency (η_{pr}).

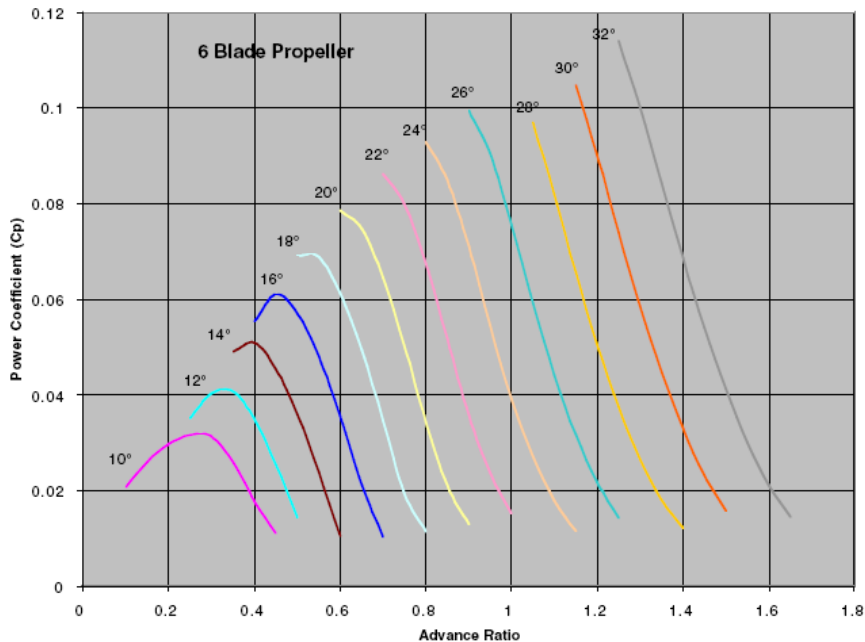


Figure 16: C_p versus J for a 6-blade propeller at different pitch angles

Using the information on airship drag that is generated either due to winds or due to movement of the airship at a given speed, Figure 15, Figure 16 and Equation 45 are used to

determine the required diameter of the propeller, its operational RPM, and the power required to generate the desired amount of thrust. While designing the propeller for a particular airship configuration, the primary objective is to maximize propeller efficiency.

In the present airship system dynamics model, the mathematical model used to describe the propeller dynamics and performance is essentially based on the above propeller characteristics model. In addition, the pitch angle variation of the propeller blades is modeled as a first-order transfer function with a specific time constant. Also, while modeling the mechanical part of the PMDC motor (Section 2.11), the propeller's (load) moment of inertia (J_p) and viscous damping (b_p) are considered along with those of the DC motor.

3. Simulink model development

In this section and the next, development of the entire Airship System Dynamics and Control Simulink model is described using Simulink block diagrams (image snapshots) and/or validation results of its essential components and subsystems. At the topmost level, the general system architecture is as given in Figure 17. The four essential functional components of this system are flight dynamics, power, propulsion, and controls. Each of the first three components is discussed below in separate subsections. The fourth component, i.e. controls, is discussed along with the full system integration results of Section 4.

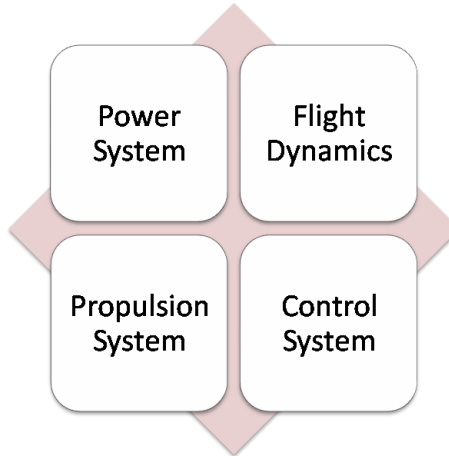


Figure 17: The four essential functional components of an airship's system dynamics

3.1. Airship flight dynamics

A block-diagram representation of various components of the airship flight dynamics model and their interconnections is given in Figure 18. Simulink models of each of these components are briefly described below.

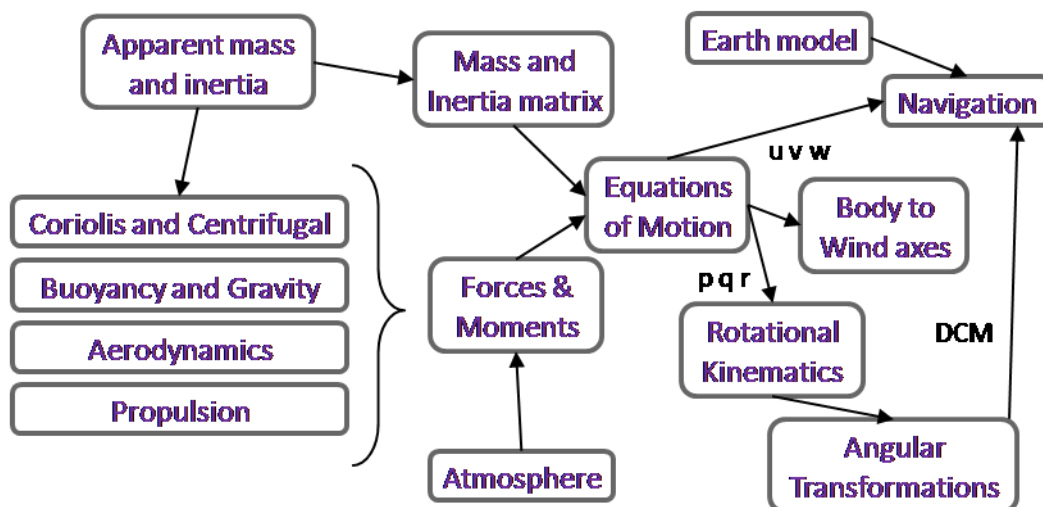


Figure 18: Block diagram of airship's flight dynamics model

3.1.1. Forces and Moments: Aerodynamics

The top-level block diagram of ‘Aerodynamics’ model is shown in Figure 19 below. This model calculates the forces and moments acting on the airship due to aerodynamic effects. The inputs to the model are angle of attack (α), sideslip (β), speed (V), density (ρ), control surface deflections and angular velocity vector.

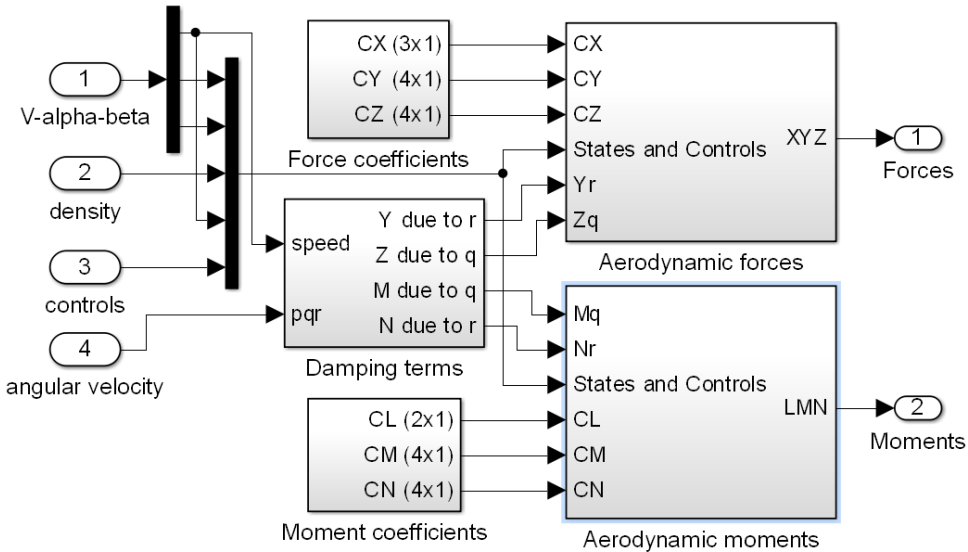


Figure 19: Aerodynamics model

The setup used for validating the ‘Aerodynamics’ system is given in Figure 20 below.

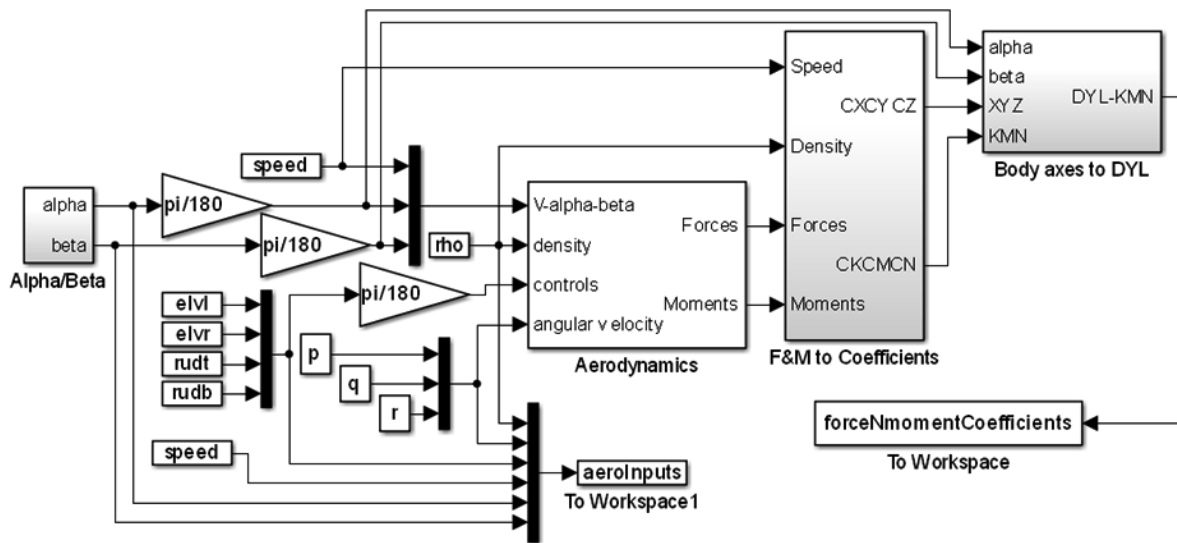


Figure 20: Validation of Aerodynamics model

Validation results are shown in Figure 21, and the ‘Pitching moment’ subsystem, one of the components of the ‘Aerodynamics’ model is shown in Figure 22. The validation results consist of the plots of drag-coefficient (C_D), lift-coefficient (C_L), pitching moment coefficient (C_m) and rolling moment coefficient (C_l) as a function of angle of attack (AoA). For zero AoA,

drag is a minimum and lift coefficient is zero. Pitching moment is positive for positive AoA and negative for negative AoA, and rolling moment does not depend on AoA.

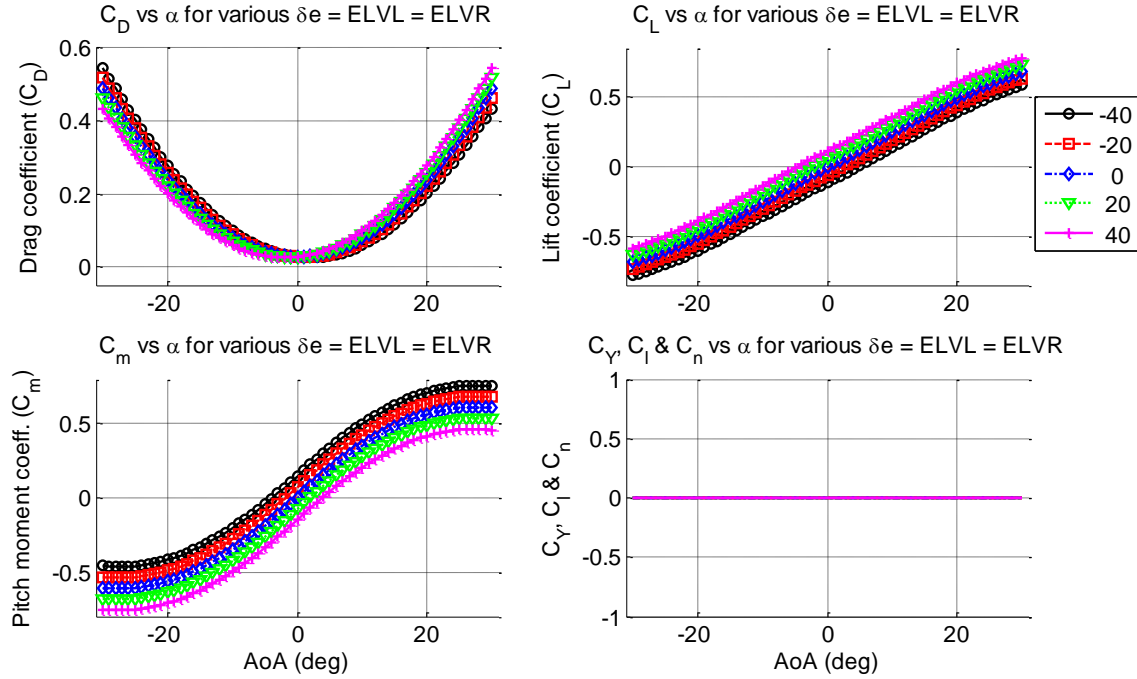


Figure 21: Validation results for Aerodynamics model

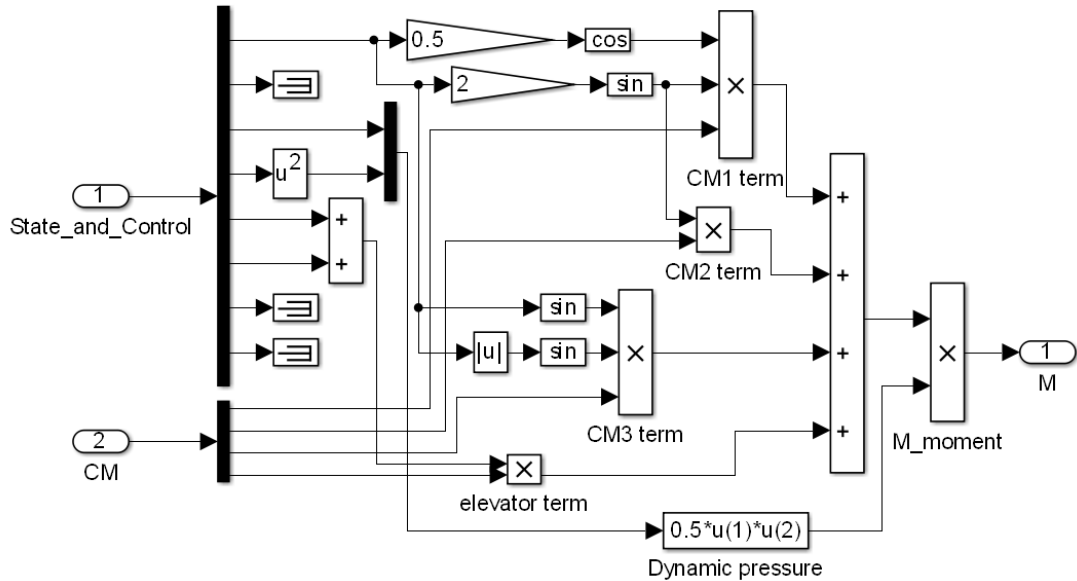


Figure 22: Pitching Moment subsystem (Aerodynamics)

3.1.2. Forces and Moments: Buoyancy and Gravity

The setup used for validating the ‘Buoyancy & Gravity’ model is given in Figure 23 below. The “Buoyancy & Gravity” model determines the forces and moments acting on the airship due to aerostatic and gravitational effects. The forces and moments along each of the axes are

the outputs, whereas the inputs to the model are pitch angle (θ), roll angle (ϕ), density (ρ) and airship's total mass (m).

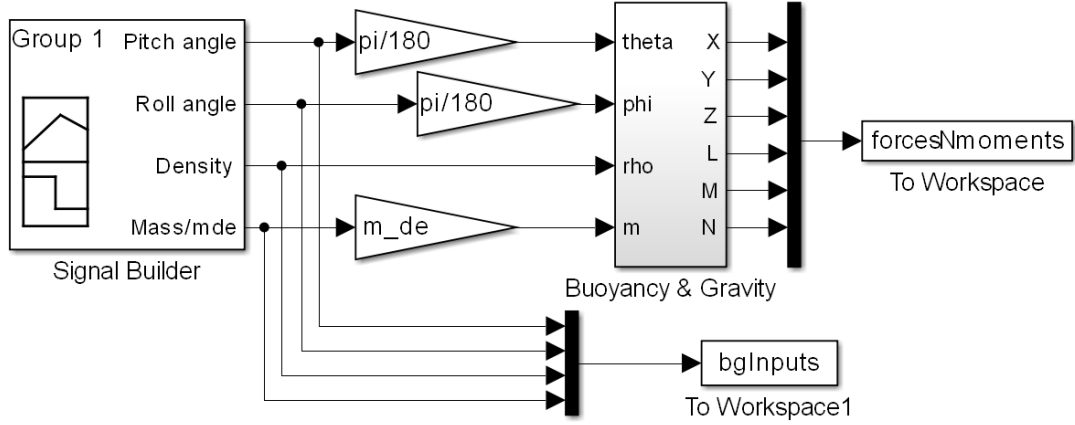


Figure 23: Validation of ‘Buoyancy & Gravity’ model

Validation results are shown in Figure 24, and the ‘Pitching moment’ subsystem, one of the components of the ‘Buoyancy & Gravity’ model is given in Figure 25. For validating the model, seven different combinations of mass, density, roll angle and pitch angle have been considered (top two plots of Figure 24). The bottom two plots of Figure 24 shows the values of buoyancy and gravity forces and moments for these different combinations.

For example, in the first case, pitch angle is 90^0 , roll angle is 45^0 , density of air is non-zero, and mass is kept zero. Thus, we have zero force along Y and Z axes and a positive force along X direction. Similarly, pitching moment is positive, whereas roll and yaw moments are zero. (For validation purposes, centre of gravity position with respect to the body frame origin (CV) is taken as $a_x = 5$ m and $a_z = 10$ m, and centre of buoyancy position is taken as $b_x = 5$ m and $b_z = 5$ m).

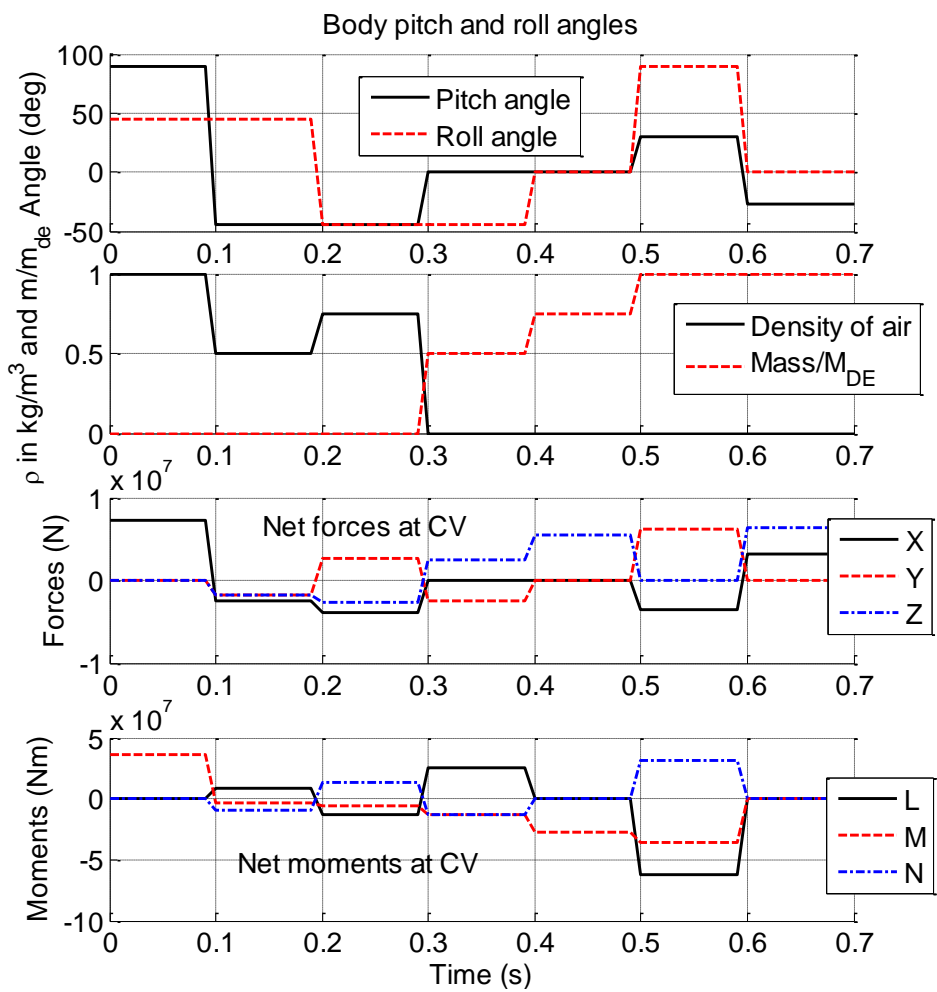


Figure 24: Validation results for ‘Buoyancy & Gravity’ model

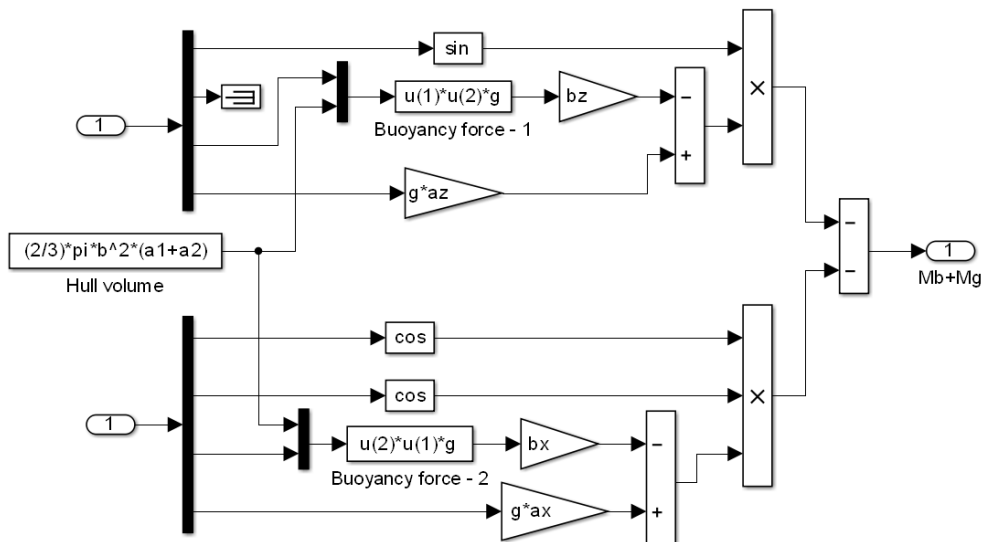


Figure 25: Pitching Moment subsystem (Buoyancy & Gravity)

3.1.3. Forces and Moments: Propulsive F&M

This model determines the forces and moments acting on the airship due to the propulsive forces. The subsystem which calculates the force components is shown in Figure 26, and the one which calculates the moment components is shown in Figure 27. Note that the present airship configuration has four propulsors (two propulsors forward of the CG and two propulsors rearward of the CG). Thus the propulsive force and moment components have four contributions each.

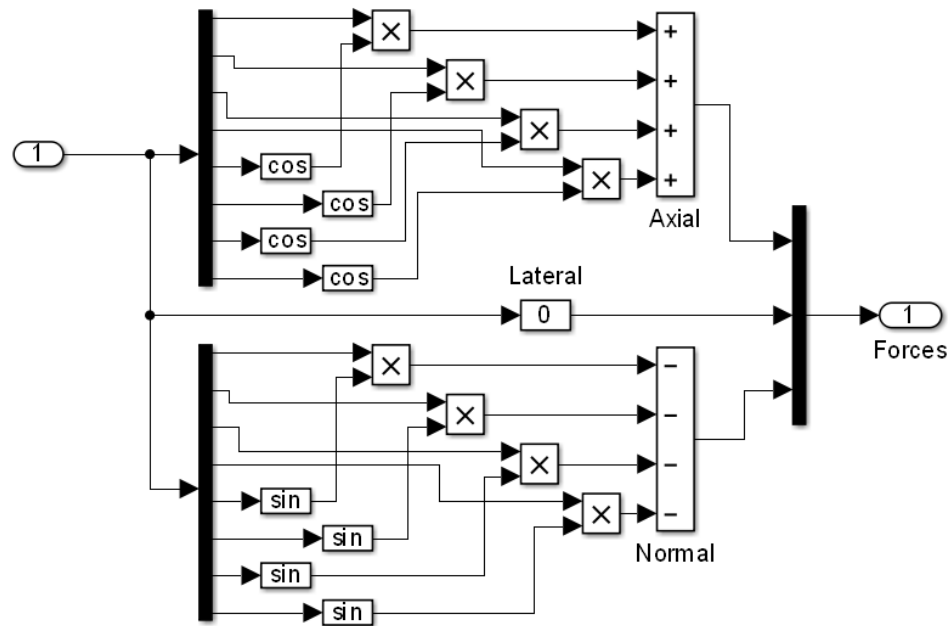


Figure 26: Simulink model of ‘Propulsive Forces’

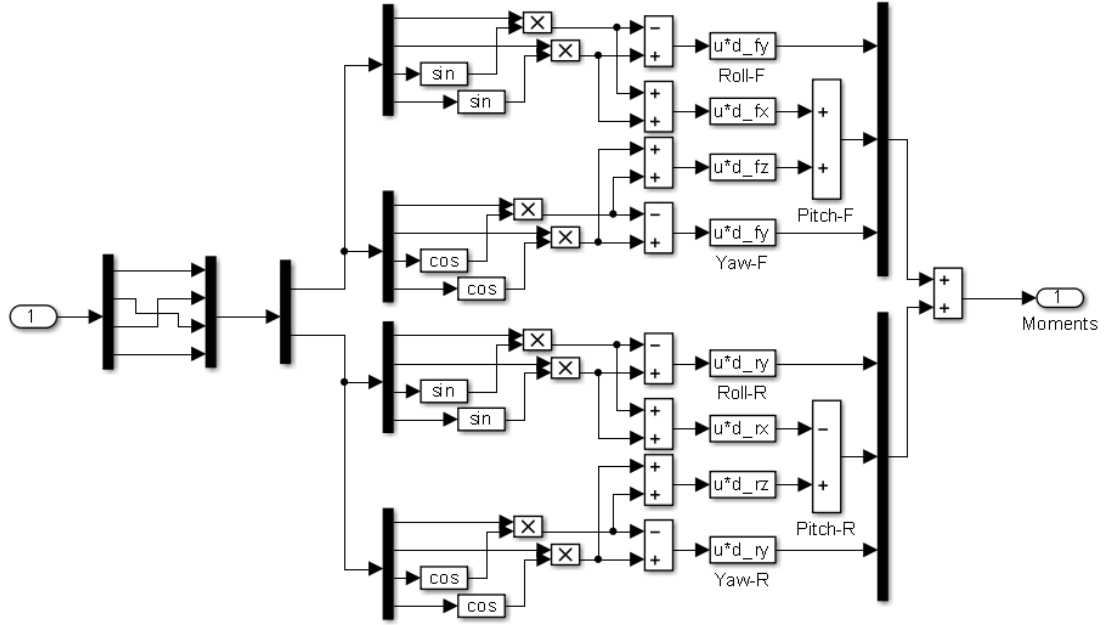


Figure 27: Simulink model of ‘Propulsive Moments’

The outputs of the propulsion model are the forces in X and Z direction (Y force is always zero) and the moments about all three axes, while the inputs to the model are the two thrusts (front and rear) on starboard side, the two thrusts on port side, and the corresponding thrust angles. The setup used for validating the ‘Propulsive F&M’ model is given in Figure 28 below, and the corresponding validation results are shown in Figure 29.

During validation, the same set of inputs has been given both to the front and rear propulsors. The top-left plot of Figure 29 shows the input parameters of the front propulsors whereas the top-right plot shows the same for the rear propulsors. The net propulsive forces and moments are shown in the bottom-left and bottom-right plots of Figure 29, respectively.

For validating the model, seven different combinations of the thrusts and their angles have been studied, and the corresponding model outputs, which are the net forces and moments acting at CV, have been analysed. For example, in the first case, right thrusts are 12.5 N each and the left thrusts are 25 N each, while their corresponding angles are 30 deg and 0 deg . Thus the net force in X direction is 71.64 N while in Z direction it is -12.5 N . Also, roll moment is negative while pitch and yaw moments are positive.

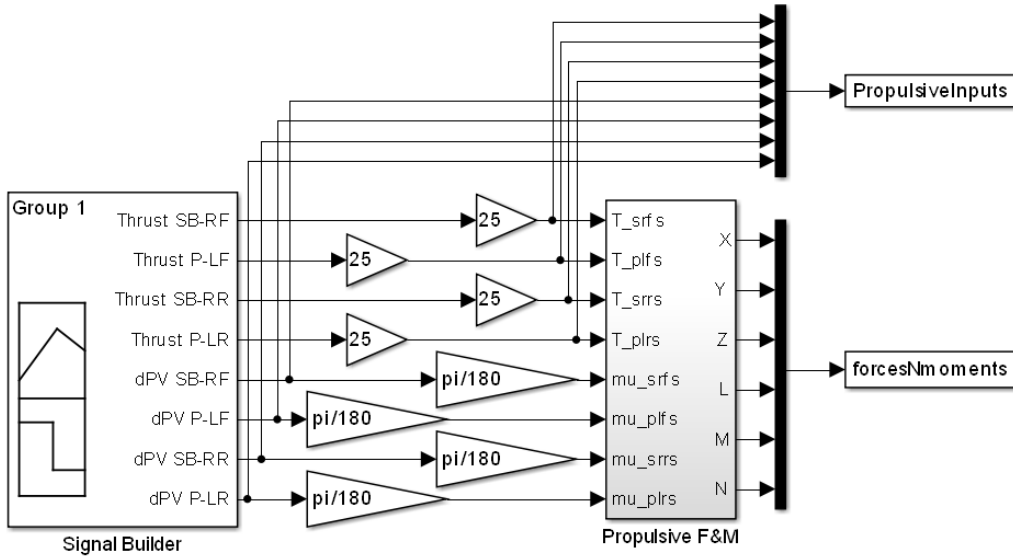


Figure 28: Validation of ‘Propulsive F&M’ model; SB – starboard side, P – port side, PV – pitch vectoring, RF – right front, LF – left front, RR – right rear, and LR – left rear.

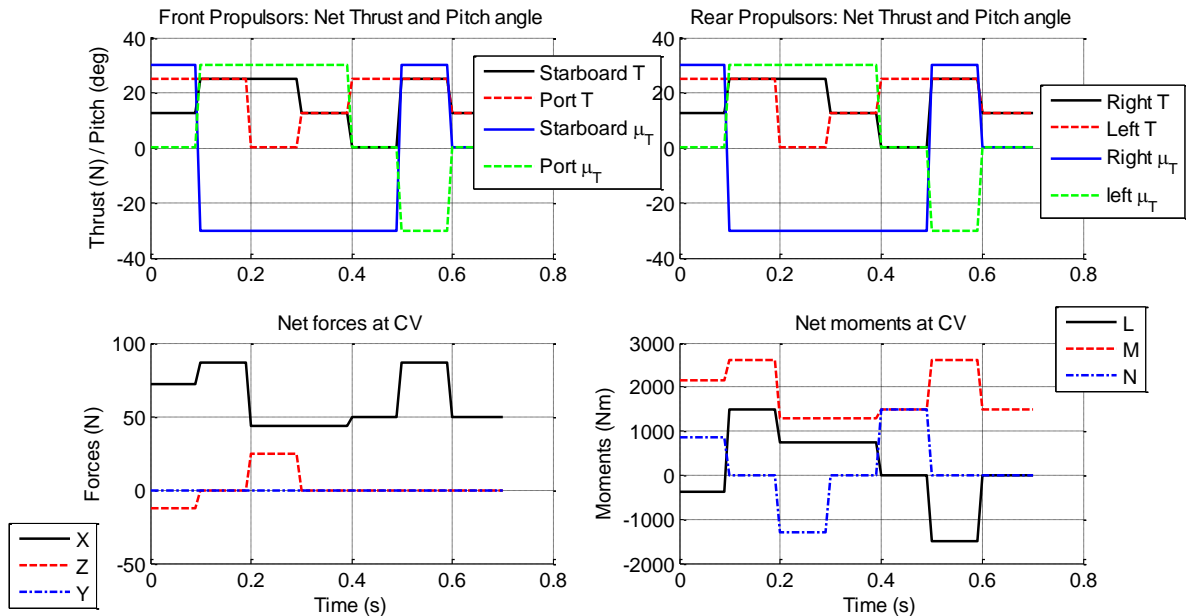


Figure 29: Validation results for ‘Propulsive F&M’ model

3.1.4. Forces and Moments: Coriolis and Centrifugal components

This subsystem calculates the forces and moments due to Coriolis and centrifugal effects. The Simulink block diagram of this ‘Coriolis and Centrifugal’ model is shown in Figure 30. As examples, the Simulink models for the ‘Axial force’ and ‘Rolling moment’ subsystems are shown in Figure 31 and Figure 32, respectively.

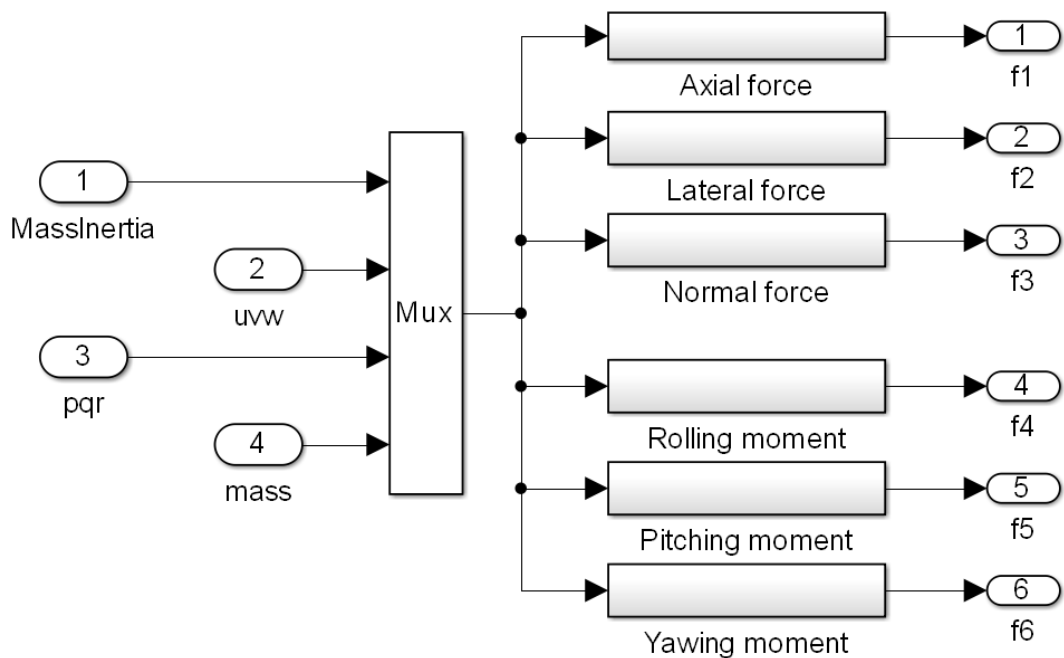


Figure 30: Simulink block diagram of ‘Coriolis and Centrifugal forces and moments’ model

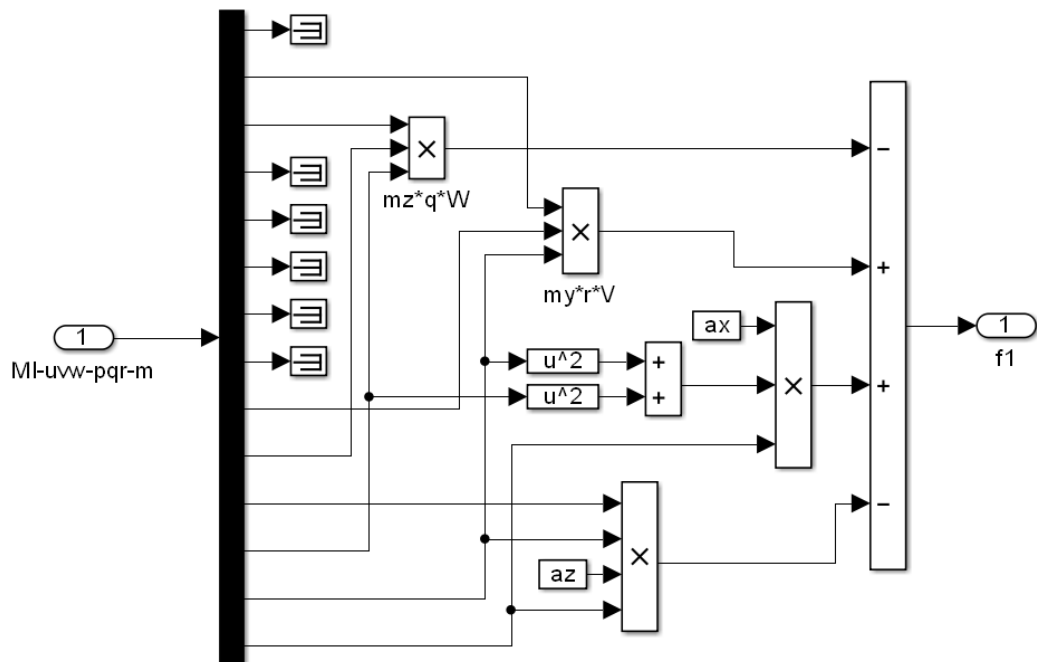


Figure 31: Axial Force subsystem (Coriolis and Centrifugal)

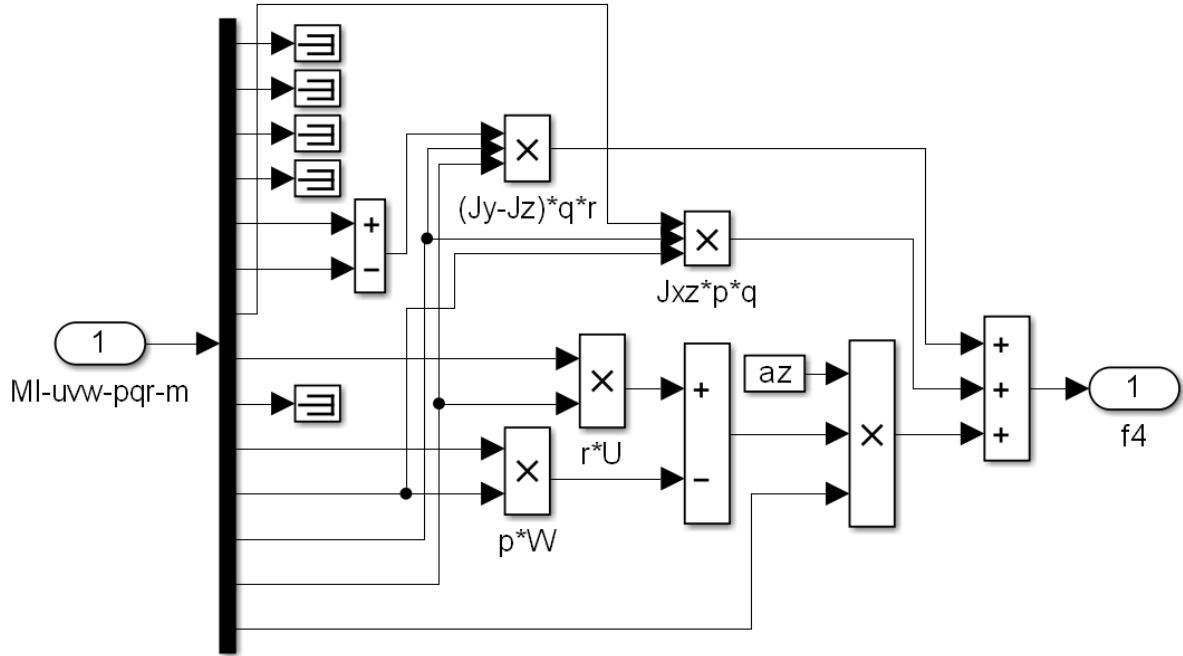


Figure 32: Rolling Moment subsystem (Coriolis and Centrifugal)

3.1.5. Inertia Coefficients

For a particular fineness ratio (a/b) of an axisymmetric airship hull, this model calculates the three inertia coefficients, i.e. k_1 (axial), k_2 (lateral), and k_3 (rotational). The setup used for validating the ‘Inertia Coefficients’ model is shown in Figure 33, and the corresponding validation results are given in Figure 34. The plot shown in Figure 34 is between fineness ratio and the three inertia coefficients for an ellipsoid moving in a fluid.

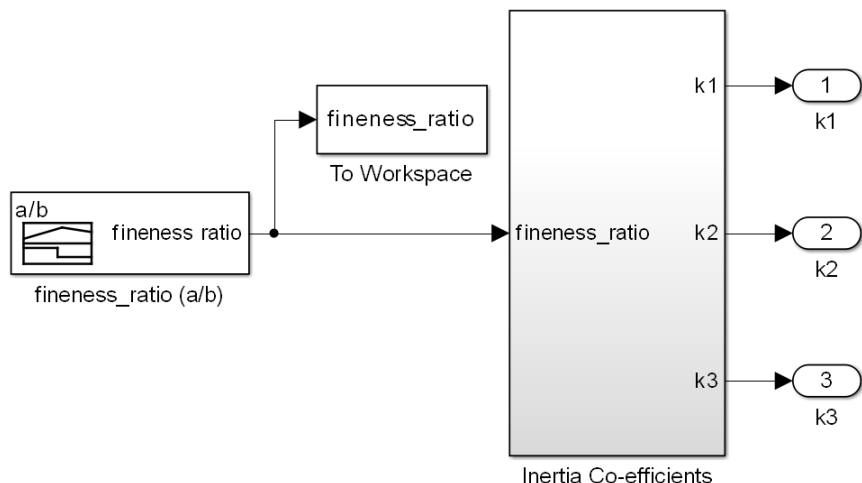


Figure 33: Validation of ‘Inertia Coefficients’ model

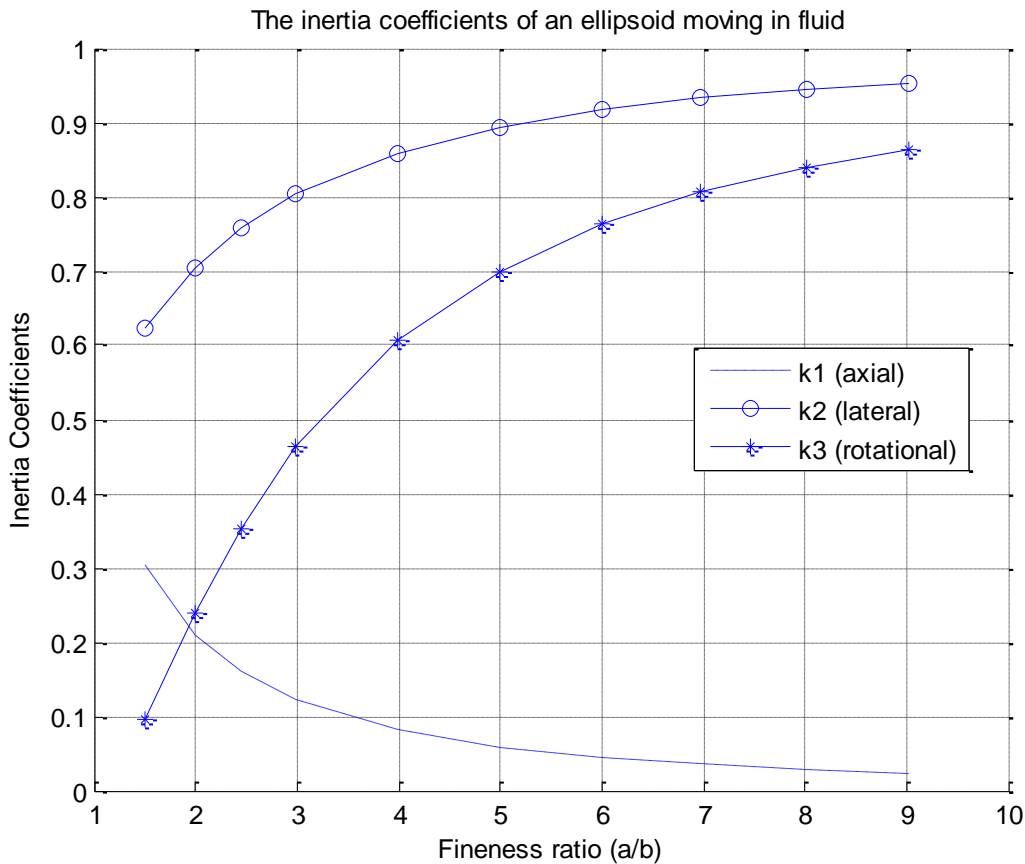


Figure 34: Validation results for ‘Inertia Coefficients’ model

The Simulink block diagram of ‘Inertia Coefficients’ model is also given below in Figure 35.

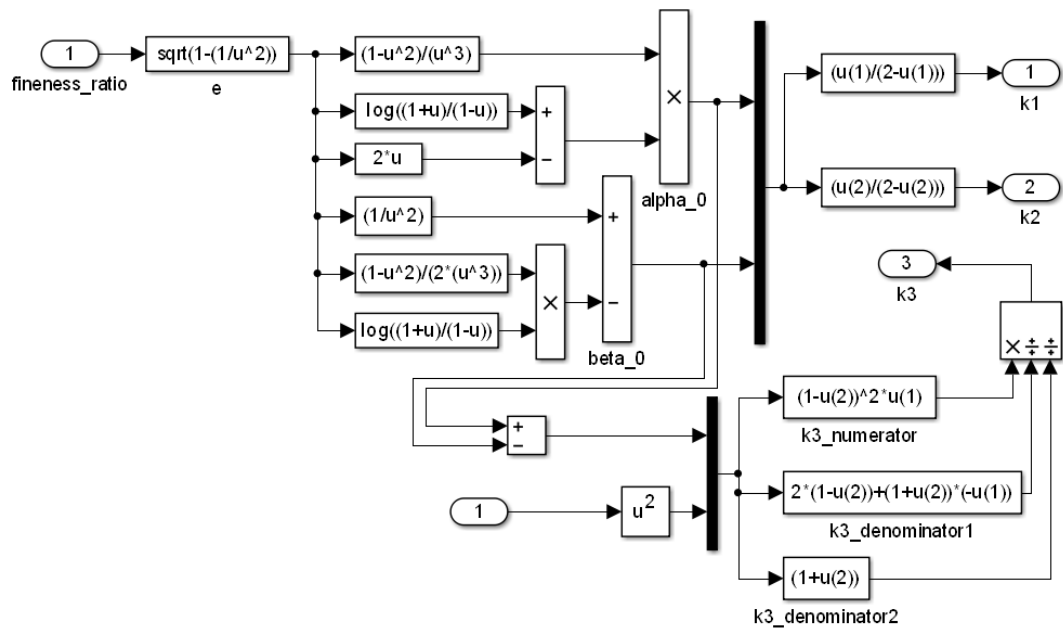


Figure 35: Inertia Coefficients model

3.1.6. Mass and Inertia

The outputs of this subsystem are the apparent masses (m_x , m_y , and m_z) along the three body axes of the airship, the apparent moments of inertia (J_x , J_y , and J_z) about these three axes, and the non-zero apparent product of inertia, i.e. J_{xz} . The ‘Mass and Inertia’ model, the setup used to validate it, and the corresponding validation results are given in Figure 36, Figure 37, and Figure 38, respectively.

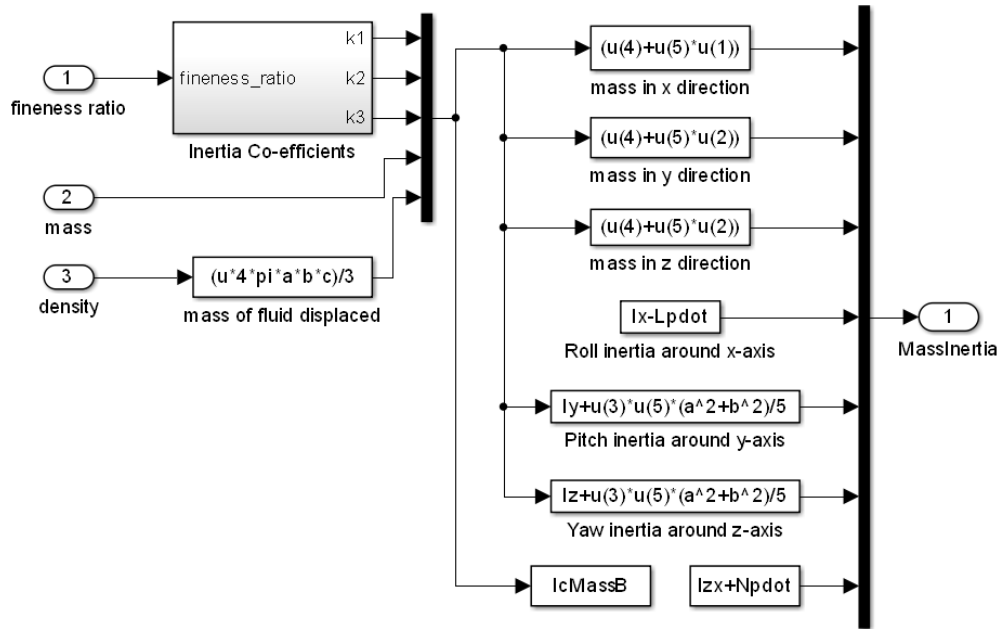


Figure 36: Mass and Inertia model

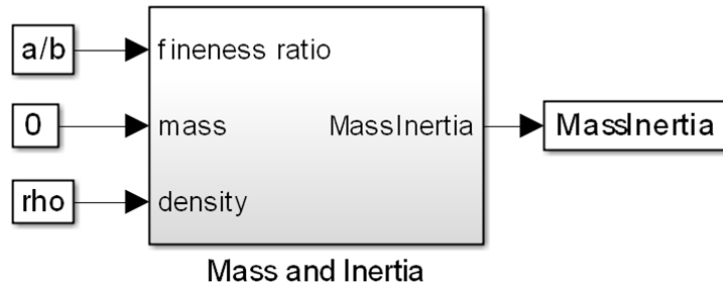


Figure 37: Validation of ‘Mass and Inertia’ model

Three airships: Generic ($a/b=3.75$), Lotte ($a/b=4$) & Akron ($a/b=5.91$)

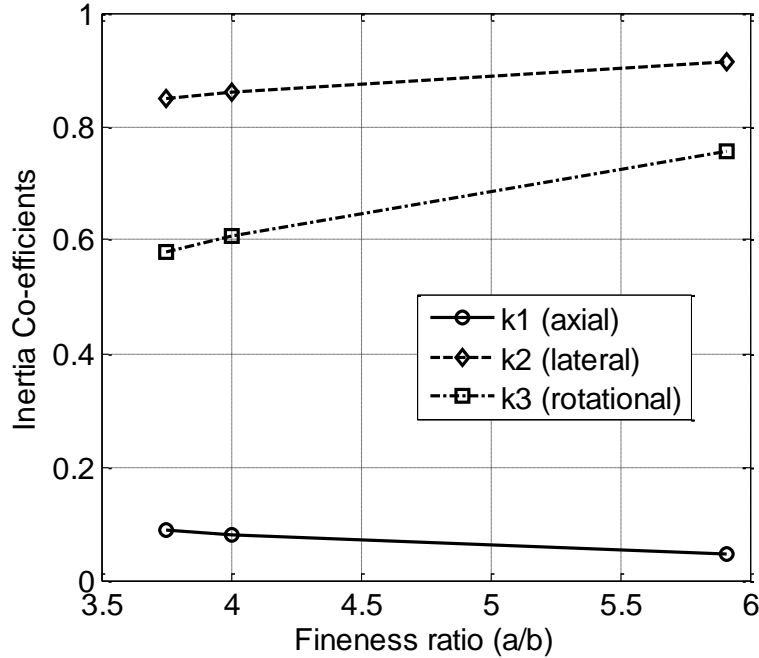


Figure 38: Validation results for ‘Mass and Inertia’ model

3.1.7. Mass and Inertia matrix

The Simulink model for the ‘Mass and Inertia matrix’ subsystem is given below in Figure 39. Note that the output of this subsystem is a matrix, the inverse of which has to be multiplied with the forces and moments vector to obtain the linear and angular accelerations.

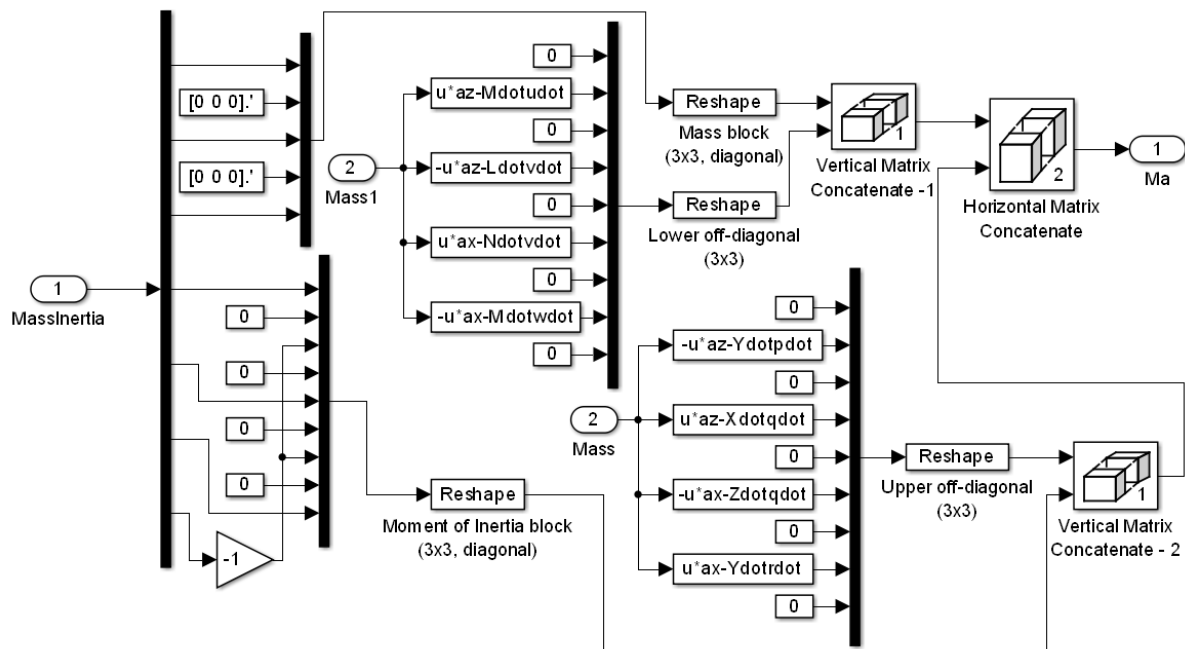


Figure 39: ‘Mass and Inertia matrix’ model

3.1.8. Equations of Motion

The ‘Equations of Motion (EoM)’ subsystem uses the above-mentioned ‘Mass and Inertia matrix’ model along with the forces and moments vector to determine the accelerations vector, and performs integration to obtain the linear and angular velocities as a function of time (Figure 40).

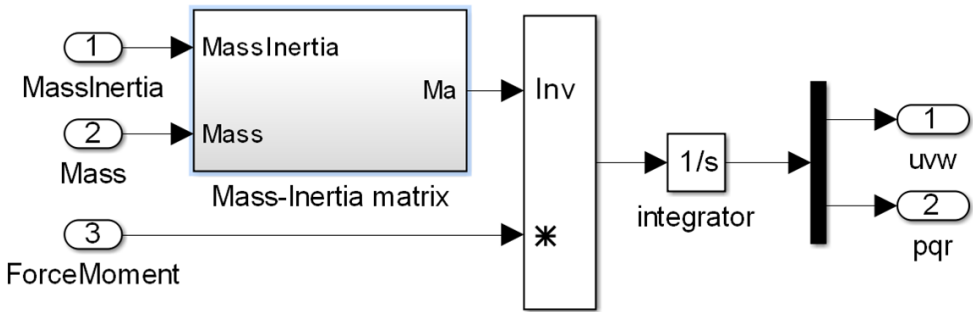


Figure 40: ‘Equations of Motion (EoM)’ subsystem

The setup used for validating the ‘EoM’ model and the corresponding validation results are shown in Figure 41 and Figure 42, respectively.

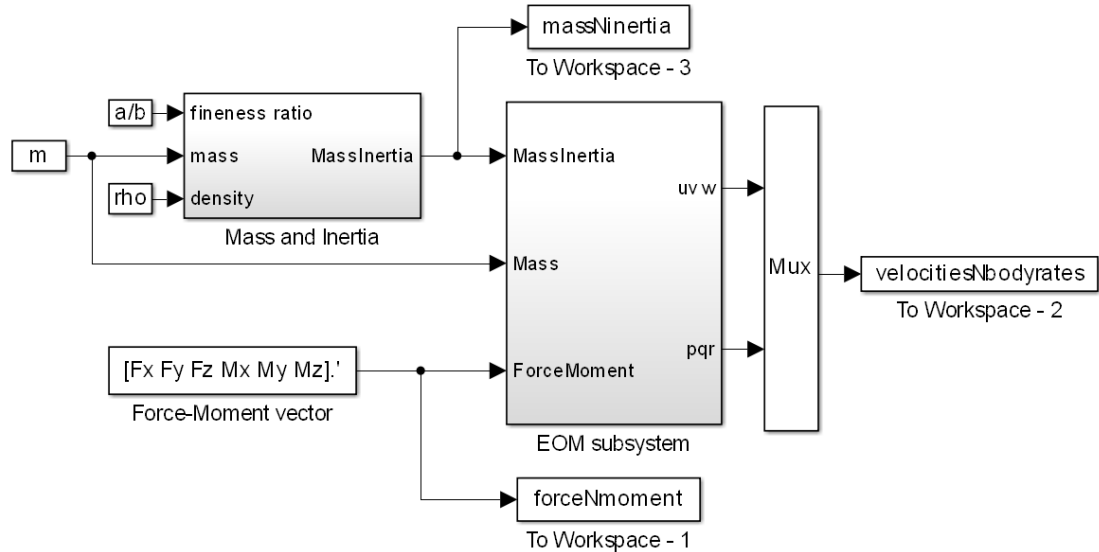


Figure 41: Validation of EoM model

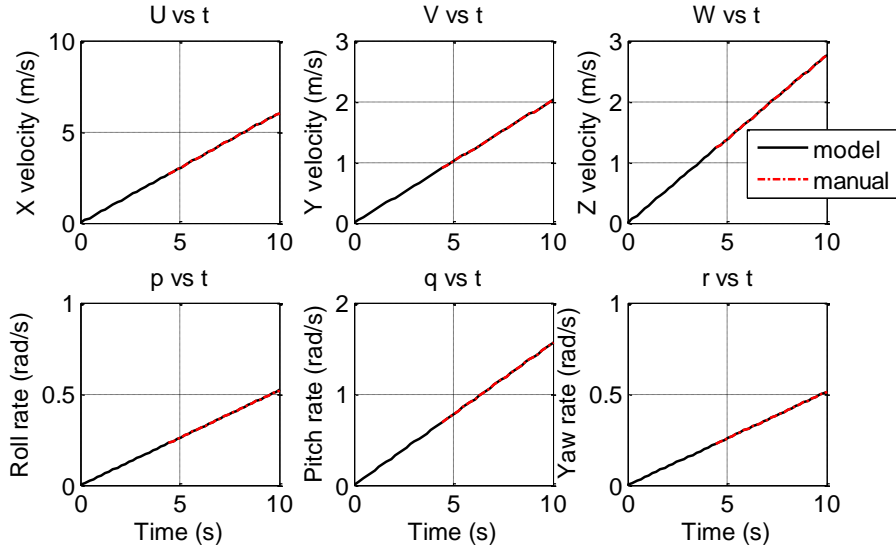


Figure 42: Validation results for EoM model

3.1.9. Quaternion kinematics and Angular transformations

The Simulink models discussed in this subsection and the next were obtained from ‘Aerosim’ toolbox and appropriately modified for the current application. The models used in this work for numerical integration of rotational kinematics in terms of Quaternions, for coordinate transformation from Quaternion to Euler, and for transformation from Quaternion to DCM are shown in Figure 43, Figure 44, and Figure 45, respectively.

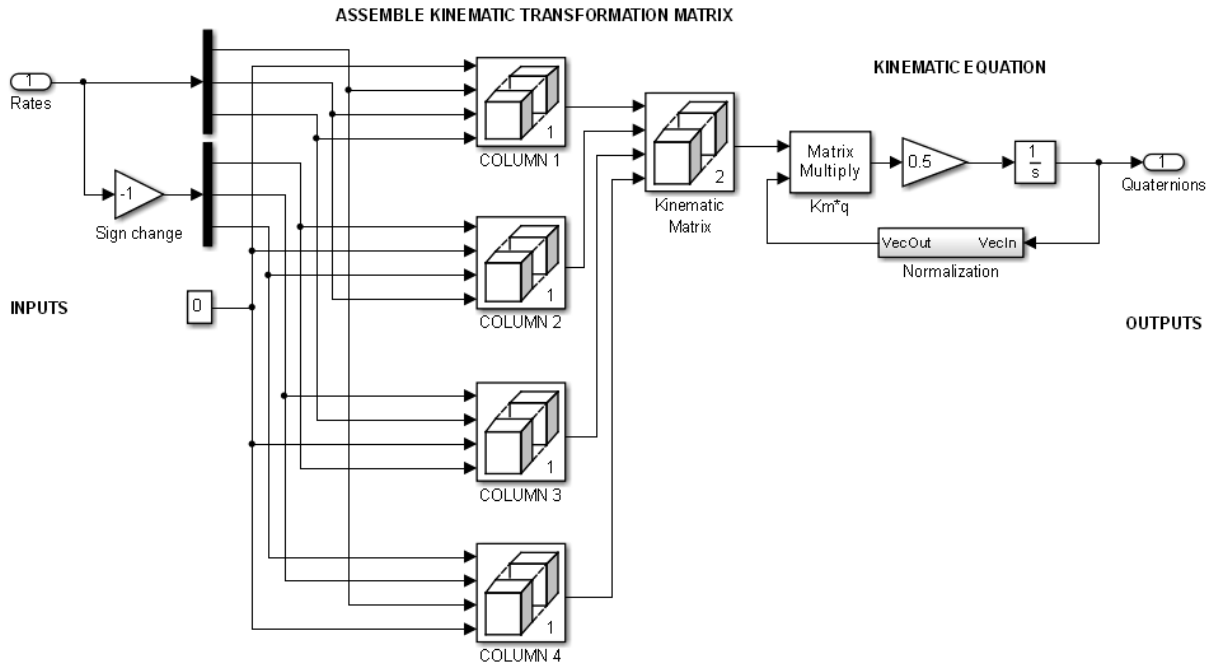


Figure 43: Simulink model for integration of rotational kinematics in terms of Quaternions

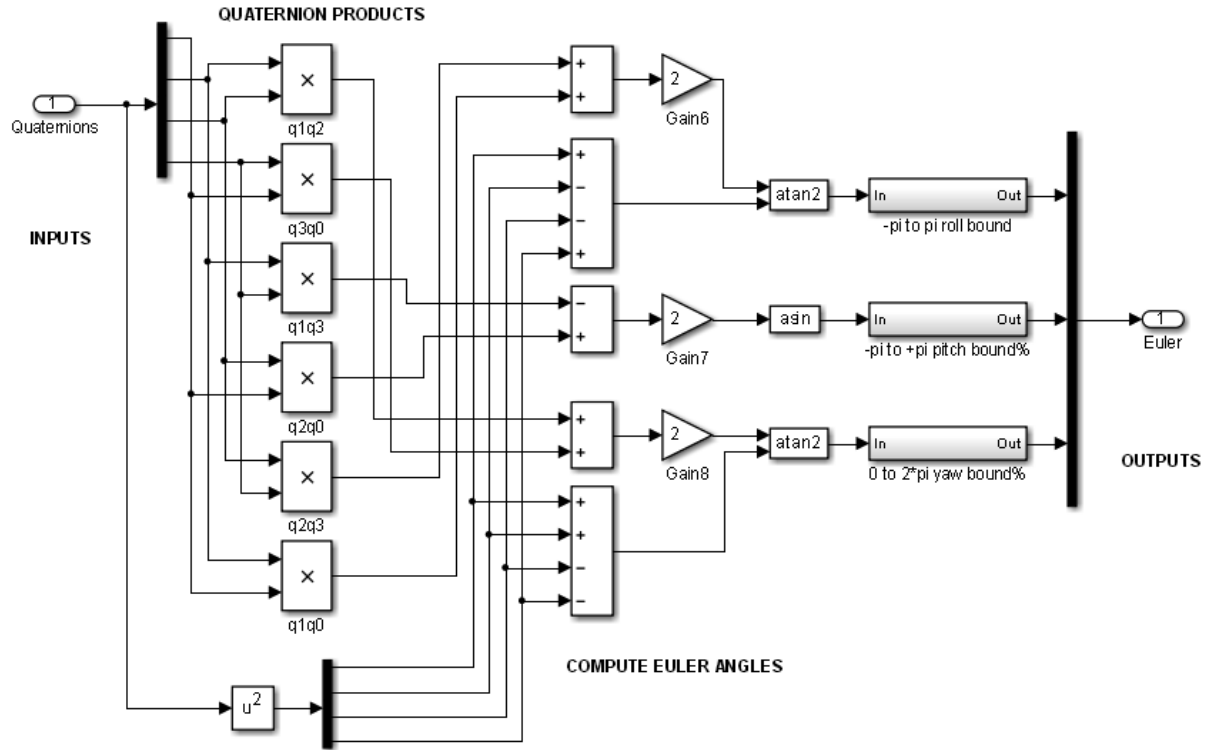


Figure 44: Simulink model for coordinate transformation from Quaternion to Euler angles

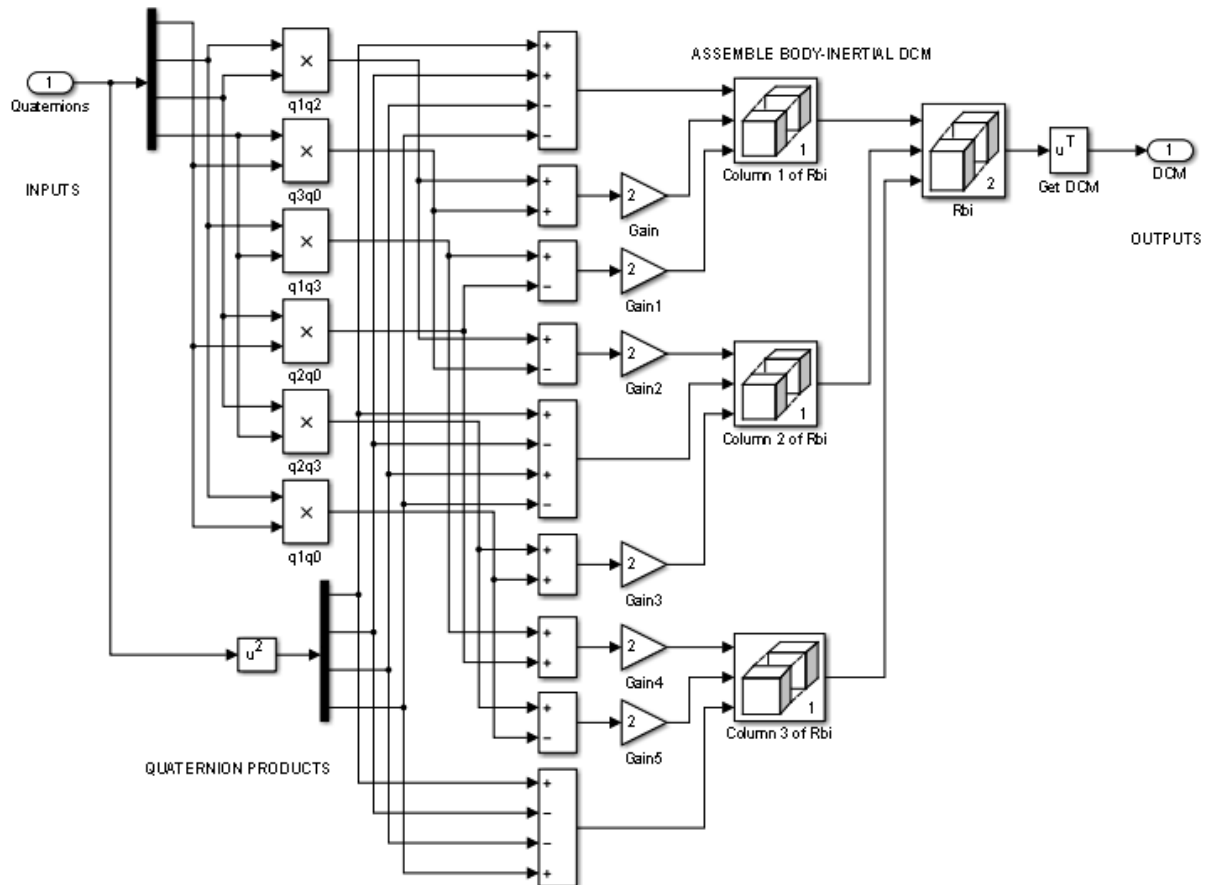


Figure 45: Simulink model for determining the Body to Inertial Direction Cosine Matrix (DCM) from the Quaternion angles

3.1.10. Earth model and Navigation

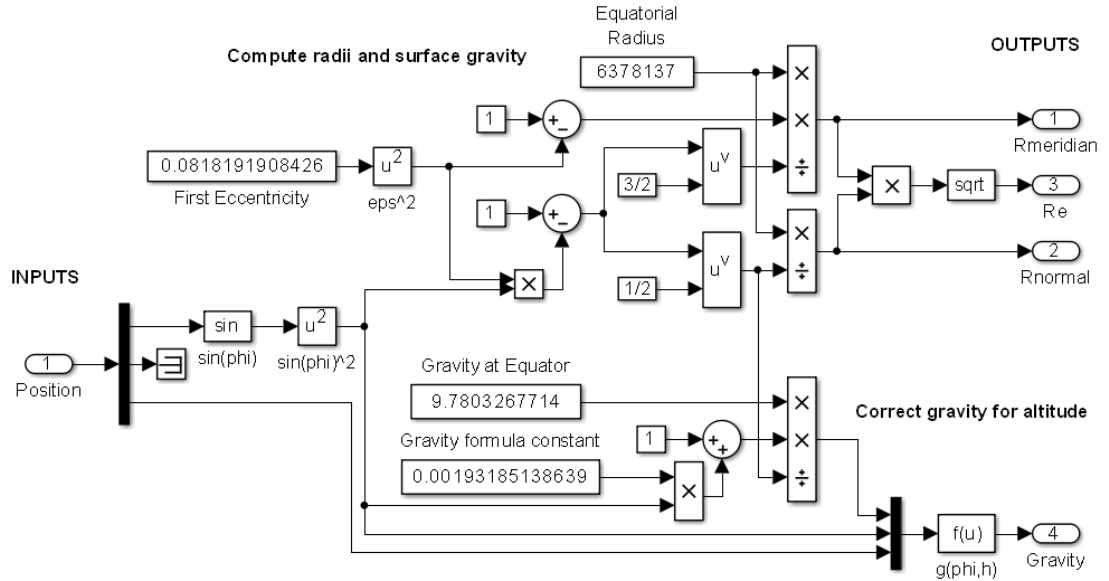


Figure 46: Earth model

The Simulink block diagram for the Earth model is shown in Figure 46, and the subsystem which implements the navigation equations is given in Figure 47. This navigation model is based on the Flat-Earth approximation. The ECI frame-based Geodetic navigation model has been discussed later in Section 4 as part of the airship system integration and analysis results.

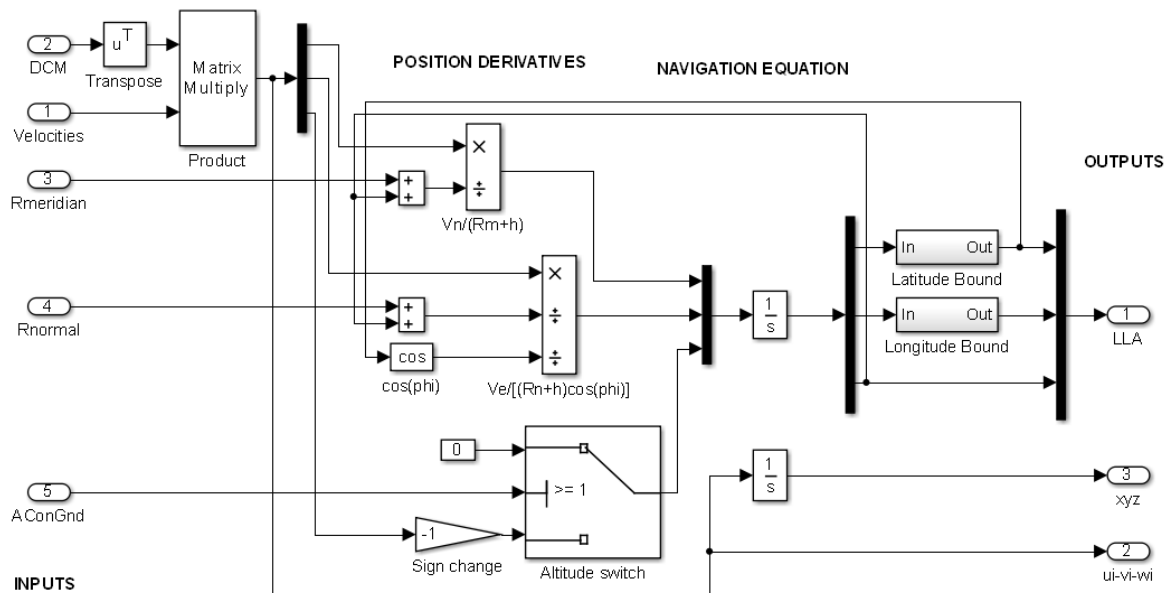


Figure 47: Simulink model for airship navigation

3.1.11. Velocity transformation: Body to Wind axes

The Simulink model used to determine the air-speed, angle of attack (α), and sideslip angle (β), from the body-frame components of the air-reference velocity vector, is shown in Figure 48 below.

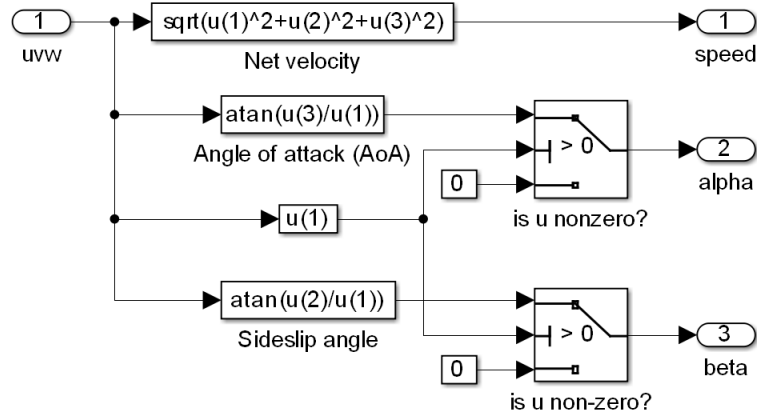


Figure 48: Air-reference velocity: body to wind axes

3.1.12. Atmosphere model

Atmospheric properties such as temperature, pressure and density are calculated using the model given in Figure 49. This model is based on the International Standard Atmosphere (ISA). Note that the altitude input is in ‘km’, and the altitude limit for this model is 32 km. Based on the altitude, various atmospheric properties are calculated using a set of equations corresponding to each atmospheric level.

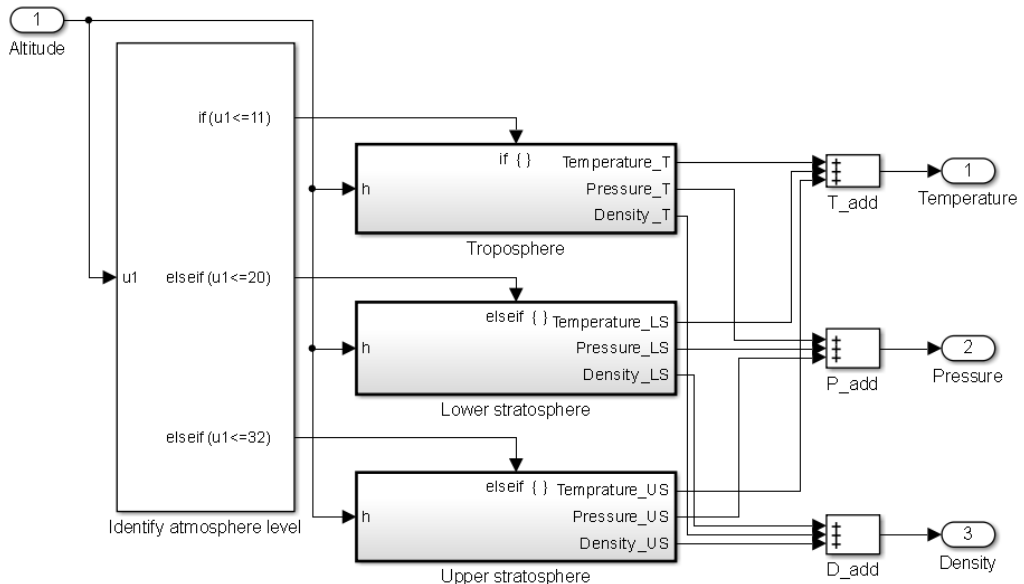


Figure 49: ISA-based atmosphere model

For example, the Simulink block diagram of the subsystem for ‘Upper Stratosphere’ is shown in Figure 50 below. For validation, the plots given in Figure 51 can be generated using this model.

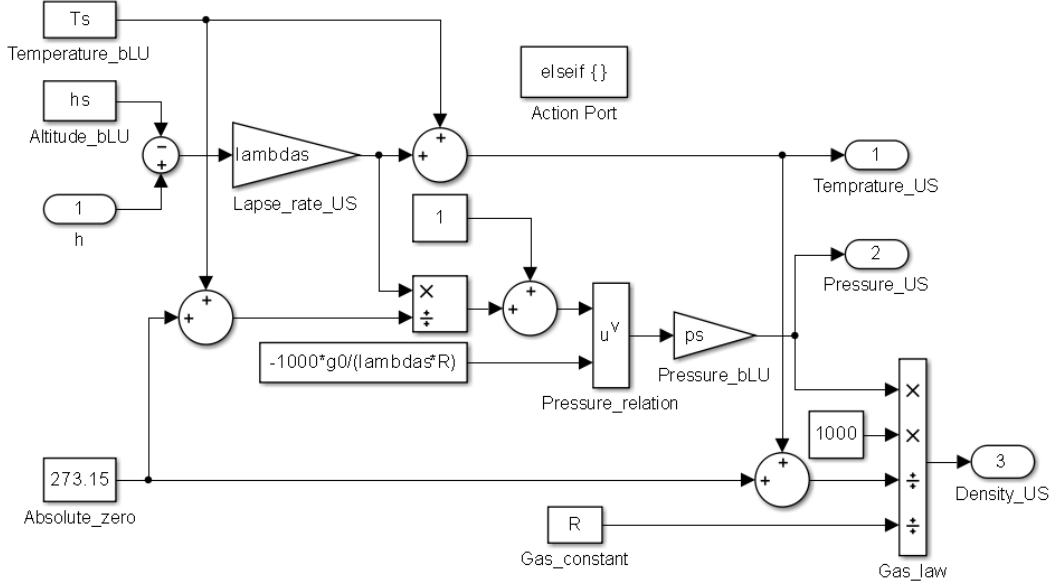


Figure 50: Simulink model of ‘Upper Stratosphere’ subsystem

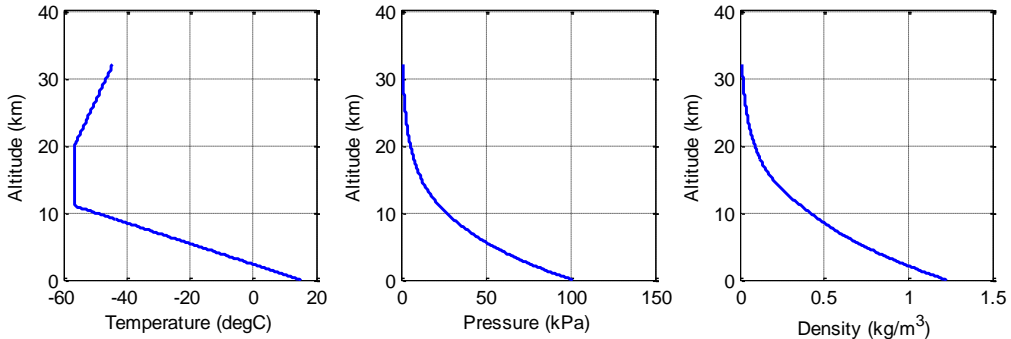


Figure 51: Validation results for ‘Atmosphere’ model

3.1.13. System Integration

Based on the block diagram given in Figure 18 and using all the subsystems discussed above in Section 3.1, the airship’s flight dynamics system (including navigation) is developed. The integrated system is shown in Figure 52, and Figure 53 captures the block diagram of its main subsystem, i.e. ‘Forces and Moments’. This flight dynamics model is based on the Flat-Earth approximation. The Geodetic flight dynamics model, which takes into consideration the Earth’s rotational speed and its ellipsoidal shape, is discussed later in Section 4.

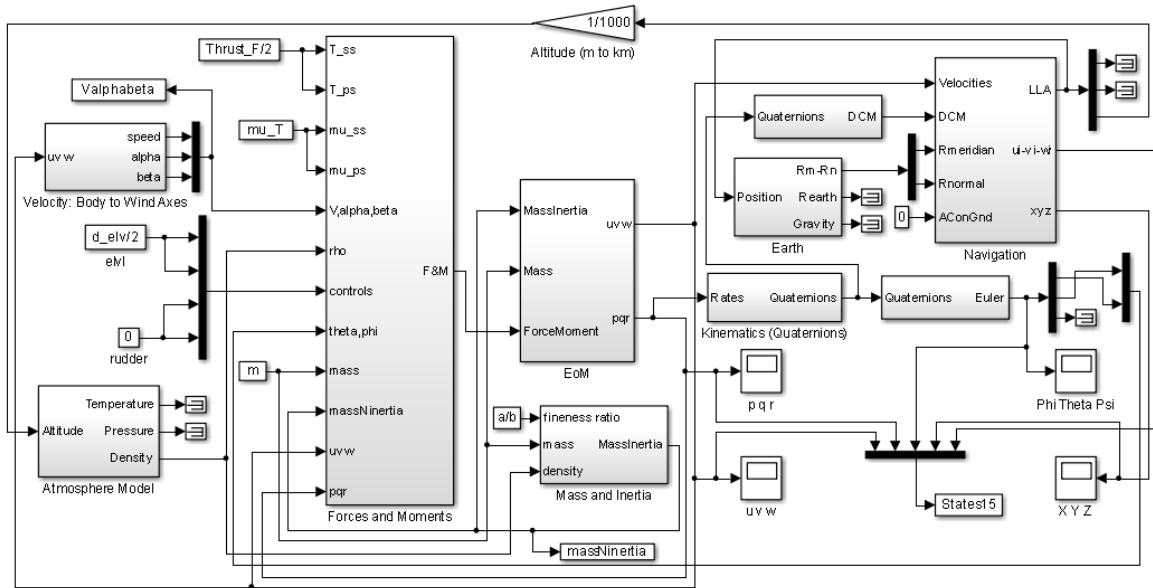


Figure 52: Integration of all subsystems to obtain the 6DOF flight dynamics model for a High Altitude Airship (HAA)

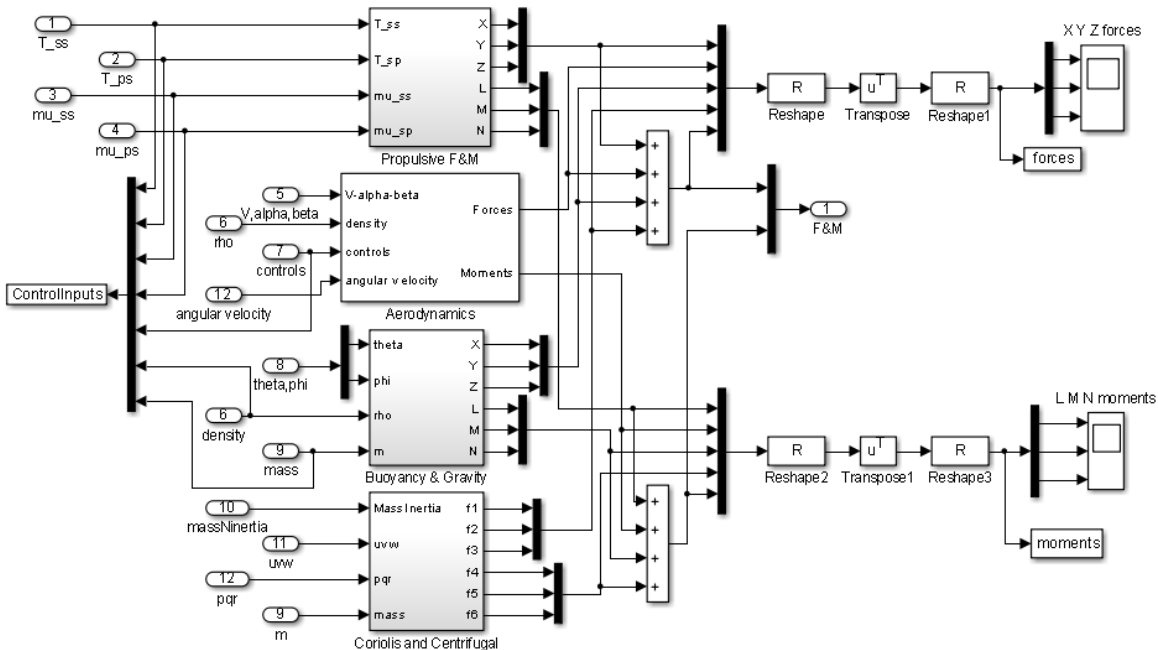


Figure 53: Simulink block diagram of the ‘Forces and Moments’ subsystem

Thus the flight dynamics part of HAA is modelled as above; it contains the forces and moments due to the aerodynamics, buoyancy, gravity, propulsion, centrifugal and Coriolis effects. The atmosphere model (ISA) has been incorporated to get the pressure, temperature and density at various altitudes. Earth and navigation models have been added to get the longitude, latitude, altitude and acceleration due to gravity.

3.2. Solar radiation and PV arrays

A high-level architecture of the power and propulsion system is shown in Figure 54. In this section, Simulink models pertaining to solar radiation and PV arrays are discussed. Model development for the remaining components, i.e. from Electrolyzer to Propeller, is described in the next section (3.3). The discussion on integration of power and propulsion systems will be taken up later in Section 4 as part of the full system integration.

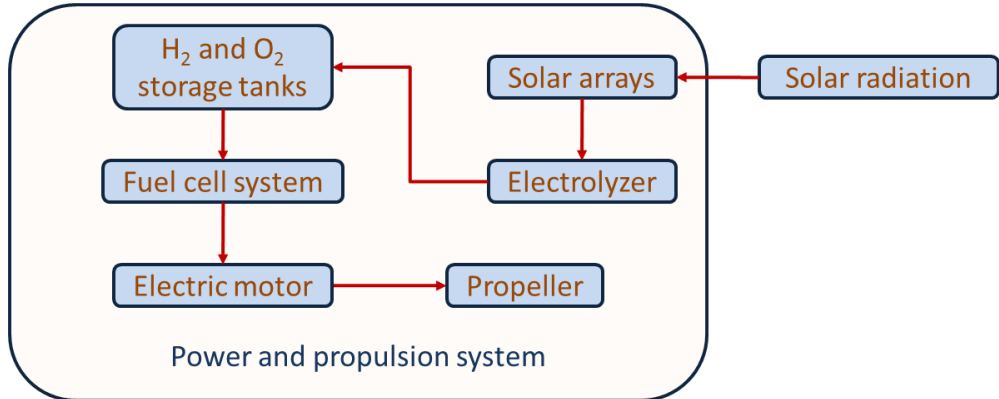


Figure 54: A schematic of the power and propulsion system

3.2.1. Declination angle of the sun

Given the day number, this subsystem determines the declination angle of the sun for that particular day with respect to the Equator. This model is applicable only to the latitudes north of Equator, i.e. for airship motion in the Northern Hemisphere.

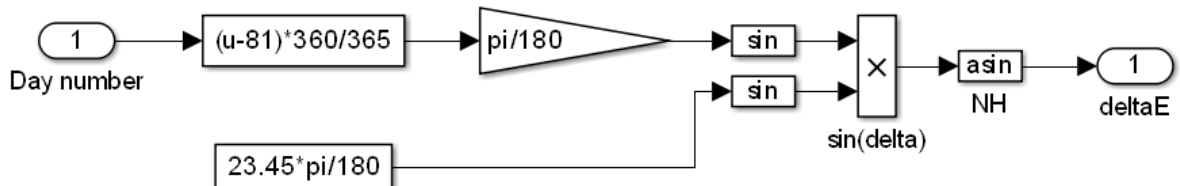


Figure 55: Simulink model to calculate the declination angle of the sun

3.2.2. Sunrise and Sunset timings

This model calculates the sunrise and sunset times for any particular day of the year at any particular place north of the Equator, i.e. for airship motion in the Northern Hemisphere. The inputs required are day number and latitude. It also resets the time to the 0-to-24 hour format as days go by, meanwhile counting the number of days the airship is in flight. The previous model “Declination angle of the Sun” (Section 3.2.1) is a subsystem of this Simulink model.

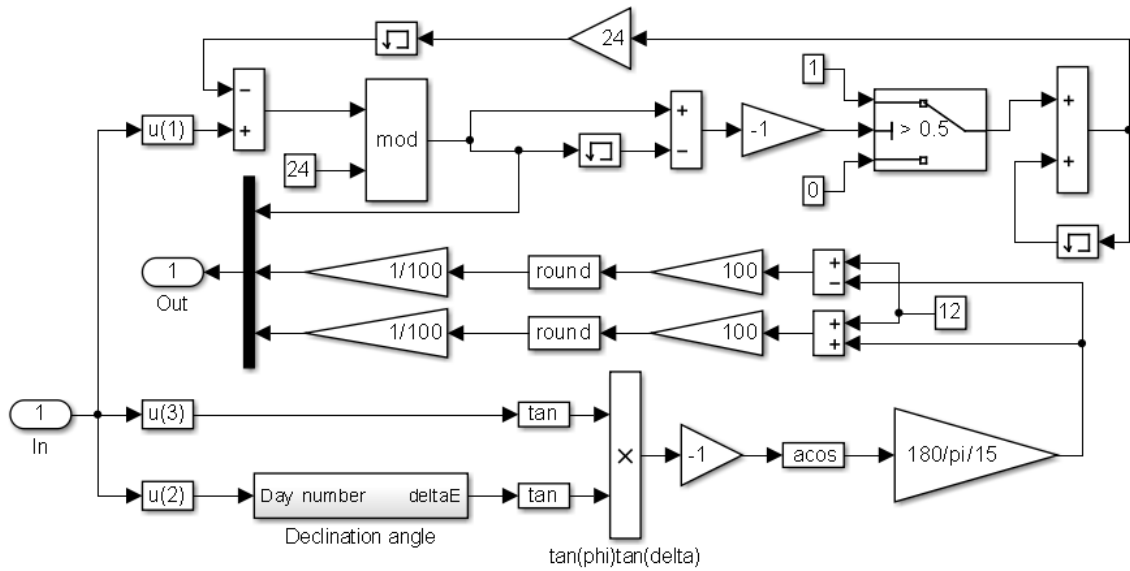


Figure 56: Simulink model to calculate the sunrise and sunset times

3.2.3. Solar Intensity

This model calculates the solar intensity reaching the Earth's orbital location on any day of the year using the day angle γ_E .

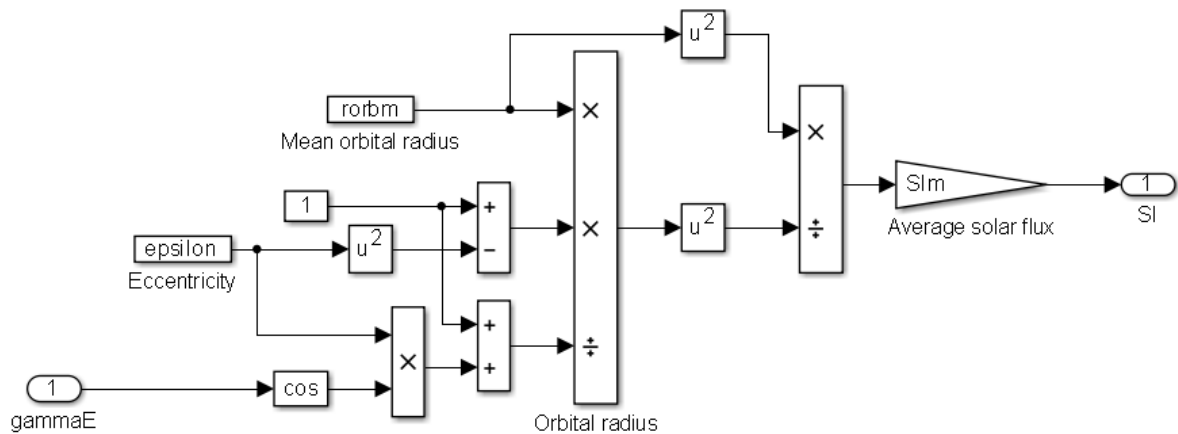


Figure 57: Simulink model to calculate the Solar Intensity

3.2.4. Variation with altitude

This model calculates the solar intensity at different altitudes in the Earth's atmosphere using the altitude and the solar intensity at the Earth's orbital location as inputs.

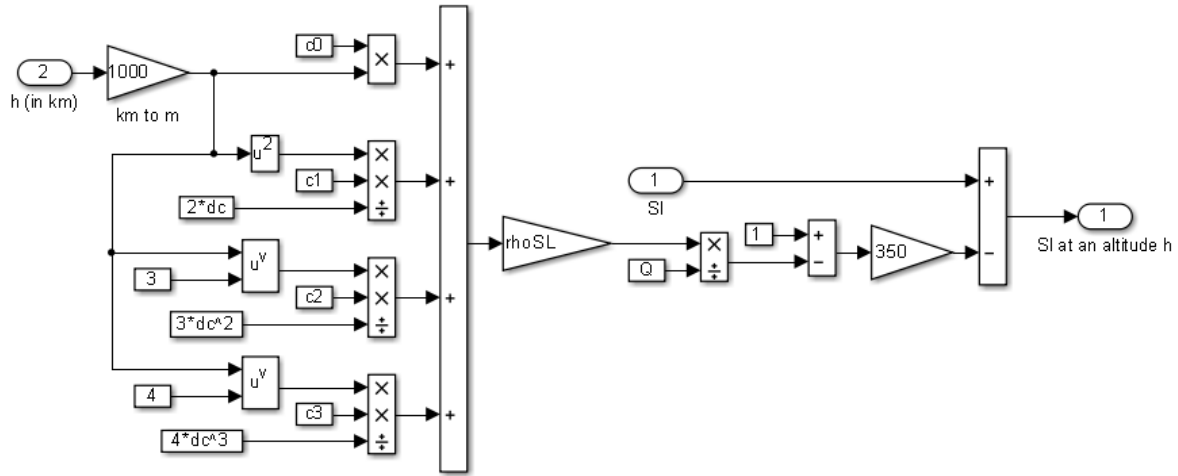


Figure 58: Simulink model implementing the altitude variation of solar intensity

3.2.5. Sun position

This model calculates the Sun's position with respect to the airship using the day number, time of the day, airship's latitudinal position and its orientation. The specific outputs of this model are solar elevation, solar azimuth and solar hour angles in addition to the sun vector in the East-North-Up frame and in the airship's body frame.

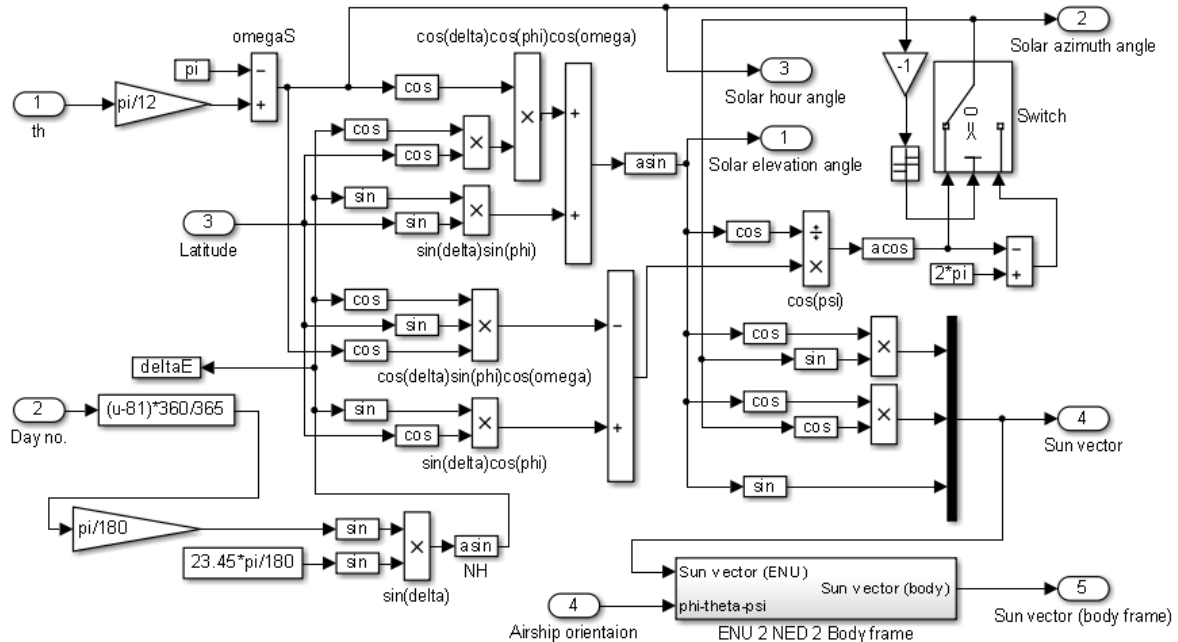


Figure 59: Simulink model to determine the Sun's position

3.2.6. Transformation: ENU-NED-Body frame

This subsystem is used to transform the Sun's position vector from the East-North-Up (ENU) frame to the airship's body frame using the airship orientation in terms of its Euler angles.

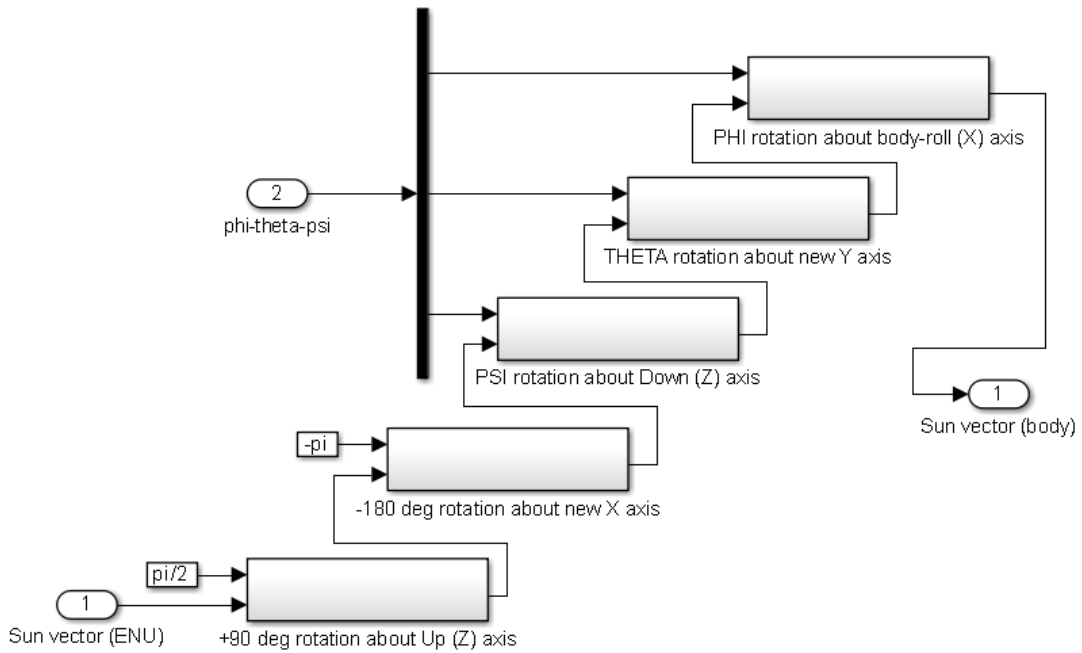


Figure 60: ENU to Body frame coordinate transformation

3.2.7. PV array calculations

This subsystem determines the total power generated by the photovoltaic (PV) array which is installed on the top surface of the airship. The inputs are solar elevation and azimuth angles, solar intensity and airship heading. The effects due to the airship's roll and pitch angle variation are ignored here. A shadow model is also included, and is described in the next subsection.

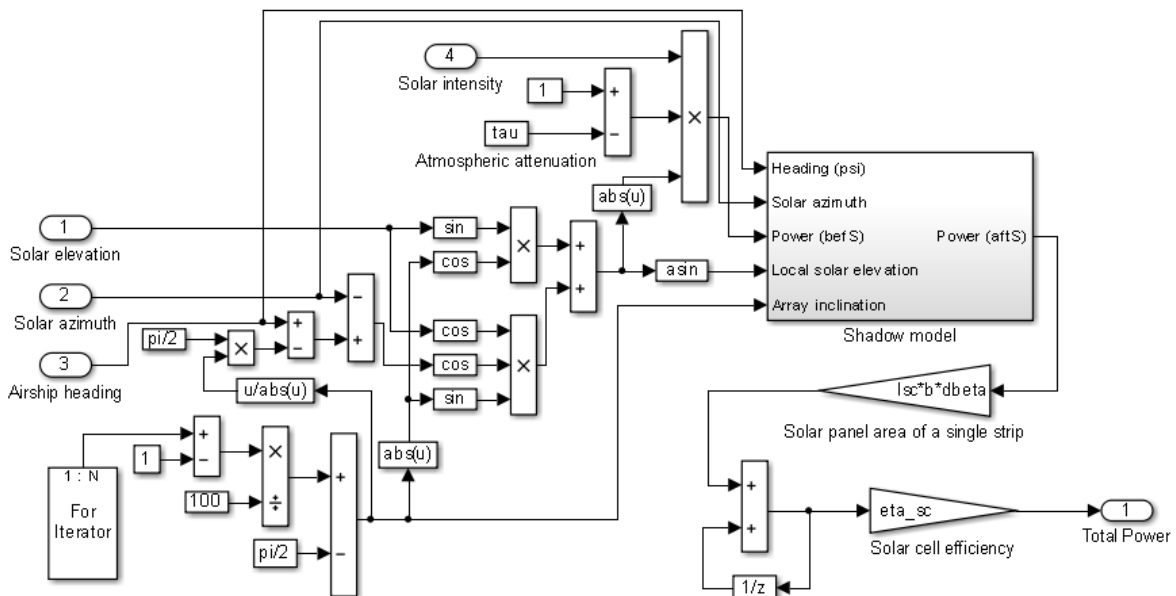


Figure 61: Subsystem to determine the total power generated by the PV array

3.2.8. Shadow model

This model determines whether a particular length-wise PV strip is in the shadow or not. The inputs, local solar elevation and array inclination angles, are parameters of the PV strip.

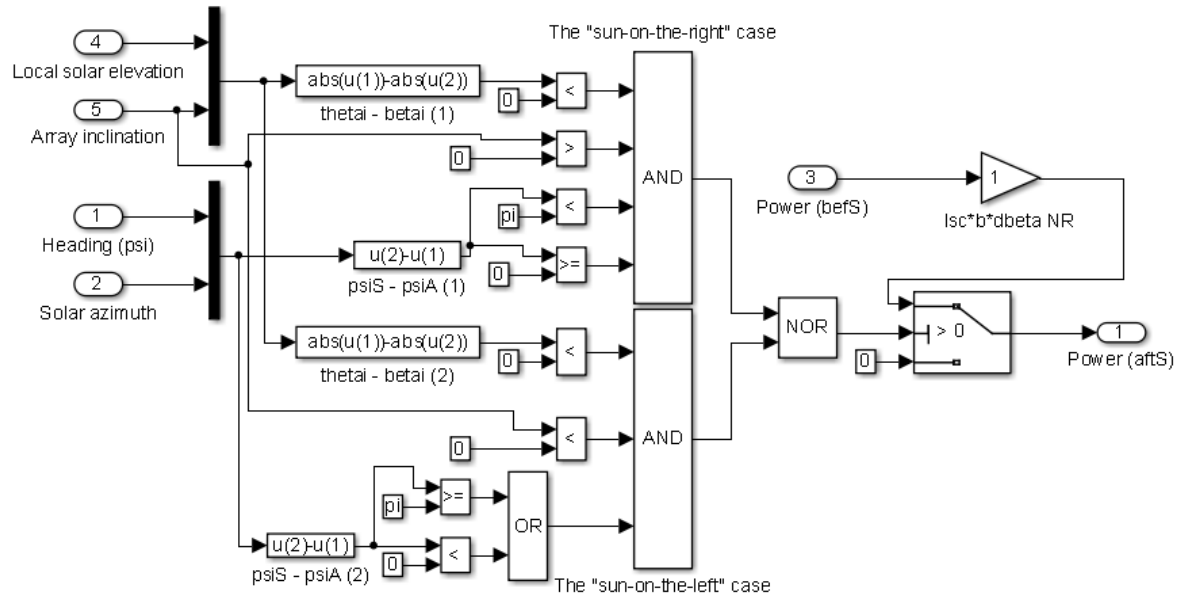


Figure 62: Shadow model

3.2.9. System Integration

The various models in this section are combined here to build the power system (Figure 63 and Figure 64). The day-night identification is done by the system shown in Figure 63. The actual power generating components are contained in the subsystem “Day time” (Figure 64).

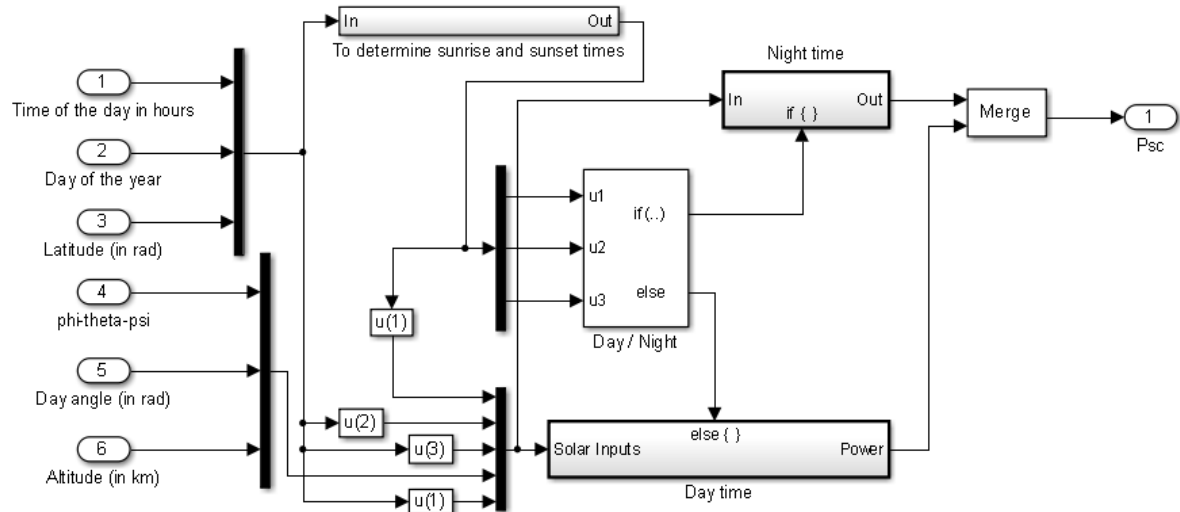


Figure 63: Power system

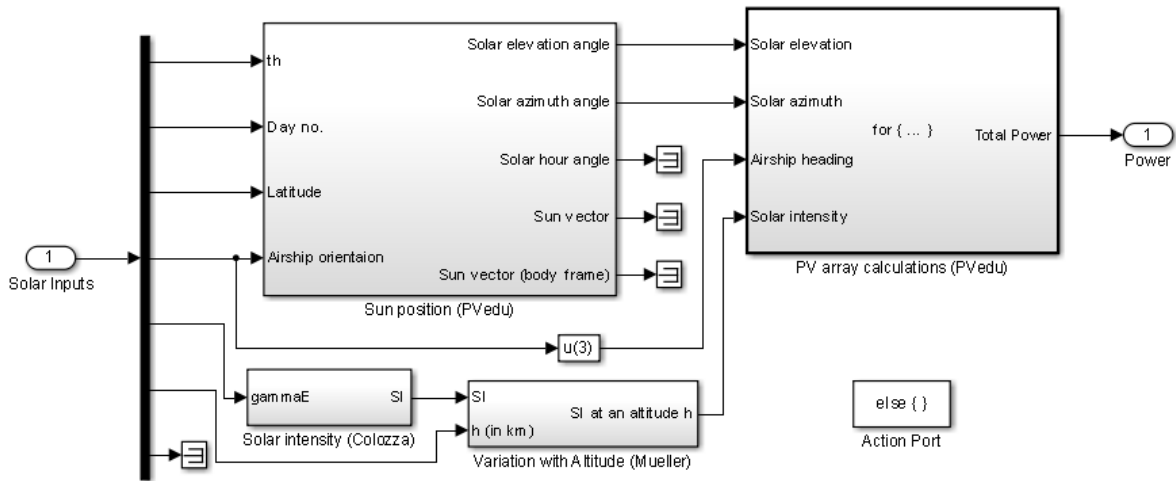


Figure 64: The subsystem “Day time”

3.3. Propulsion (including Storage)

In this section, Simulink models pertaining to the propulsion system are discussed (Figure 54). The propulsion system designed for the current airship system simulation has four propulsors. Power produced from the PV array system is equally distributed among them. The Simulink model of a single propulsor is shown in Figure 65.

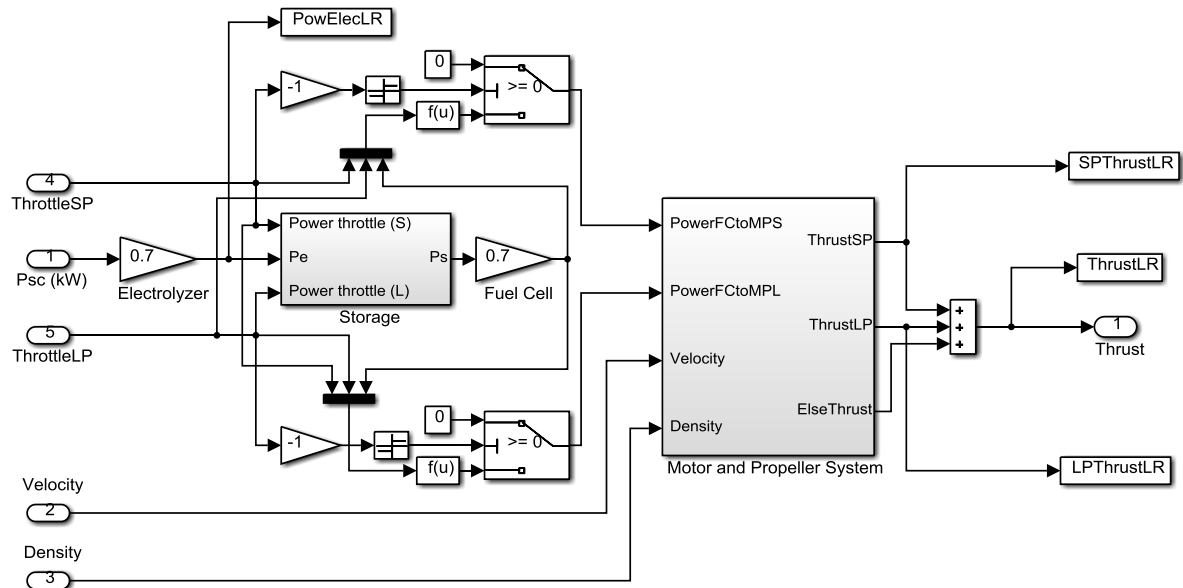


Figure 65: Simulink model of a single propulsor

Each propulsor consists of an electrolyzer, a storage system, a fuel cell and two motor-propeller units, one with the smaller propeller and the other with the larger propeller. The propulsors are

attached on two sides (port and starboard) of the airship, two forward of the C.G. and the other two rearward of the C.G. The above model corresponds to the Left-Rear propulsor, denoted by “LR”. “SP” stands for smaller propeller and “LP” stands for larger propeller.

3.3.1. Electrolyzer, Storage and Fuel cell

The electrolyzer is simply modelled as a black-box system with 70% total efficiency, i.e. 70% of the input power P_{sc} from the PV array is passed on as usable output power P_e (Figure 65). Addition and depletion of energy in the storage system is based on simple integrators (Figure 66). It is assumed that the storage system has no losses. The output of the storage system, P_s is the power drawn by the motor-propeller unit, either the smaller or larger propeller. For each propeller, the power required to run the motor-propeller unit is normalized with respect to a specific maximum power to define the power throttle.

For example, for the larger propeller, power required is normalized with maxPsreqLP to define the throttle input. The variable maxPsreqLP is the power required out of the storage system to drive the larger propeller at maximum possible efficiency such that it produces the required thrust for the airship to fly at the design maximum speed of 45 m/s. Similarly, maxPsreqSP is the power required to drive the smaller propeller for it to produce the required thrust for airship flight at design mean speed of 20 m/s.

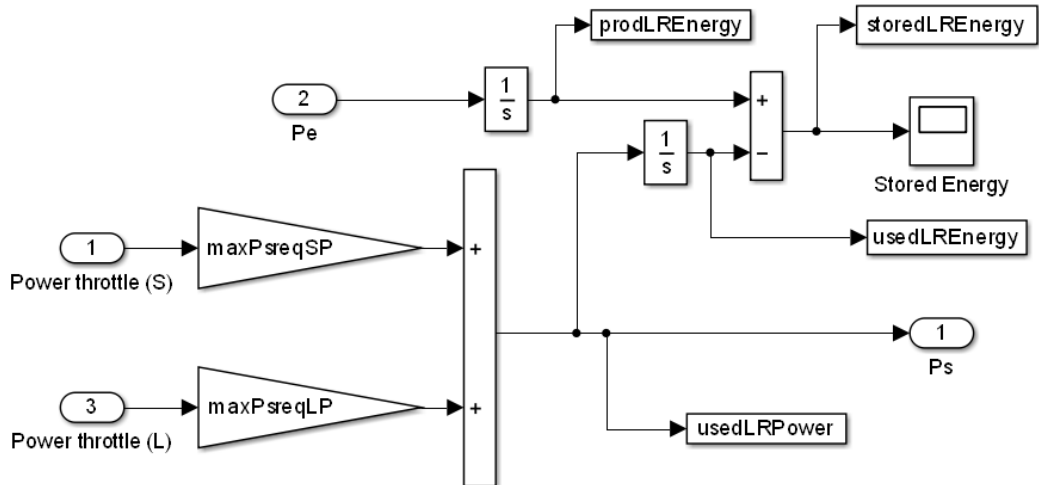


Figure 66: Storage system for Left-Rear propulsor

Again the fuel cell is simply modelled as a black-box system with 70% total efficiency, i.e. 70% of the input power P_s from the storage system is passed on as usable output power P_f (Figure 65).

3.3.2. Motor and Propeller System

From here onwards and in the next subsections, the contents of the “Motor and Propeller System” are discussed. Here, only one of the units, smaller or larger, can be run at a time. The

smaller propeller is designed for typical lower speeds from 0 to 30 m/s, and the larger propeller for higher speeds from 30 to 55 m/s.

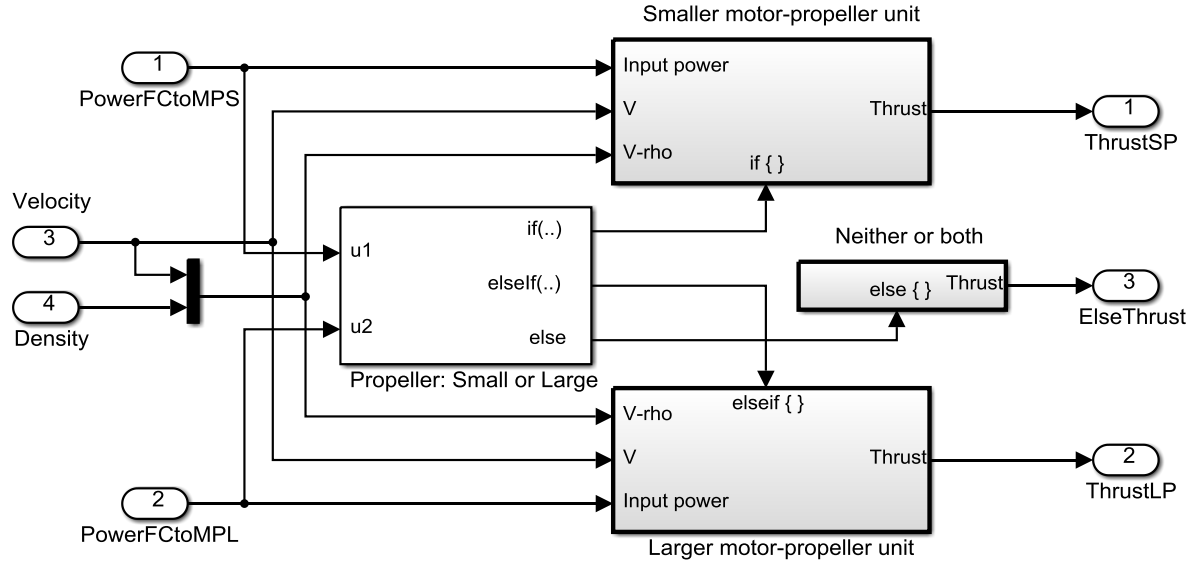


Figure 67: Simulink model of motor and propeller system

3.3.3. Smaller / Larger motor-propeller unit

The larger motor-propeller unit contains three subsystems – one modelling the electrical component of the motor dynamics, another implementing the logic for choosing the propeller's operating conditions, and the last one modelling the mechanical component of the motor dynamics combined with the propeller dynamics (Figure 68). The smaller unit has the same system architecture as the larger one.

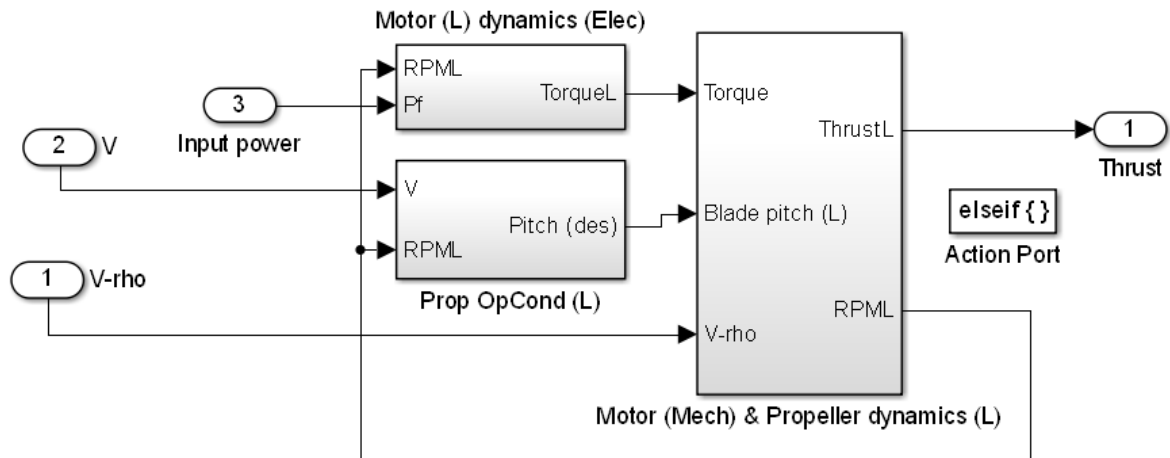


Figure 68: Larger motor-propeller unit

3.3.4. Propeller operating conditions

This subsystem (Figure 69) decides the pitch angle of the propeller blade based on the forward speed (V) of the airship and the angular speed (RPM) of the propeller such that maximum possible propeller efficiency is maintained. For zero RPM or zero forward speed, the pitch angle is set to zero. Non-zero pitch angles are commanded as a function of the advance ratio (J) only when the propeller develops rotation speeds ≥ 1 and the airship develops non-zero forward speeds (Figure 69 and Figure 70).

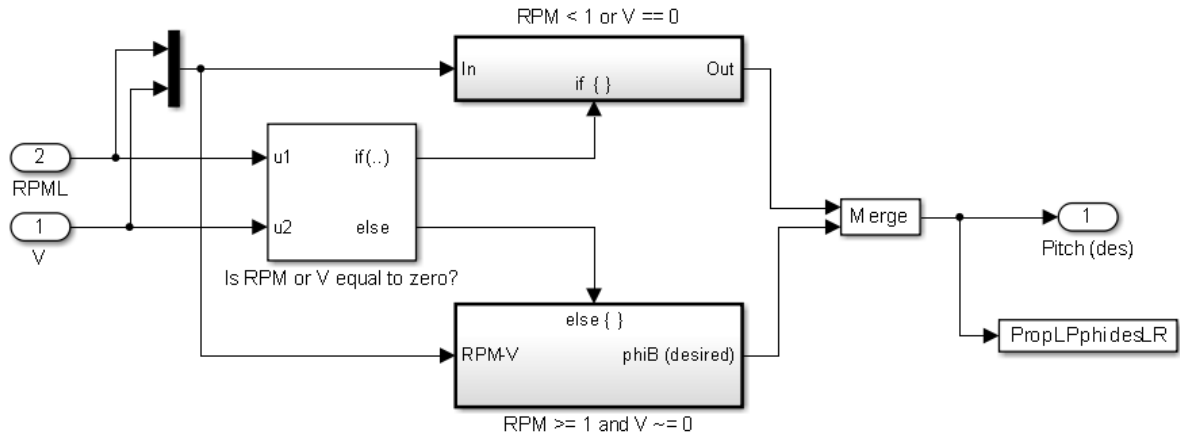


Figure 69: Propeller operating conditions (L) subsystem

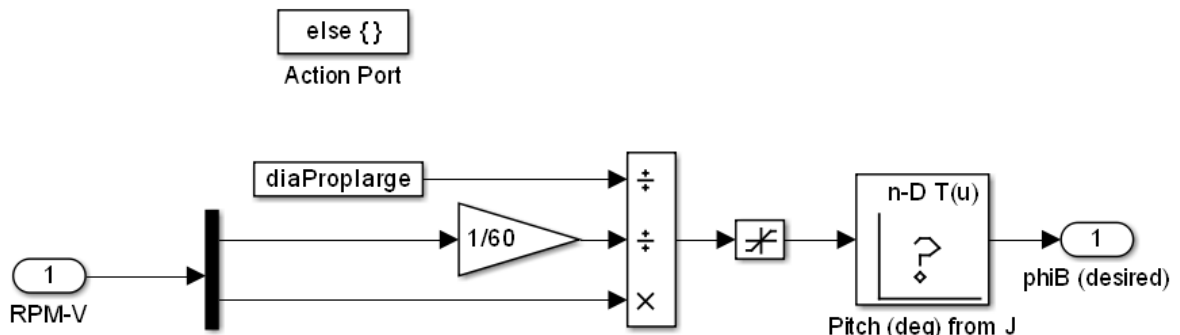


Figure 70: The subsystem corresponding to $RPM \geq 1$ and $V \neq 0$

3.3.5. Motor dynamics (Electrical)

This subsystem models the electrical component of the motor dynamics which is essentially a first-order differential equation as defined in Section 2.11. Primary input is the power drawn from the fuel cell, P_f , and the output is the motor torque. Additional feedback input is the rotational speed of the propeller, RPM (Figure 71).

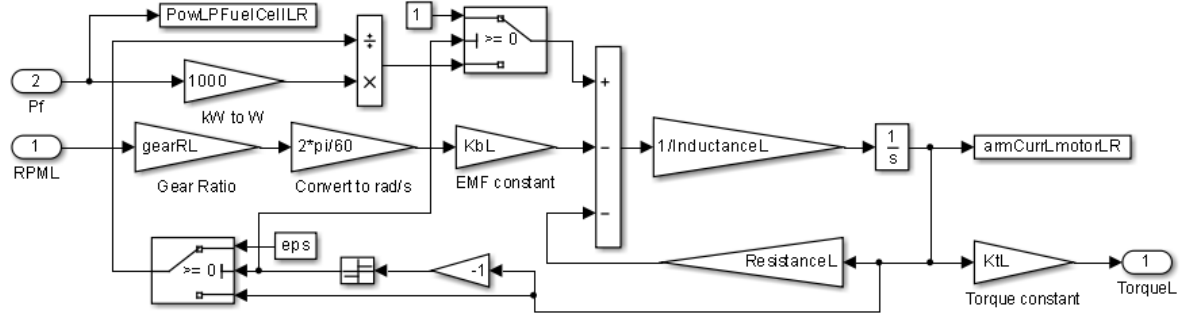


Figure 71: Motor (Electrical) dynamics subsystem

3.3.6. Motor (Mechanical) and Propeller dynamics

The subsystem shown in Figure 72 models the mechanical part of the motor dynamics and the propeller dynamics. The rotational inertia of the motor and the propeller (including shaft) are clubbed together into the parameter $J_{propmotorL}$, and the viscous damping of the two components is captured by the parameter $b_{propmotorL}$. Thus the motor torque to propeller RPM conversion of the motor-propeller unit is modelled as a second-order mass-damper system as defined in Section 2.11. The power conversion and thrust production of the propeller itself is simply modelled in terms of its characteristics as defined in Equation 45. The details of the propeller blade dynamics and the propeller characteristics are described in the next two subsections.

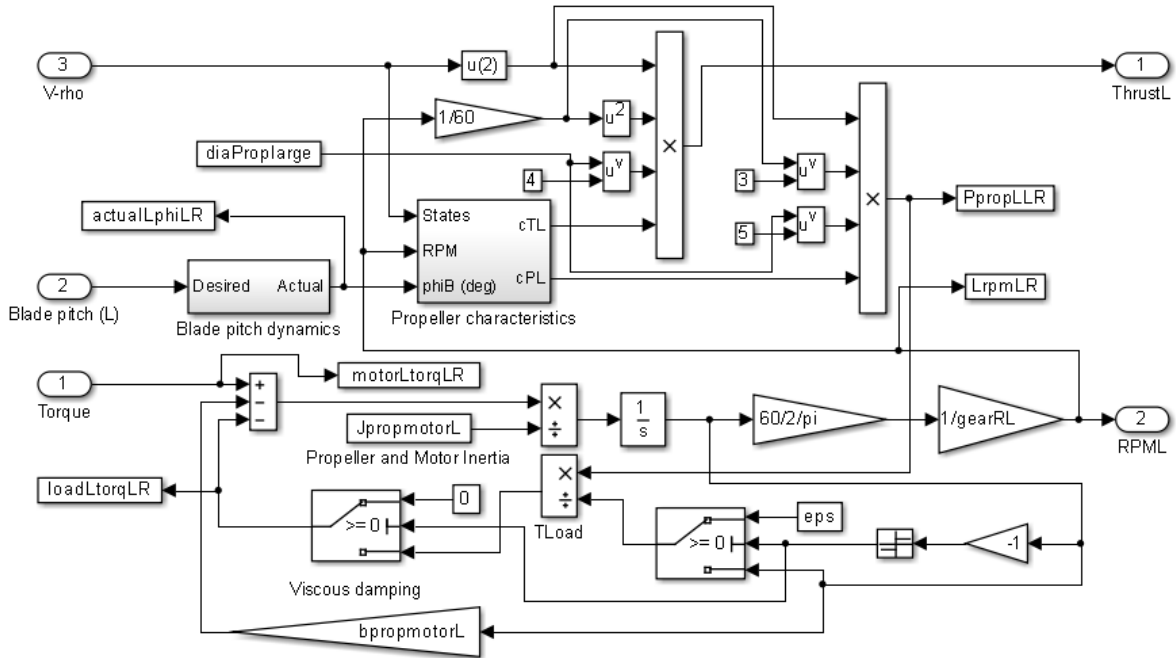


Figure 72: Motor (Mechanical) and Propeller dynamics subsystem

3.3.7. Blade-Pitch dynamics

The pitch angle variation of the propeller blade is modelled as a first order system with a time constant τ_{LPphi} (Figure 73). The propeller-blade pitch angle varies from 0 to 32 deg.

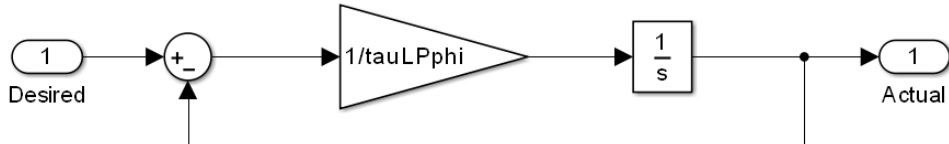


Figure 73: Propeller blade dynamics subsystem

3.3.8. Propeller characteristics

The system shown in Figure 74 calculates, using table lookups, the thrust and power coefficients as a function of the blade pitch angle and the advance ratio. As defined in Section 2.12, the propeller's advance ratio is a function of its diameter, its rotational RPM and the forward speed of the airship. The table lookups have been calculated and prepared offline such that for any input pair (J, ϕ_B) it gives the thrust and power coefficients corresponding to the propeller operating at maximum possible efficiency.

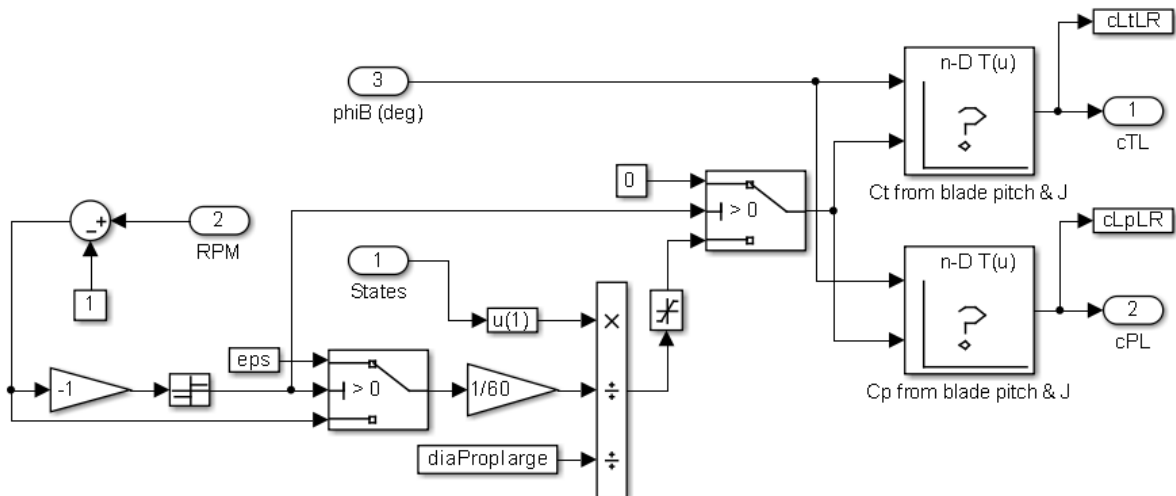


Figure 74: Propeller's thrust and power characteristics

Here we shall further discuss the essential details of the propeller design, small and large diameter. First step is to fix the diameters of the two 6-blade propellers. The propeller's thrust and power characteristics are according to the data given in Figure 15 and Figure 16. The smaller propeller's diameter has been designed for a mean speed of 20 m/s, whereas the larger propeller's diameters for a maximum speed of 45 m/s. Propeller design is for steady forward flights of the given airship configuration with four propulsors at an altitude of 21 km. Propeller's tip Mach numbers are limited to 0.7.

The smaller propeller's design diameter corresponds to the minimum diameter with which the four propulsors are able to produce enough thrust with maximum propeller efficiency (≈ 0.9), such that the airship achieves steady flight at mean speeds of 20 m/s at an altitude of 21 km. For this, the total thrust has to counter the drag experienced by the airship at such flight conditions. The airship drag can be calculated using the following expressions.

$$D = \frac{1}{2} \rho V^2 S_h C_D, \text{ where } S_h = \Lambda^{\frac{2}{3}}$$

$$C_D = 0.23175 - 0.15757 * f + 0.04744 * f^2 - 0.00704 * f^3 + 0.000515 * f^4 - 0.000015 * f^5$$

Here, ρ is the density of surrounding air, V is the forward speed, S_h is the airship's reference area, Λ is the volume of the airship, and f is its fineness ratio. The expression for the drag coefficient C_D is an empirical relation. Similarly, the larger propeller's design diameter is the minimum diameter for which the airship achieves steady flight at maximum speeds of 45 m/s, the maximum propeller efficiency achieved being ≈ 0.93 .

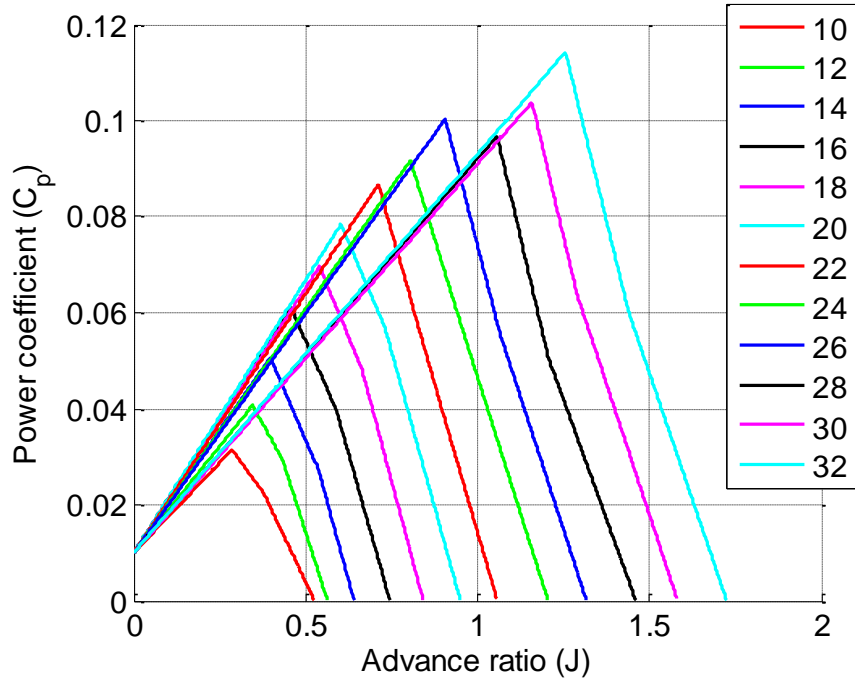


Figure 75: Modified power characteristics of the propeller

For adapting the propeller characteristics of Figure 15 and Figure 16 in the current simulation, the thrust and power values for lower advance ratios (< 0.3) and lower propeller-blade pitch angles (< 10 deg) have been appropriately appended. The final propeller data is shown in Figure 75 and Figure 76. The table lookups of the current simulation are based on this data. Figure 77 shows the corresponding propeller efficiency as a function of advance ratio for different propeller-blade pitch angles. In the same figure, the black dotted curve defined by black squares corresponds to the pitch angle-advance ratio combinations with which airship flight at different thrust conditions is possible while maintaining maximum achievable

propeller efficiency. The blue dotted curve with blue squares gives the corresponding values of the thrust coefficient ($10 * c_t^{maxeff}$), and the equivalent power coefficient values are defined by the red dotted curve with red squares ($10 * c_p^{maxeff}$).

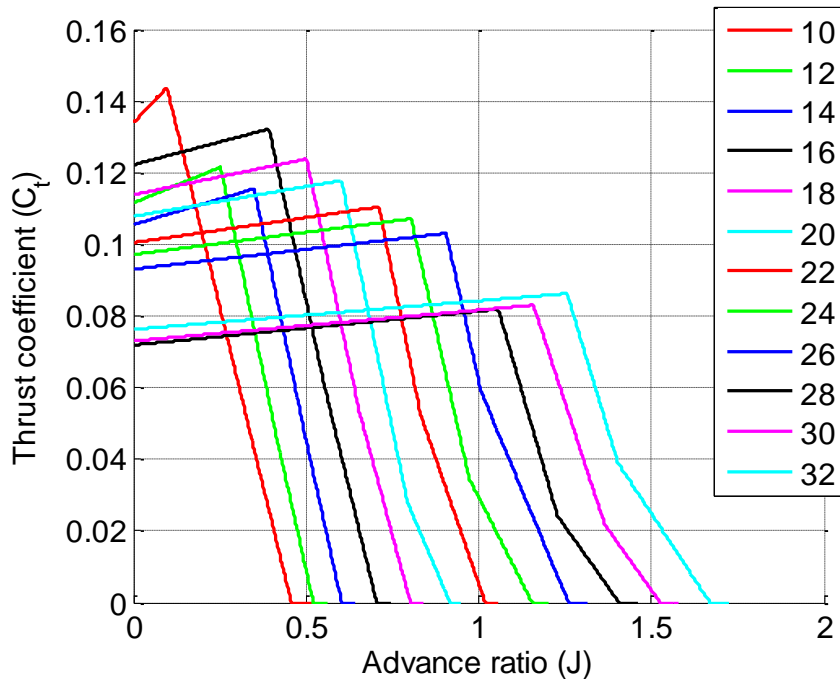


Figure 76: Modified thrust characteristics of the propeller

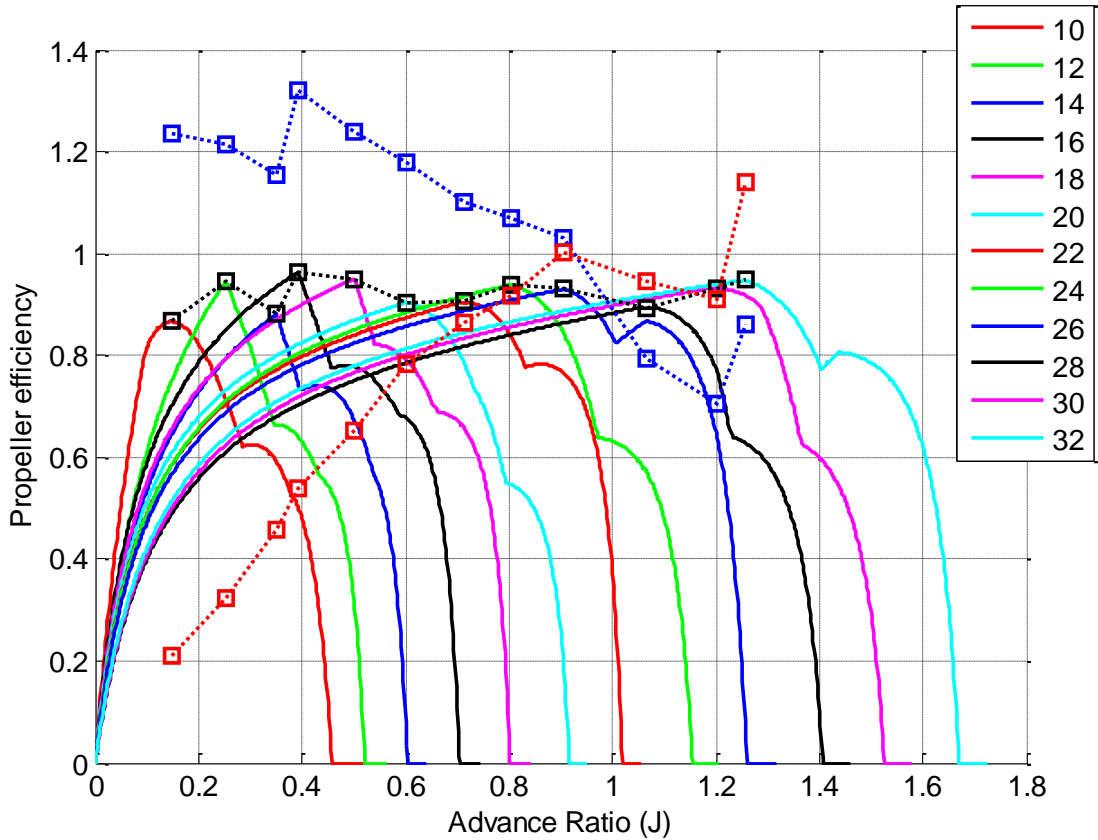


Figure 77: Propeller efficiency as a function of Advance Ratio for different blade pitch angles

3.3.9. System Integration

Four propulsors with the same system architecture as in Figure 65 are combined together to form the full propulsion system for the current airship configuration (Figure 78). The power generated from the PV system is equally distributed among the four propulsors. The density of surrounding air and the airship's forward speed are the two feedback inputs to all the propulsors. Here, whether driving the smaller or the larger propeller, the same throttle command is sent to all the propulsors. In a later version of the propulsion system, the individual throttle commands have been decoupled such that control over individual propulsor throttle is available.

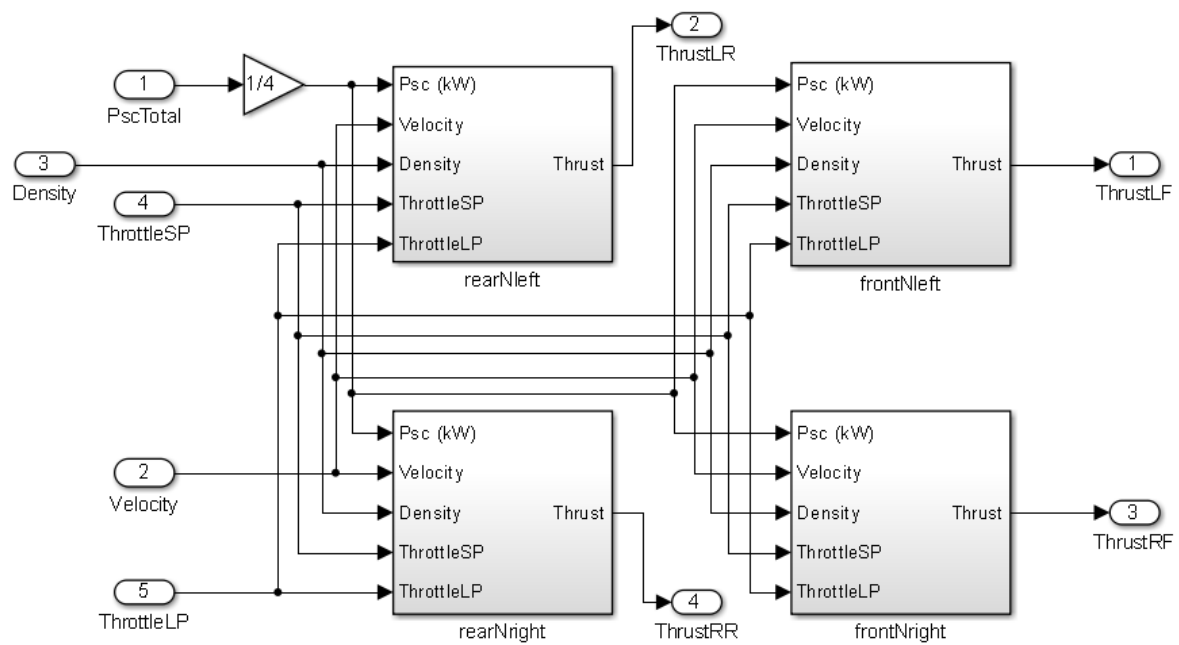


Figure 78: Propulsion system

4. System integration, dynamic analysis, and control

In this work, we develop a fairly-detailed system-level dynamic mathematical model of a High Altitude Airship (HAA) considering all the essential subsystems, and successfully implement it using the MATLAB-Simulink simulation framework. As per the requirement, what we are looking at is to develop an almost-fully autonomous stratospheric airship, which has to operate at altitudes ranging between 18 and 22 km using power from a renewable source of energy and a propulsion system which can efficiently run at those altitudes.

In the current project, solar energy is the renewable source. The operating altitude is around 21 km above the earth's surface where there are no clouds to block the sunlight and wind speeds are relatively lower. The particular HAA system, which is being simulated in this project, has the following design characteristics:

- 1) The hull is modeled as two, axisymmetric ellipsoid halves (Figure 1). Each ellipsoid has the same semi-minor axis, b , but different semi-major axes, a_1 and a_2 .
- 2) The other major structural parts of the airship are a hanging gondola, power and propulsion system, and tail fins for stability and control.
- 3) The power and propulsion system chosen is a photovoltaic/fuel-cell system powering electric motors to drive a propeller for generating thrust.
- 4) As per the design, thin-film solar arrays are used, and they are installed on the upper surface of the airship hull on the envelope material itself.
- 5) Four propulsor units have been chosen for this configuration. Each propulsor unit is a self-sufficient system, i.e. it receives 25% of the power produced by the solar arrays, has an electrolyzer to convert this electric power into Hydrogen and Oxygen, which in turn are sent to the storage tanks. Note that these storage tanks are also a part of the propulsor unit, and whenever there is a power demand from the control system for propulsion or for payload requirements, a fuel cell system starts converting the stored H_2 and O_2 into electric power either for the motor to run the propellers or for running some payload unit.

The essential details of all the mathematical models are described in Section 2 above. Development of the individual Simulink models, their validation results, and system integration of each of the three essential dynamic subsystems of an HAA (Flight Dynamics, Power, and Propulsion), is the subject matter of Section 3 above. Here in this section, we shall mainly focus on the system integration issues and the results obtained with respect to the dynamics and control of the overall Airship system.

To begin with, we will briefly discuss the three essential dynamic subsystems of an HAA: flight dynamics system, power system, and propulsion system. An airship's typical flight dynamics system (including navigation) can be modelled using Simulink as given in Figure 52. Also Figure 53 captures the block diagram of its main subsystem, i.e. 'Forces and Moments'. This Simulink model applies to a case in which flight dynamics of the airship has been

mathematically modelled with respect to a local NED frame based on the Flat-Earth approximation. Engines are simply modelled as two inputs, a total thrust magnitude and a pitch-vectoring angle, one each on either side of the airship. Also, this model is applicable only for a “no wind” case.

The airship flight dynamics is essentially described in terms of the following dynamic state variables: axial (u), lateral (v) and normal (w) velocities, roll (p), pitch (q) and yaw (r) angular rates, roll (ϕ), pitch (θ) and yaw (ψ) Euler angles, and x , y , z positions. The dynamics can be decoupled into two distinctive modes: longitudinal and lateral-directional.

The longitudinal mode consists of following four states:

- 1) Axial velocity (u)
- 2) Normal velocity (w)
- 3) Pitch rate (q)
- 4) Pitch angle (θ)

These states can be affected by using the following three controls:

- 1) Thrust Throttle (τ)
- 2) Thruster pitch-vectoring angle (μ , fore-aft differential actuation)
- 3) Symmetric elevator deflection (δ_{elv} , left and right)

The lateral-directional mode consists of the following states:

- 1) Lateral velocity (v)
- 2) Roll rate (p)
- 3) Yaw rate (r)
- 4) Roll angle (ϕ)

These states can be affected by using the following three controls:

- 1) Symmetric rudder deflection (δ_{rud} , top and bottom)
- 2) Differential elevator and rudder deflection (δ_{ail})
- 3) Thruster pitch-vectoring angle (μ , port-starboard differential actuation)

Longitudinal level-trim (equilibrium) flight solutions were obtained for the given airship configuration at the following forward speeds: 15 m/s and 30 m/s. For this, the “TRIM” command in Matlab software was used. For these level-trim solutions, the lateral-directional state variables and controls are all zero. In the longitudinal plane, the rates of change of the different states also have to be zero, i.e. $q = 0$. Search is done for a level-trim solution with zero angle of attack, so $w = 0$ and $\theta = 0$. Thus the “TRIM” command finds out a control triplet (τ , μ , δ_{elv}) which leads to such a level-trim solution of the airship flight. Further, the command “LINMOD” in Matlab software was used to calculate the stability and control matrices at each of the equilibrium solutions.

For flight at 15 m/s, a total thrust of $\tau = 1471.9$ N is required from the two thrusters (port and starboard, 735.95 N each) with the thruster pitch-vectoring angle of each being -0.2928 rad

(-16.77 deg) and the elevator deflections, left and right, being 0.0226 rad (1.3 deg) each. The longitudinal stability eigenvalues and eigenvectors of this trim solution are as given below.

Eigenvalue matrix, $D =$

$$\begin{bmatrix} -0.7273 & 0 & 0 & 0 \\ 0 & -0.0051 & 0 & 0 \\ 0 & 0 & -0.0262 + 0.0035i & 0 \\ 0 & 0 & 0 & -0.0262 - 0.0035i \end{bmatrix}$$

Eigenvector matrix, $V (u, w, q, \theta) =$

$$\begin{array}{cccc} 0.7905 + 0.0000i & 0.9988 + 0.0000i & 0.0051 - 0.0082i & 0.0051 + 0.0082i \\ -0.5853 + 0.0000i & -0.0492 + 0.0000i & -0.9992 + 0.0000i & -0.9992 + 0.0000i \\ -0.1061 + 0.0000i & 0.0000 + 0.0000i & -0.0005 + 0.0009i & -0.0005 - 0.0009i \\ 0.1459 + 0.0000i & -0.0021 + 0.0000i & 0.0244 - 0.0314i & 0.0244 + 0.0314i \end{array}$$

The lateral-directional stability eigenvalues and eigenvectors are as given below.

Eigenvalue matrix, $D =$

$$\begin{bmatrix} -0.0278 & 0 & 0 & 0 \\ 0 & -0.0710 + 0.4323i & 0 & 0 \\ 0 & 0 & -0.0710 - 0.4323i & 0 \\ 0 & 0 & 0 & -2.3065 \end{bmatrix}$$

Eigenvector matrix, $V (v, p, r, \phi) =$

$$\begin{array}{cccc} 1.0000 + 0.0000i & 0.8300 + 0.0000i & 0.8300 + 0.0000i & -0.9906 + 0.0000i \\ 0.0001 + 0.0000i & -0.1112 - 0.1938i & -0.1112 + 0.1938i & -0.1161 + 0.0000i \\ 0.0002 + 0.0000i & 0.0203 - 0.0237i & 0.0203 + 0.0237i & -0.0520 + 0.0000i \\ -0.0026 + 0.0000i & -0.3955 + 0.3221i & -0.3955 - 0.3221i & 0.0503 + 0.0000i \end{array}$$

For flight at 30 m/s ($u = 30$, $w = 0$, $\theta = 0$), a total thrust of $\tau = 5887.8$ N is required from the two thrusters (port and starboard, 2943.9 N each) with the thruster pitch-vectoring angle of each being -0.2928 rad and the elevator deflections, left and right, being 0.0226 rad each. The longitudinal stability eigenvalues and eigenvectors of this trim solution are as given below.

Eigenvalues matrix, $D =$

$$\begin{bmatrix} -1.4985 & 0 & 0 & 0 \\ 0 & -0.0465 & 0 & 0 \\ 0 & 0 & -0.0147 & 0 \\ 0 & 0 & 0 & -0.0102 \end{bmatrix}$$

Eigenvectors matrix, $V =$

-0.80536	0.00235	-0.10212	0.99736
0.57835	0.99998	-0.9534	-0.07168
0.10814	-0.00025	0.00416	0.00012
-0.07216	0.00533	-0.28387	-0.01187

The lateral-directional stability eigenvalues and eigenvectors are as given below.

Eigenvalues matrix, D =

$$\begin{bmatrix} -4.8296 & 0 & 0 & 0 \\ 0 & -0.0556 & 0 & 0 \\ 0 & 0 & -0.0337 + 0.4270i & 0 \\ 0 & 0 & 0 & -0.0337 - 0.4270i \end{bmatrix}$$

Eigenvectors matrix, V =

0.9910 + 0.0000i	-1.0000 + 0.0000i	0.7702 + 0.0000i	0.7702 + 0.0000i
0.1203 + 0.0000i	-0.0003 + 0.0000i	-0.2227 - 0.1158i	-0.2227 + 0.1158i
0.0525 + 0.0000i	-0.0002 + 0.0000i	0.0055 - 0.0169i	0.0055 + 0.0169i
-0.0249 + 0.0000i	0.0052 + 0.0000i	-0.2284 + 0.5397i	-0.2284 - 0.5397i

Wind can be incorporated by including a subsystem called “Wind calculations” and making some modifications in the “Coriolis and Centrifugal” subsystem of the “Forces and Moments” model. The Geodetic flight dynamics of the airship, in which the equations of motion (EoM) are written with respect to the Earth-Centered Inertial frame, is obtained by essentially modifying the “Navigation” and “Wind calculations” subsystems of the Flat-Earth Simulink model. The modified Simulink model, which includes the wind incorporation and the Geodetic dynamics, is shown in Figure 79.

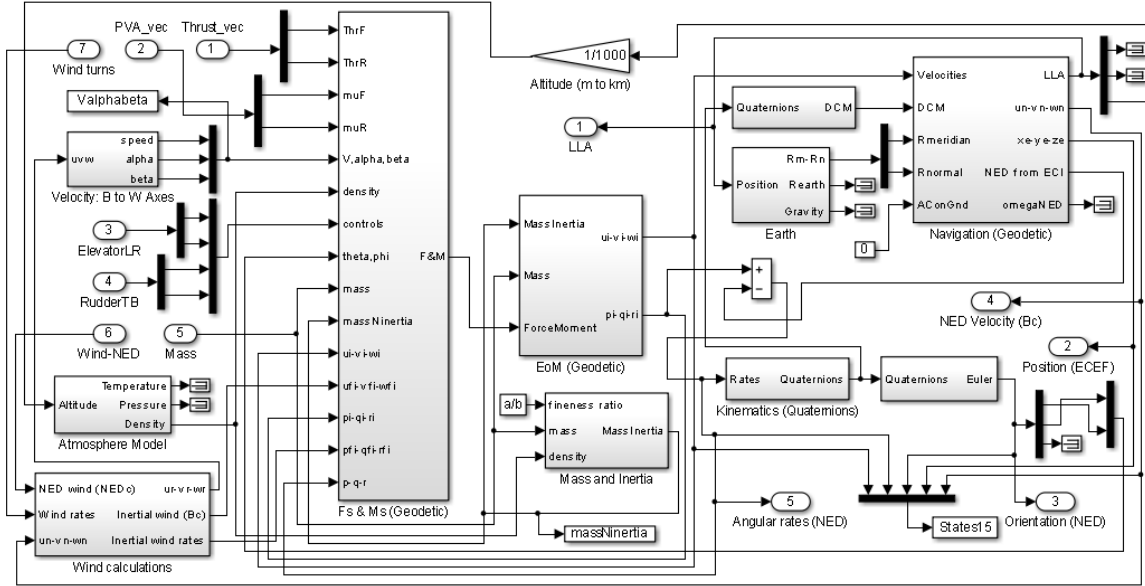


Figure 79: Simulink model for flight dynamics of an HAA with respect to the Earth-Centered Inertial (ECI) frame

The “Forces and Moments” subsystem of this geodetic model is given in Figure 80, and the corresponding Navigation and Wind calculations subsystems are shown in Figure 81 and Figure 82.

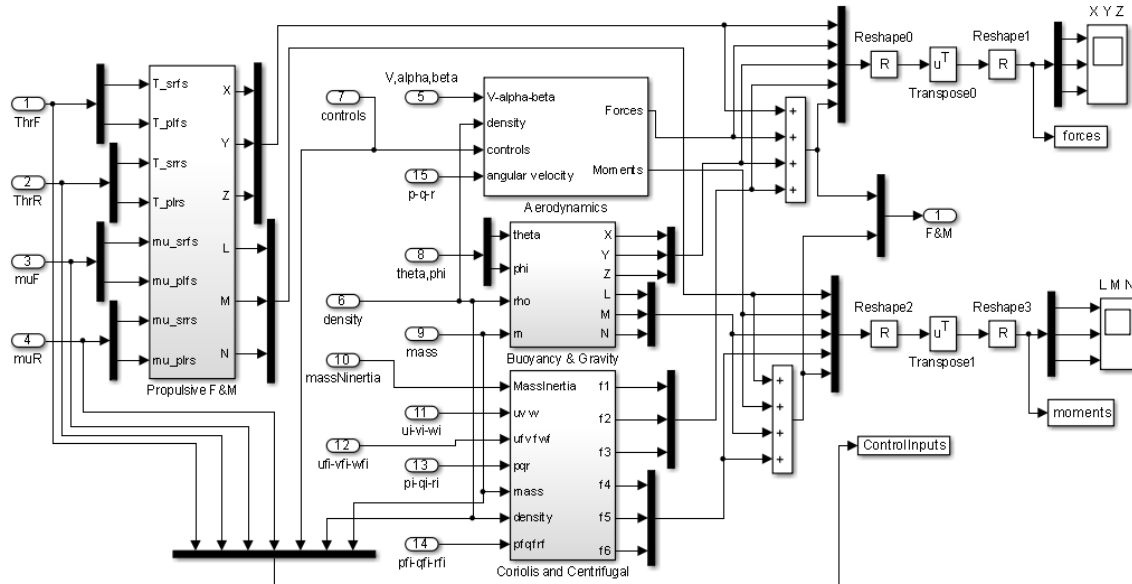


Figure 80: Simulink model of the “Forces and Moments” subsystem; airship flight dynamics model in ECI frame

Also, here the “Propulsive Forces and Moments” subsystem has been modified to incorporate two starboard-side propulsors and two port-side propulsors. On each side, each propulsor is positioned, equidistant, fore and aft of the Centre of Gravity (CG).

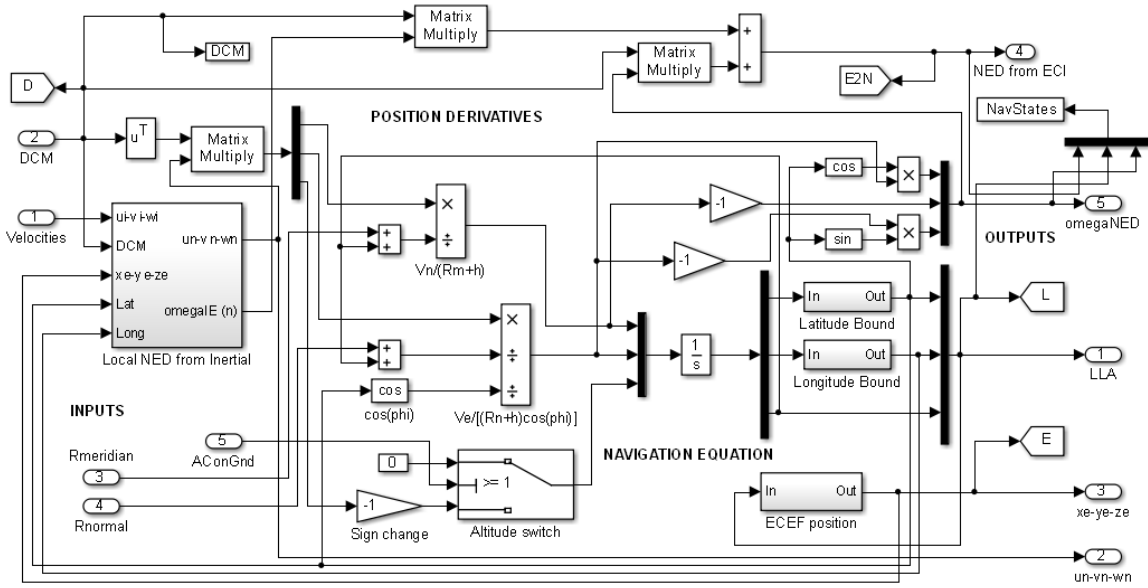


Figure 81: Navigation subsystem; airship flight dynamics model in ECI frame

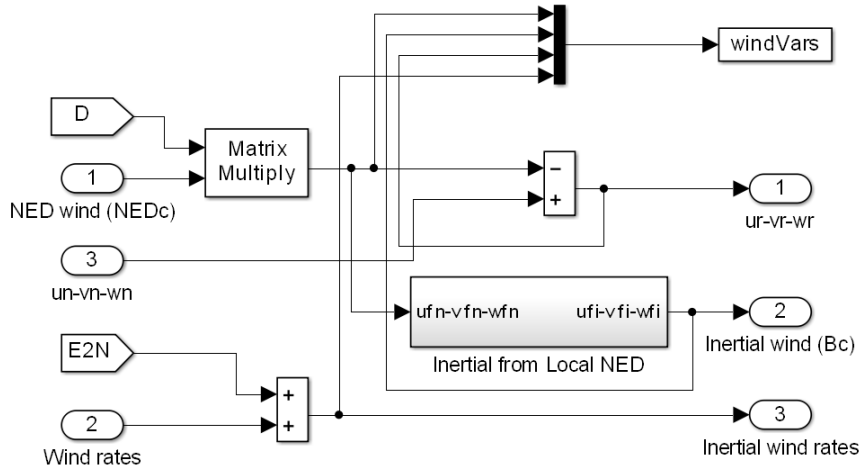


Figure 82: Wind calculations subsystem; airship flight dynamics model in ECI frame

Note that the basic flight dynamic model has not changed except for a few additional changes in the moments of inertia. The final set of parameters is included in the Appendix (Section 6). The trim and stability analysis have been repeated for the fully modified wind-included four-thruster airship flight dynamic system. The results are provided here for flight at 15 m/s (air-reference speed). A total thrust of $\tau = 1450$ N is required from the four thrusters (two front and two rear, 362.5 N each) with the thruster pitch-vectoring angle of each being -0.2442 rad (-14 deg) and the elevator deflections, left and right, being 0.0187 rad (1.07 deg) each. This trim calculation was done with a background wind of 15 m/s in the same direction as the flight direction, thus making the inertial velocity of the airship 30 m/s.

The longitudinal stability eigenvalues and eigenvectors of this trim solution are as given below.

Eigenvalues matrix, $D =$

$$\begin{bmatrix} -0.5156 & 0 & 0 & 0 \\ 0 & -0.0051 & 0 & 0 \\ 0 & 0 & -0.0265 + 0.0035i & 0 \\ 0 & 0 & 0 & -0.0265 - 0.0035i \end{bmatrix}$$

Eigenvectors matrix, V =

$$\begin{array}{cccc} 0.6740 + 0.0000i & 0.9992 + 0.0000i & -0.0056 + 0.0080i & -0.0056 - 0.0080i \\ -0.7121 + 0.0000i & -0.0406 + 0.0000i & 0.9991 + 0.0000i & 0.9991 + 0.0000i \\ -0.0902 + 0.0000i & 0.0000 + 0.0000i & 0.0006 - 0.0009i & 0.0006 + 0.0009i \\ 0.1750 + 0.0000i & -0.0017 + 0.0000i & -0.0261 + 0.0304i & -0.0261 - 0.0304i \end{array}$$

The lateral-directional stability eigenvalues and eigenvectors are as given below.

Eigenvalues matrix, D =

$$\begin{bmatrix} -0.0279 & 0 & 0 & 0 \\ 0 & -0.0536 + 0.4383i & 0 & 0 \\ 0 & 0 & -0.0536 - 0.4383i & 0 \\ 0 & 0 & 0 & -0.7959 \end{bmatrix}$$

Eigenvectors matrix, V =

$$\begin{array}{cccc} 1.0000 + 0.0000i & 0.8649 + 0.0000i & 0.8649 + 0.0000i & -0.9970 + 0.0000i \\ 0.0001 + 0.0000i & -0.0358 - 0.1993i & -0.0358 + 0.1993i & -0.0446 + 0.0000i \\ 0.0002 + 0.0000i & 0.0192 - 0.0188i & 0.0192 + 0.0188i & -0.0289 + 0.0000i \\ -0.0024 + 0.0000i & -0.4382 + 0.1352i & -0.4382 - 0.1352i & 0.0560 + 0.0000i \end{array}$$

The power system is modelled as shown in Figure 63. Its power-generating component, i.e. “Day time” subsystem, has architecture as given in Figure 83 (same as Figure 64). Sun Position (Figure 59) and PV array calculations (Figure 61) are the two primary functional subsystems of the power generation model.

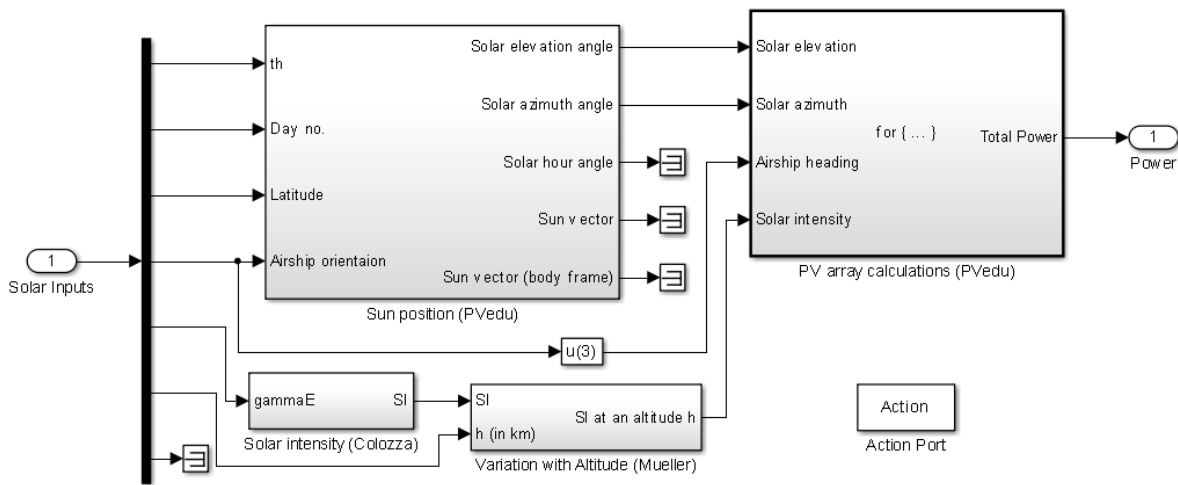


Figure 83: “Day time” subsystem

A typical output of the power generation component (Figure 83) is shown in Figure 84.

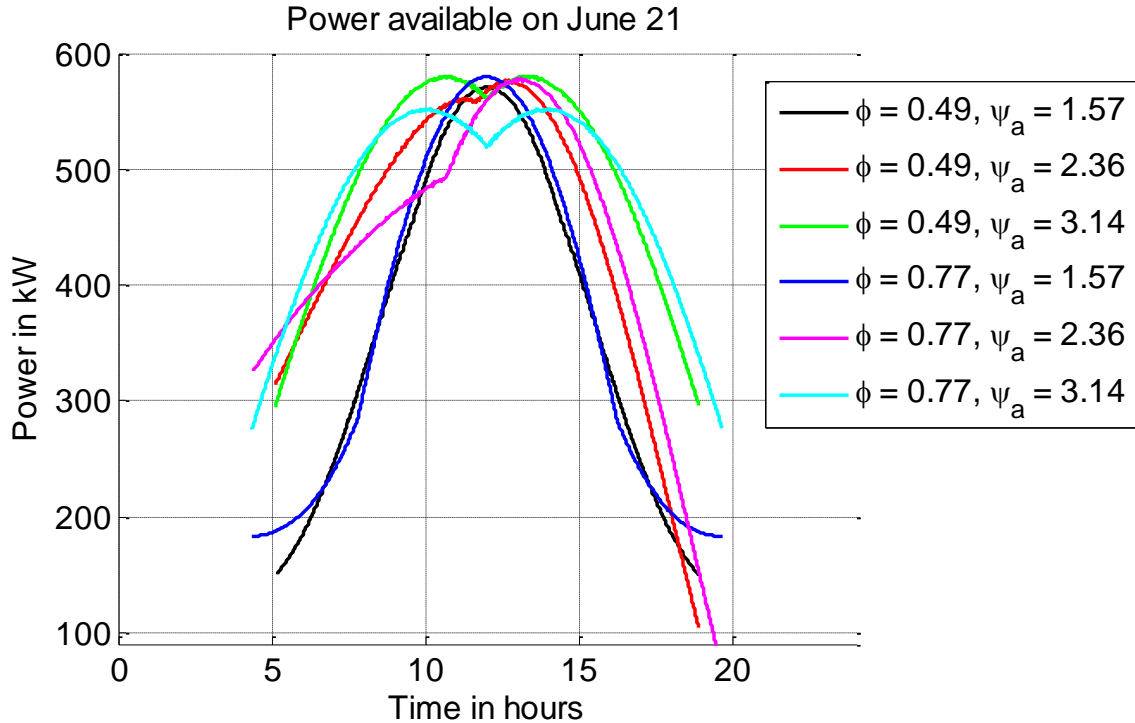


Figure 84: Power output during a particular day for different latitudes (ϕ) and airship orientations (ψ_a)

It shows the total power generated (in kW) by the entire solar array structure (installed on the top surface of the airship hull) as a function of time (in hours, from sunrise to sunset) on a typical day such as June 21 for six combinations of airship position and orientation (two latitudes, ϕ × three headings, ψ_a).

The propulsion system is modelled as shown in Figure 85 (same as Figure 78).

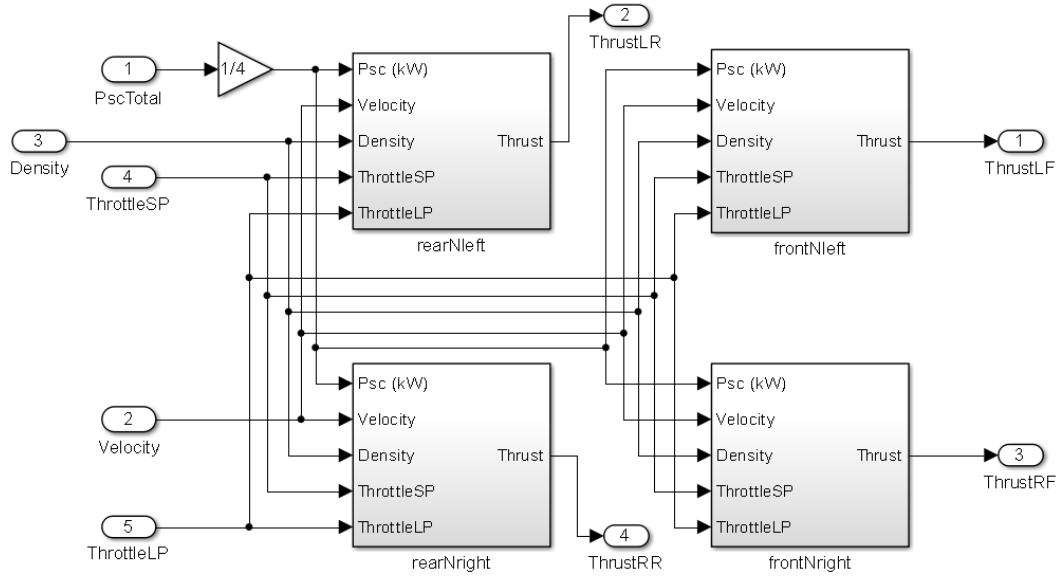


Figure 85: Airship propulsion system with four propulsors

Functionally, each propulsor has system architecture as shown in Figure 86 (same as Figure 65). The power generated from the solar arrays is equally distributed among the four propulsors. The propeller calculations need information on atmospheric density and the airship's flight velocity, and each propulsor has two propellers, a small-diameter propeller which is designed for typical average wind speeds that the airship will have to go through (20 m/s) for flights at stratospheric altitudes (19 – 22 km) and a large-diameter propeller which is designed for maximum wind speeds (45 m/s) that the airship will have to endure at those altitudes.

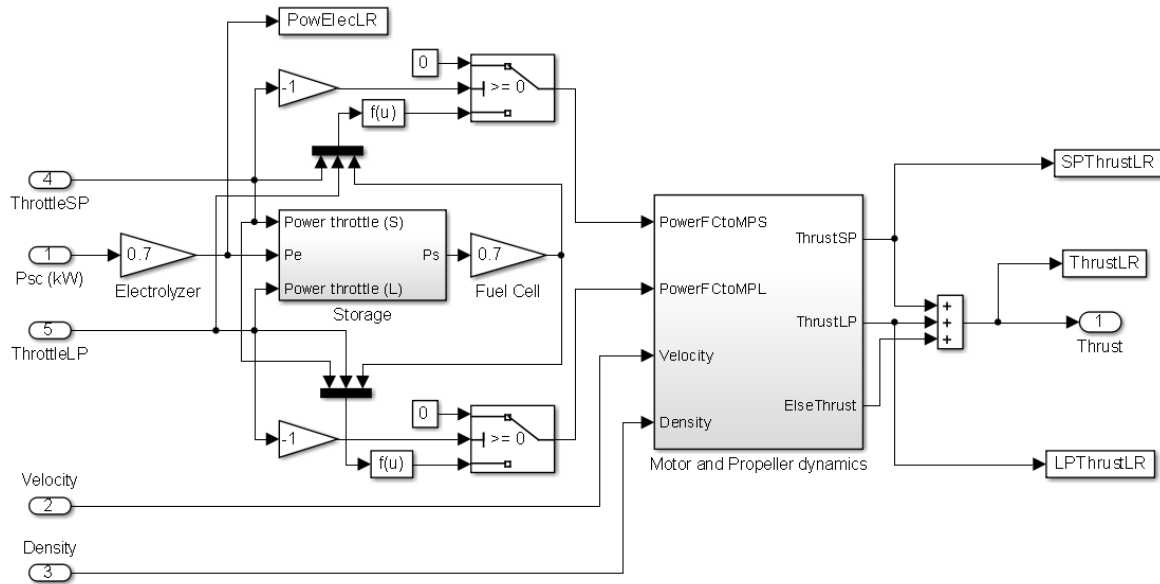


Figure 86: System architecture of a single propulsor

Only a fraction of the input solar power P_{sc} is passed on by the electrolyzer, which in turn gets stored in the storage unit. The actual driving power input to the propulsor is the power drawn out of this storage unit, P_s . This power has been converted into a throttle input, which is defined as the ratio given below:

$$\eta = \frac{\text{Input Power drawn out of the storage unit}}{\text{Design Maximum Power corresponding to design airship speed}} = \frac{P_s}{P_{s,max}}$$

Thus each propulsor has two throttle inputs, one each for the smaller (denoted by *SP*) and larger (denoted by *LP*) propellers. Each of these propellers is driven by separate motors, the maximum power rating $P_{f,max}$ of these two motors being different. The smaller propeller is designed for airships flying at 20 m/s, and the motor driving this propeller will have a maximum power rating equal to the power required to drive the propeller at that forward speed (considering all the efficiencies). Similarly, the motor driving the larger propeller should have a higher $P_{f,max}$ since it is supposed to perform at maximum airship speeds around 45 m/s. For more details, refer Section 3.3.

Note that the subscript *LR* stands for Left-Rear, and the other propulsor units have similar nomenclature for their individual parameters, i.e. *LF* (Left-Front), *RF* (Right-Front) and *RR* (Right-Rear). In Figure 85, for smaller or larger propellers, the same throttle input signal is fed to each propulsor, i.e. at a time all the propulsors will be generating the same thrust magnitude. Differential thrusting has been made possible in a subsequent variant of this propulsion system as part of control applications. In that case, the four throttle inputs (smaller or larger propeller) will be independent of each other. Note that the pitch-vectoring angle input of each propulsor is separate from all this and they can be assigned independently.

Integration of the full HAA system has been achieved by following through various integration steps, which depend on the particular model choice considered in each of the three cases given below:

- a) whether the power and propulsion systems are included, i.e. whether the system being studied is the full HAA system or only its Flight Dynamics subsystem
- b) whether the Flight Dynamics subsystem is a Flat-Earth model or Geodetic model
- c) whether a Control System is included or not (i.e. Open-Loop or Closed-Loop)

The results shown in Figure 87 to Figure 90 correspond to different control-input-perturbation responses of the Open-Loop Flat-Earth flight dynamics system with four thrusters flying at a trim speed of 15 m/s. (Trim: Thrust required is 1450 N (4×362.5), pitch-vectoring angle of each thruster is -0.2442 rad, and the elevator deflections, left and right, are 0.0187 rad each.) For these results, the power and propulsion systems are not included, i.e. the basic Flight Dynamics subsystem is being studied. The control-input perturbations are introduced at $t = 0$ in the form of step inputs. In Figure 87, the thrust produced by each thruster is increased by 100 N. This results in increased velocity (17 m/s) in the surge (axial) direction with some transitional pitch and heave dynamics which lasts for around 700 seconds.

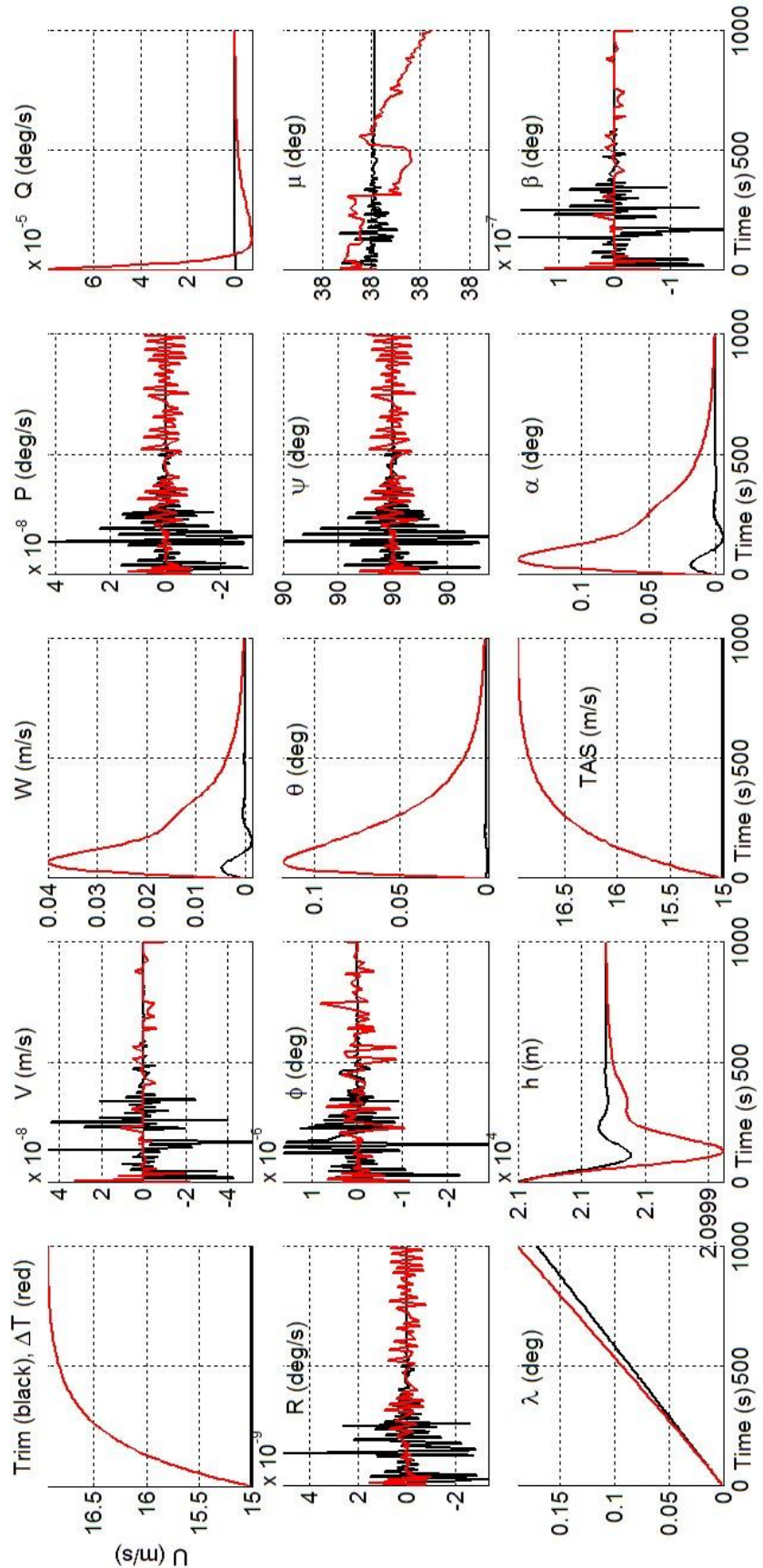


Figure 87: Control input perturbation results for Open-Loop Flat-Earth airship flight dynamics system; a positive thrust perturbation of 100 N per thruster (total $\Delta T = 400$ N).

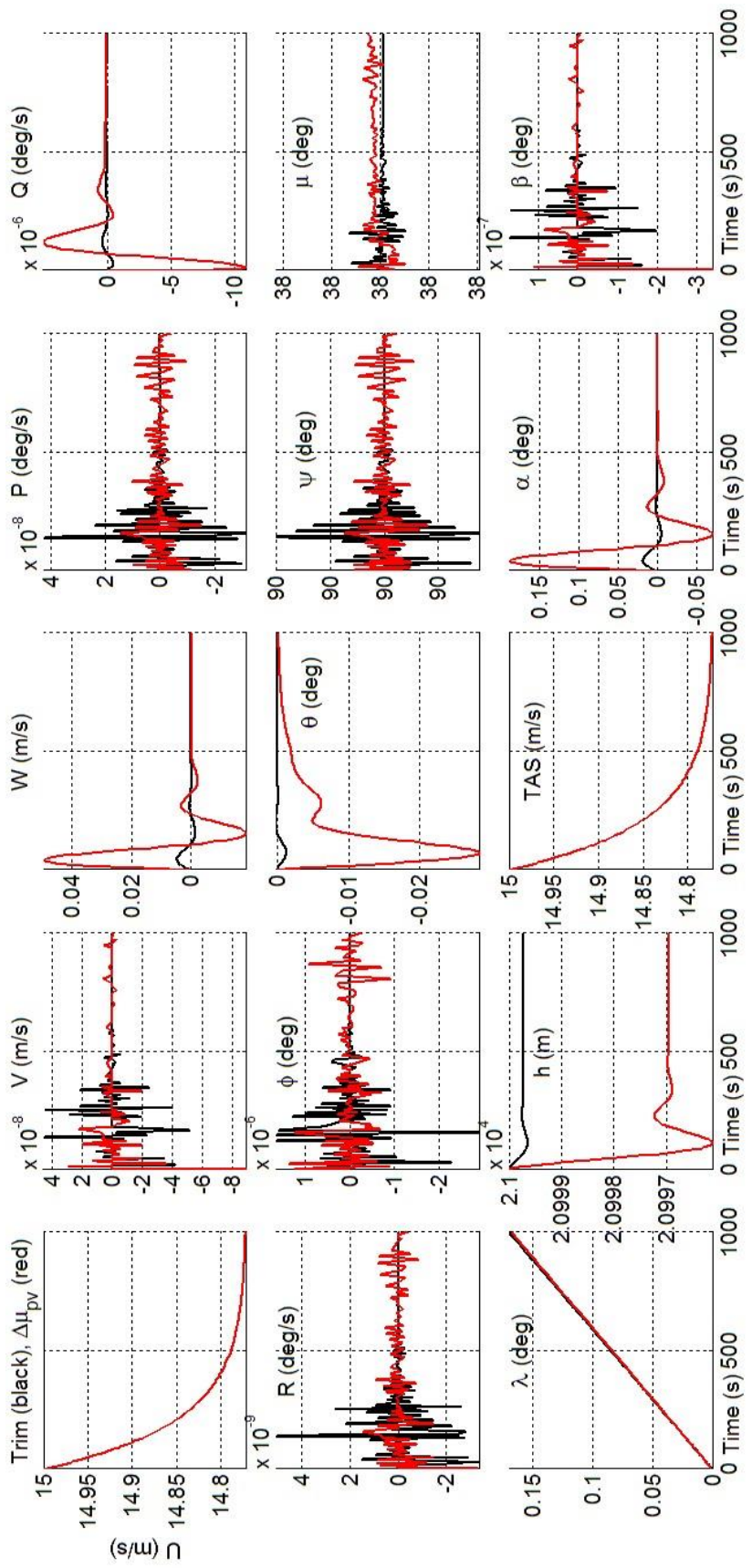


Figure 88: Control input perturbation results for Open-Loop Flat-Earth airship flight dynamics system; a negative perturbation of -0.1 rad (≈ -5.7 deg) in the pitch-vectoring angle of each thruster ($\Delta\mu = -0.1$ rad).

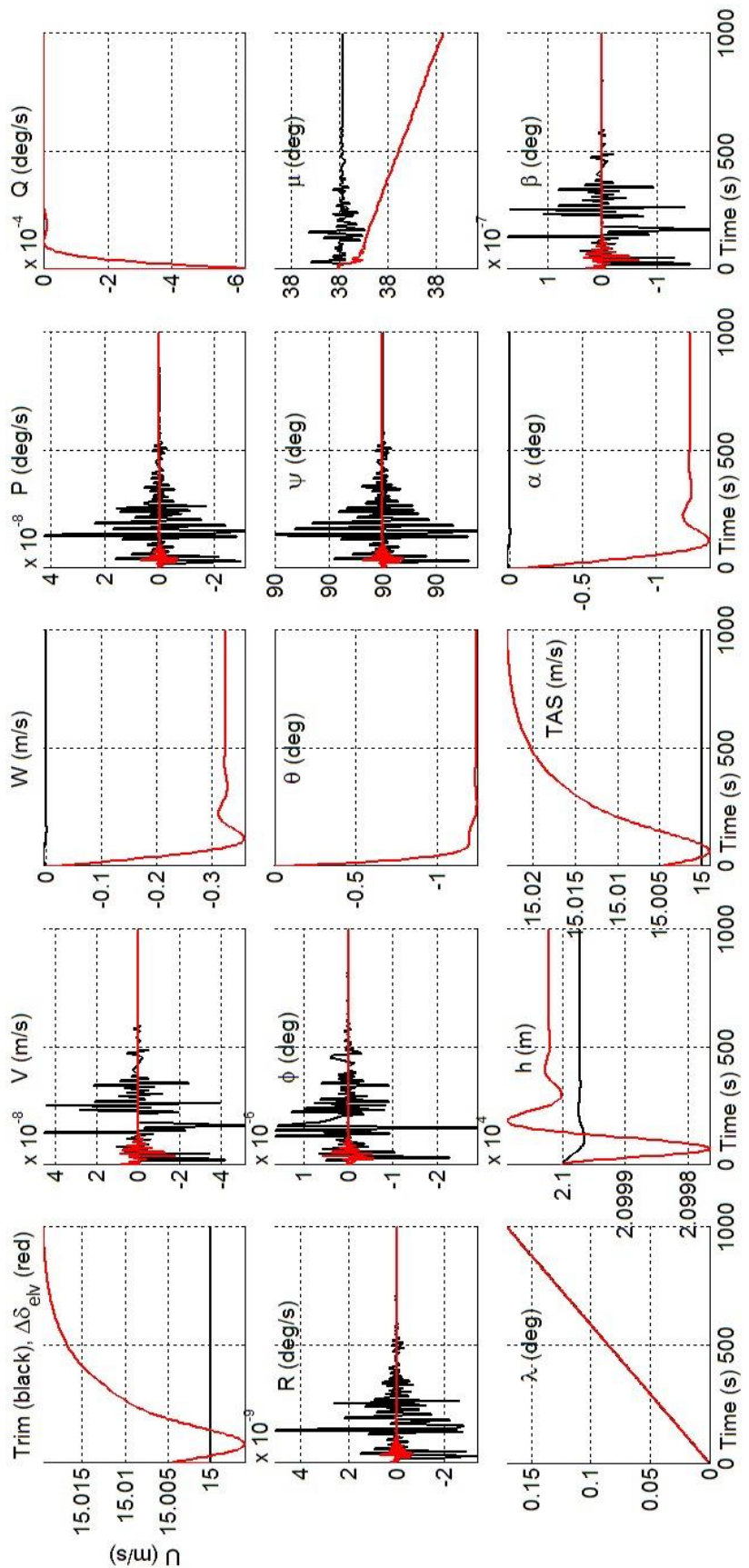


Figure 89: Control input perturbation results for Open-Loop Flat-Earth airship flight dynamics system; a positive perturbation of 0.03 rad (1.72 deg) in each of the elevator deflections, left and right.

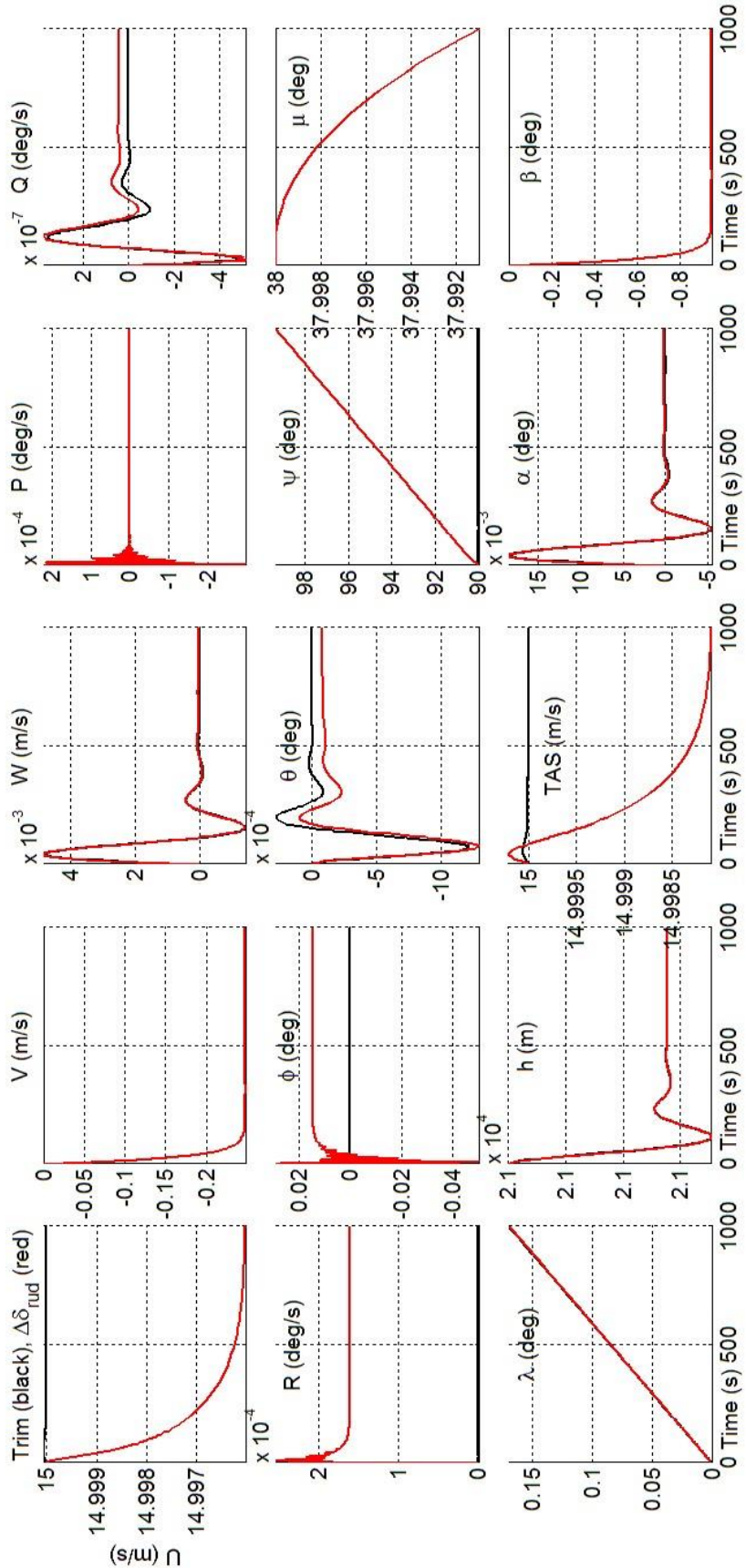


Figure 90: Control input perturbation results for Open-Loop Flat-Earth airship flight dynamics system; a positive perturbation of 0.01 rad (≈ 0.6 deg) in each of the rudder deflections, top and bottom.

In Figure 88, a negative perturbation of -5.7 deg is given in the pitch-vectoring angle of all the four thrusters. Essentially, the down thrust is slightly increased and the forward thrust is slightly decreased. This results in a slight decrease in the airship's surge velocity and altitude. The transitional pitch and heave dynamics die down within 500 seconds. In Figure 89, the elevator deflection (left and right) is increased from its trim value (1.07 deg) by 1.72 deg. This results in a small increase in altitude and axial velocity. Again, the transitional pitch and heave dynamics die down within 500 seconds. In Figure 90, a positive rudder deflection (top and bottom) of 0.6 deg results in a small negative lateral velocity (-0.25 m/s) and a small positive yaw rate (0.0016 deg/s). Also, while turning, the airship rolls into a steady roll angle of 0.015 deg. Note that the lateral-directional dynamics is over within 100 seconds, indicative of the relatively higher stability eigenvalues of the lateral-directional Jacobian matrix.

The power, propulsion and flight dynamics systems discussed before have been assembled to build the full airship dynamic system. The Simulink model of the same is shown in Figure 91. The results for a typical forward motion of this airship are given in Figure 92 to Figure 95. These results were produced by giving a constant throttle command of 0.43 to the smaller-diameter propeller of all the four propulsors. The pitch-vectoring angle of each propulsor is set to a constant value of -0.244 rad (-0.0777π -rad in Figure 92), and the elevator deflection (left and right) is held at 0.1859 rad (0.0592π -rad in Figure 92). It is observed that each propulsor produces a steady thrust of around 300 N, and the airship is flying level at a net speed of 14 m/s (in body components, 13.9 m/s axial velocity and -1.2 m/s normal velocity; $\alpha = \theta \approx -5$ deg). See Figure 92 and Figure 93. Note that the flight dynamics system here is a Flat-Earth model, and hence NED velocities are the inertial velocities.

Also, Figure 94 shows the variation of different power and propulsion system variables. The simulation is set up such that it starts at sunrise of a particular day, and the total simulation run-time is 3600 seconds (1 hr). The power produced by the PV array system starts from around 250 kW at sunrise (increases during the day), which gets equally distributed among the four propulsors. After the electrolyser efficiency, each electrolyser's output is approximately 44 kW at sunrise. The rest of the parameters shown in Figure 94 are all for a single propulsor. Throttle command is such that 9.37 kW is drawn from each propulsor's storage, and the input power to the motor, i.e. the fuel cell output, is 6.56 kW. At the steady state of the motor-propeller system, the various parameters' values are as follows (smaller-diameter propeller is being driven):

- i) Motor current is 17.3 A
- ii) Blade pitch angle of the propeller is 20 deg
- iii) Thrust coefficient is 0.1145 and power coefficient is 0.0773
- iv) Motor torque is 313.2 N-m
- v) Thrust produced is 291.2 N and propeller RPM is 172.85
- vi) Load torque is 41.7 N-m and power absorbed is 4.53 kW

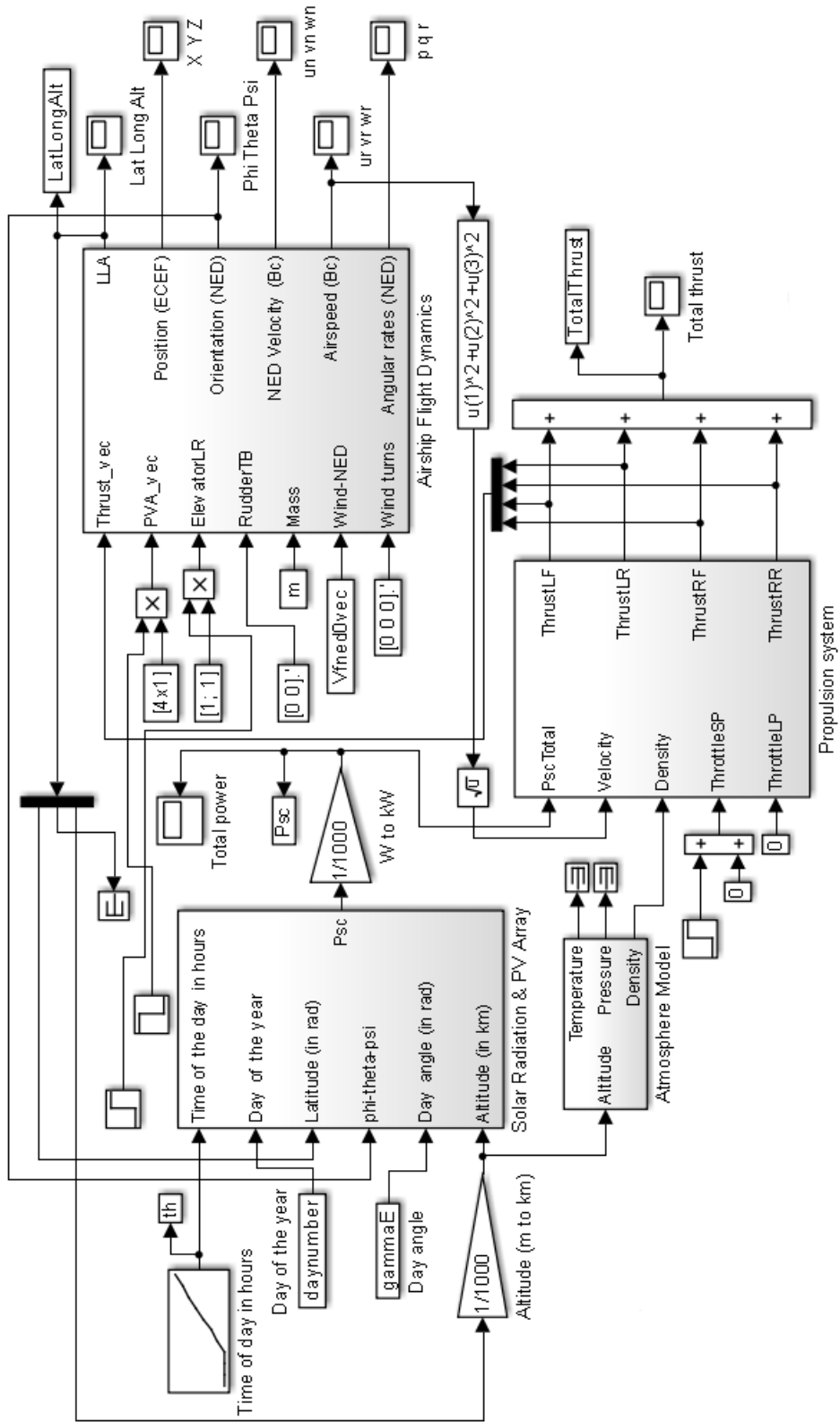


Figure 91: Simulink model of Airship System dynamics: Power system, Propulsion system and Flight dynamics

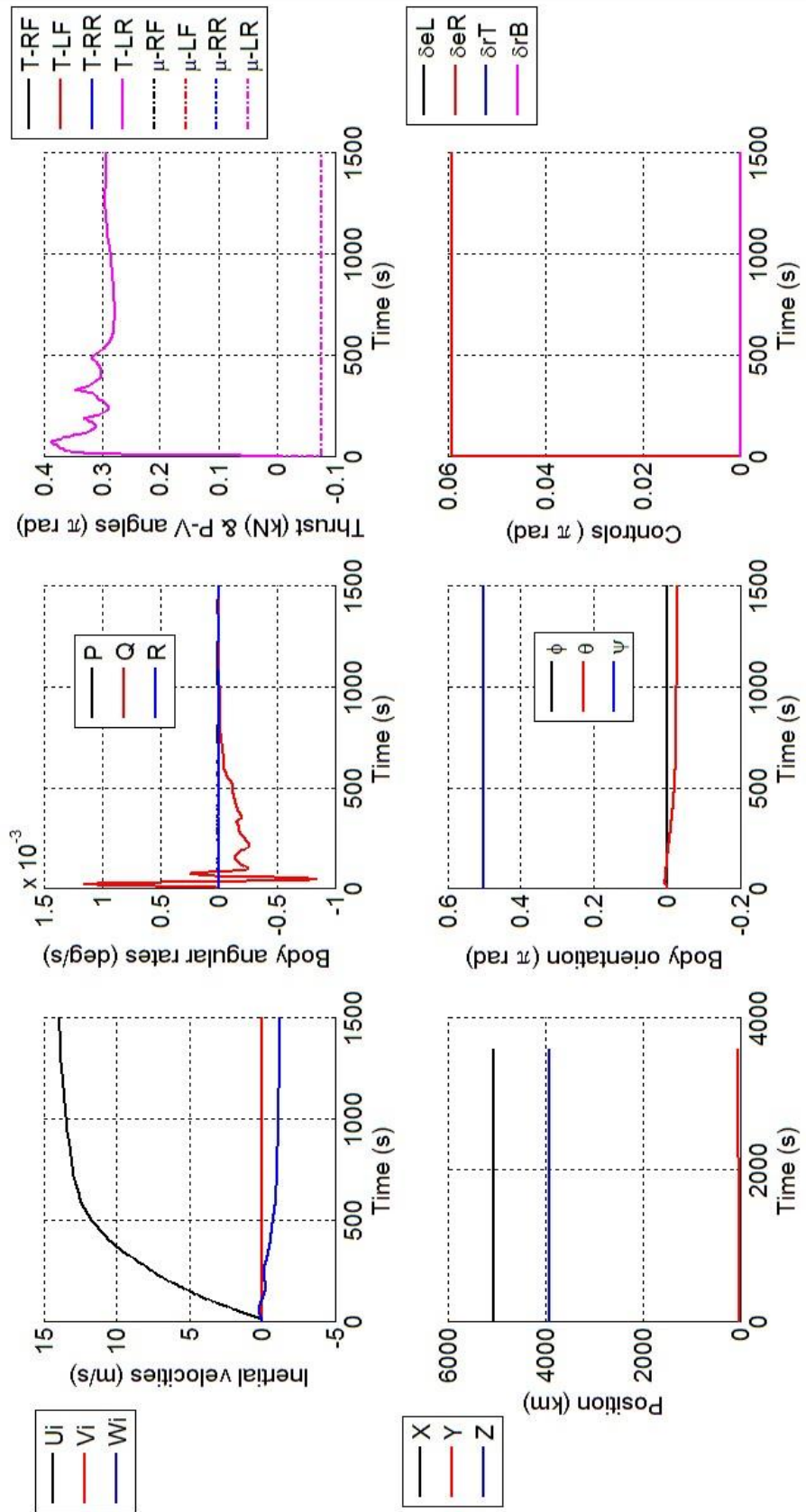


Figure 92: A typical forward motion of the Airship for a throttle command of 0.43 to the smaller-diameter propeller of all the propulsors; Euler angles, control actuator angles and thruster pitch-vectoring angle have been plotted in terms of π rad.

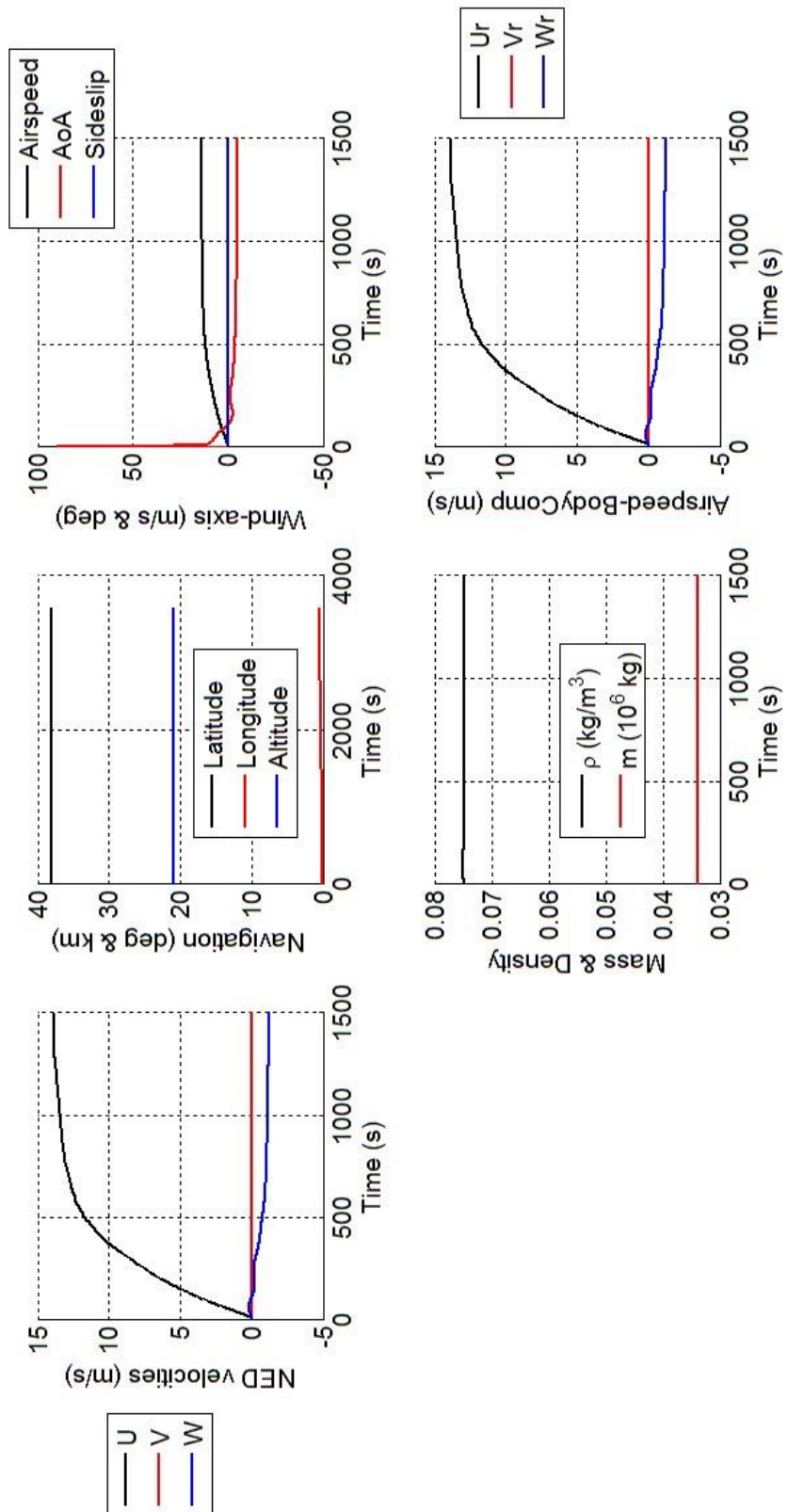


Figure 93: A typical forward motion of the Airship for a throttle command of 0.43 to the smaller-diameter propeller of all the propulsors; airspeed parameters, inertial velocities and navigation variables.

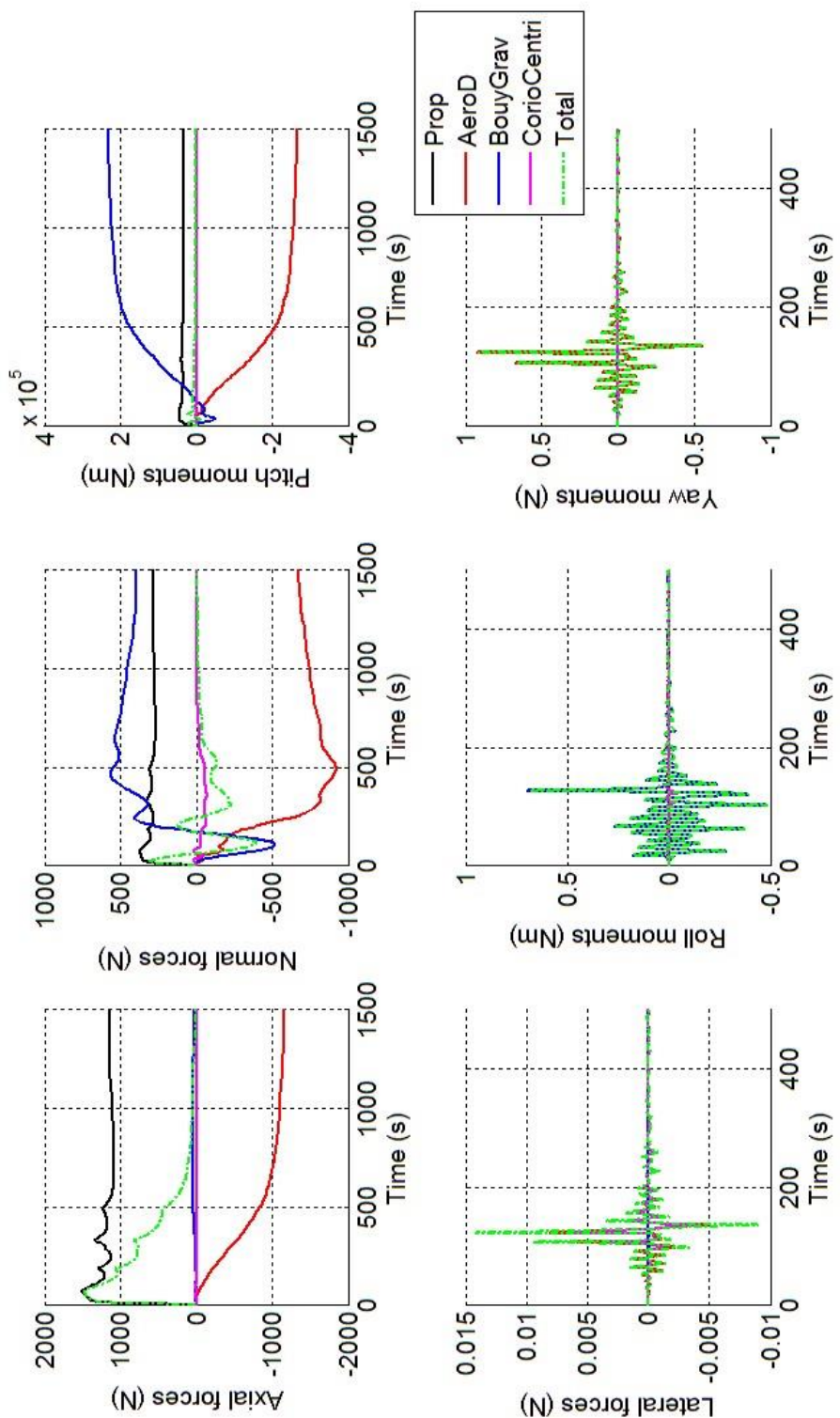


Figure 94: A typical forward motion of the Airship for a throttle command of 0.43 to the smaller-diameter propeller of all the propulsors; different components of the longitudinal, lateral and directional forces and moments.

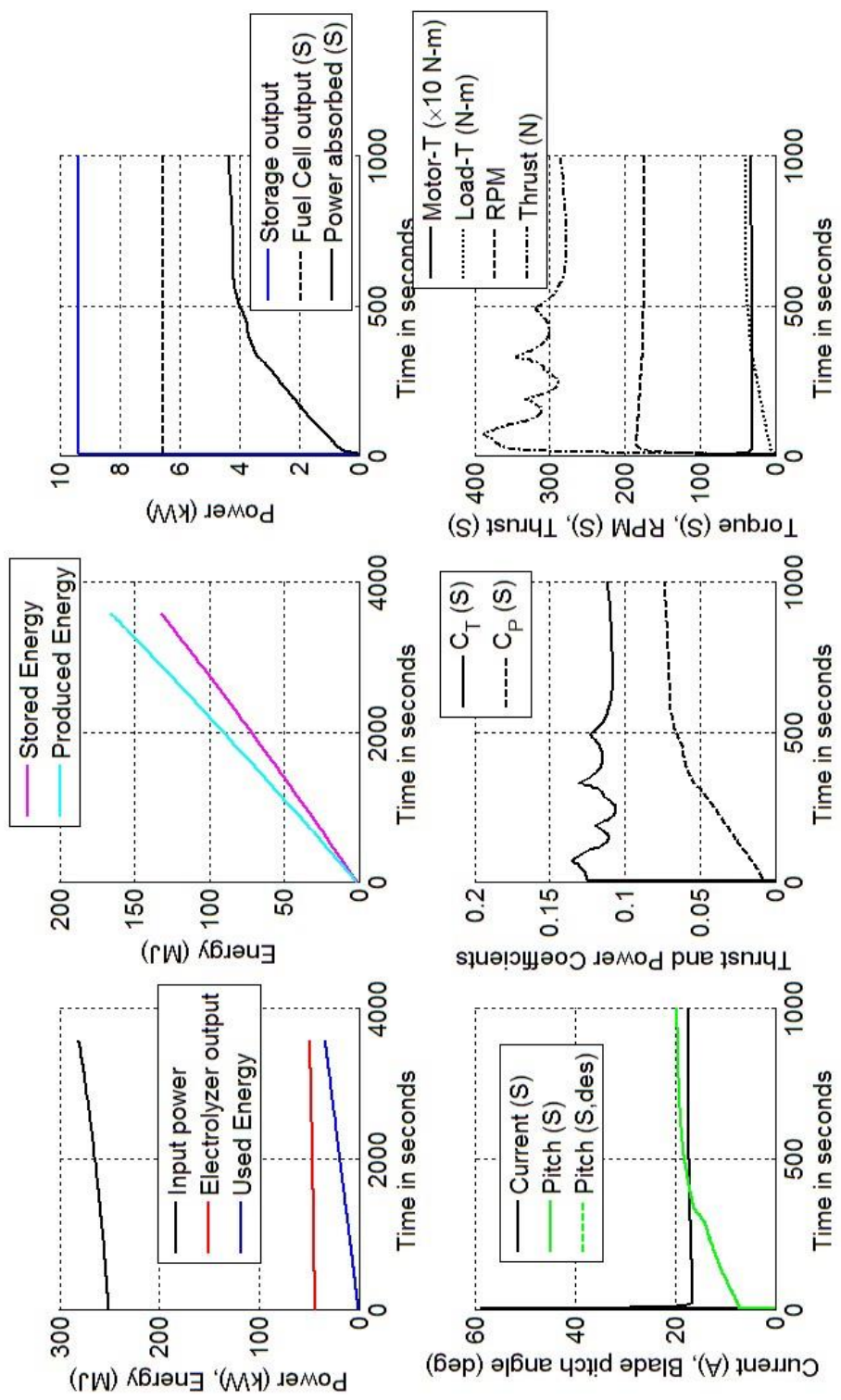


Figure 95: A typical forward motion of the Airship for a throttle command of 0.43 to the smaller-diameter propeller of all the propulsors; power and propulsion system variables.

For closed-loop analysis, the power and propulsion subsystems have not been included and results have been generated for the basic flight dynamics system (Flat-Earth model) of the airship. The control system in closed loop is designed to perform in the presence of wind perturbations. Steady-wind perturbations are generated in NED frame using a simple wind simulation model based on “RAMP” functions as shown in Figure 96.

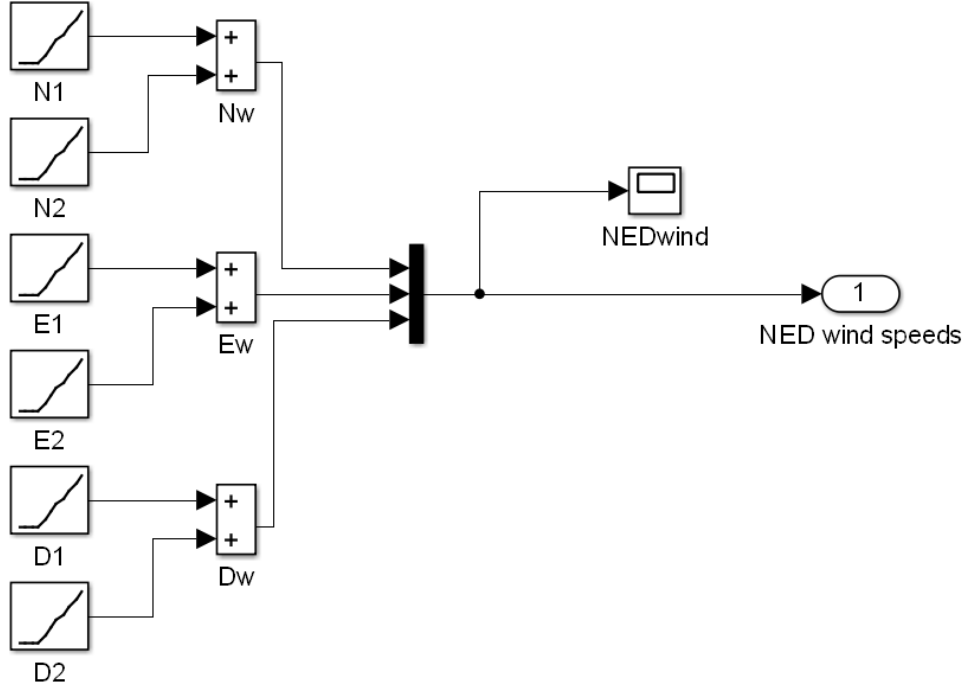


Figure 96: Wind simulation model

The control system developed is shown in Figure 97. It is basically a set of PID-logic systems along different state-to-control feedback pathways. For the closed-loop results reported here, only the top-most (axial velocity, U to thrust) and bottom-most (lateral velocity, V to rudder) blocks are active. Each of the PID-logic control subsystems has a basic structure as shown in Figure 98, with proportional, integral and differential control gains.

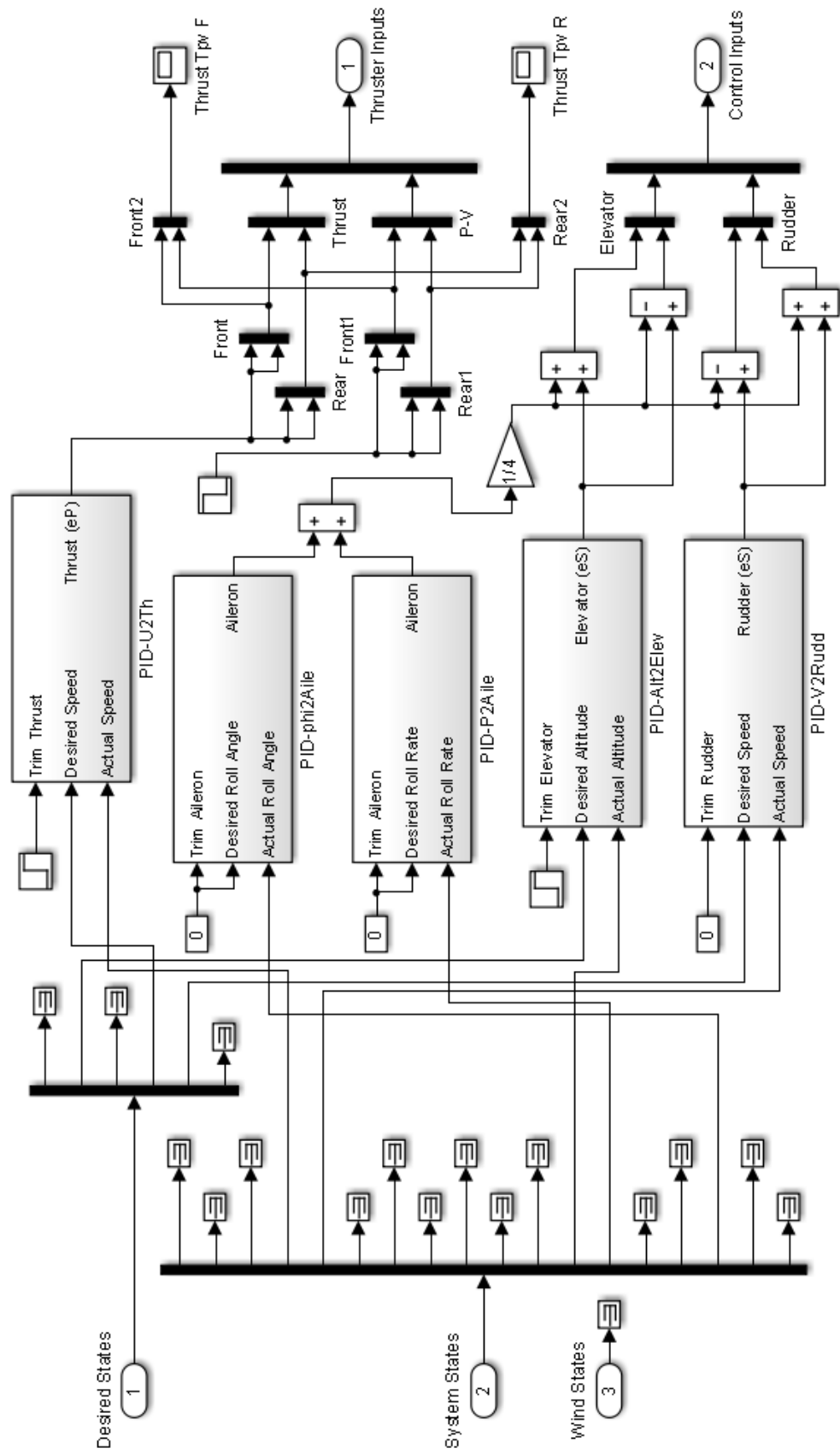


Figure 97: Control system

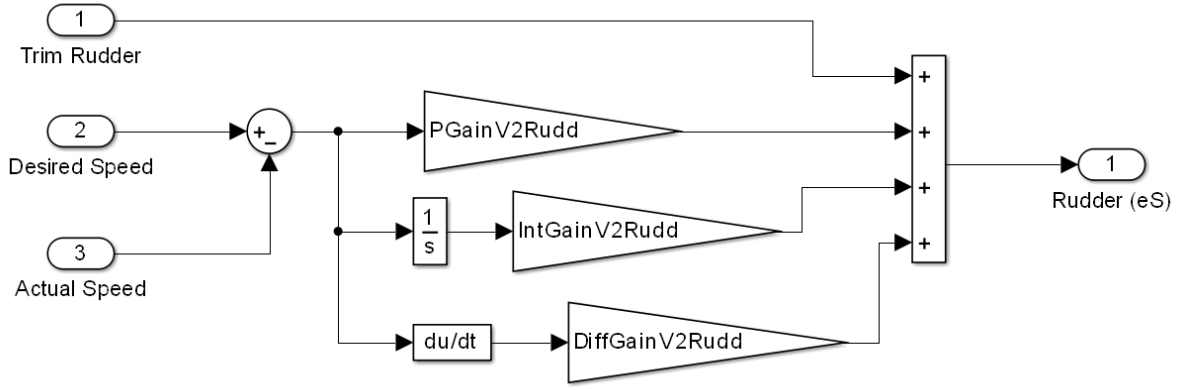


Figure 98: PID control system for lateral velocity control

The closed-loop results are shown in Figure 99 to Figure 101. The nominal trim solution with which the simulation is started corresponds to airspeed of 15 m/s. There is a background wind of speed 15 m/s blowing from East to West. The airship heading ψ is 90 degrees, i.e. it is oriented West to East, and the inertial NED velocity of the airship is zero. Thus the airship is hovering at a position corresponding to 38 degrees latitude and zero longitude at an altitude of 21 km, with its heading oriented towards East. (Trim: Thrust required is 1450 N (4×362.5), pitch-vectoring angle of each thruster is -0.2442 rad, and the elevator deflections, left and right, are 0.0187 rad each.)

Both axial and lateral wind velocity perturbations are given in this simulation starting at time $t = 100$ seconds. The 15 m/s wind blowing from East to West is gradually increased to 20 m/s over a time span of 50 seconds, i.e. until $t = 150$ seconds (-20 m/s along y axis in NED frame). During the same time span, a steady wind of speed 5 m/s develops in the direction from North to South (-5 m/s along x axis in NED frame). The closed-loop system works towards making the airship's axial and lateral inertial velocities zero. In order to make the lateral velocity zero, the closed-loop airship system changes its heading to align itself along the direction of the resultant wind using a maximum transitional rudder deflection of 0.036π rad (6.5 deg). The new heading is $\psi = 0.578\pi$ rad (104.04 deg). Further, zero axial inertial velocity is achieved by increasing the thrust produced by each thruster to around 690 N. At steady state, the new airspeed of the airship matches the net speed (20.6 m/s) of the resultant wind.

During the transition period, there would be a change in latitude and longitude. Once the airship reaches its new steady state, it will hover over the new position. To get back to the original latitude and longitude, an outer position-control loop has to be developed and implemented. For the current results, the various control-gain values are as follows. The axial velocity controller has proportional and integral (PI) control logic with the corresponding gains being 2 and 0.2, respectively. The lateral velocity controller has only proportional (P) control with 0.02 gain value.

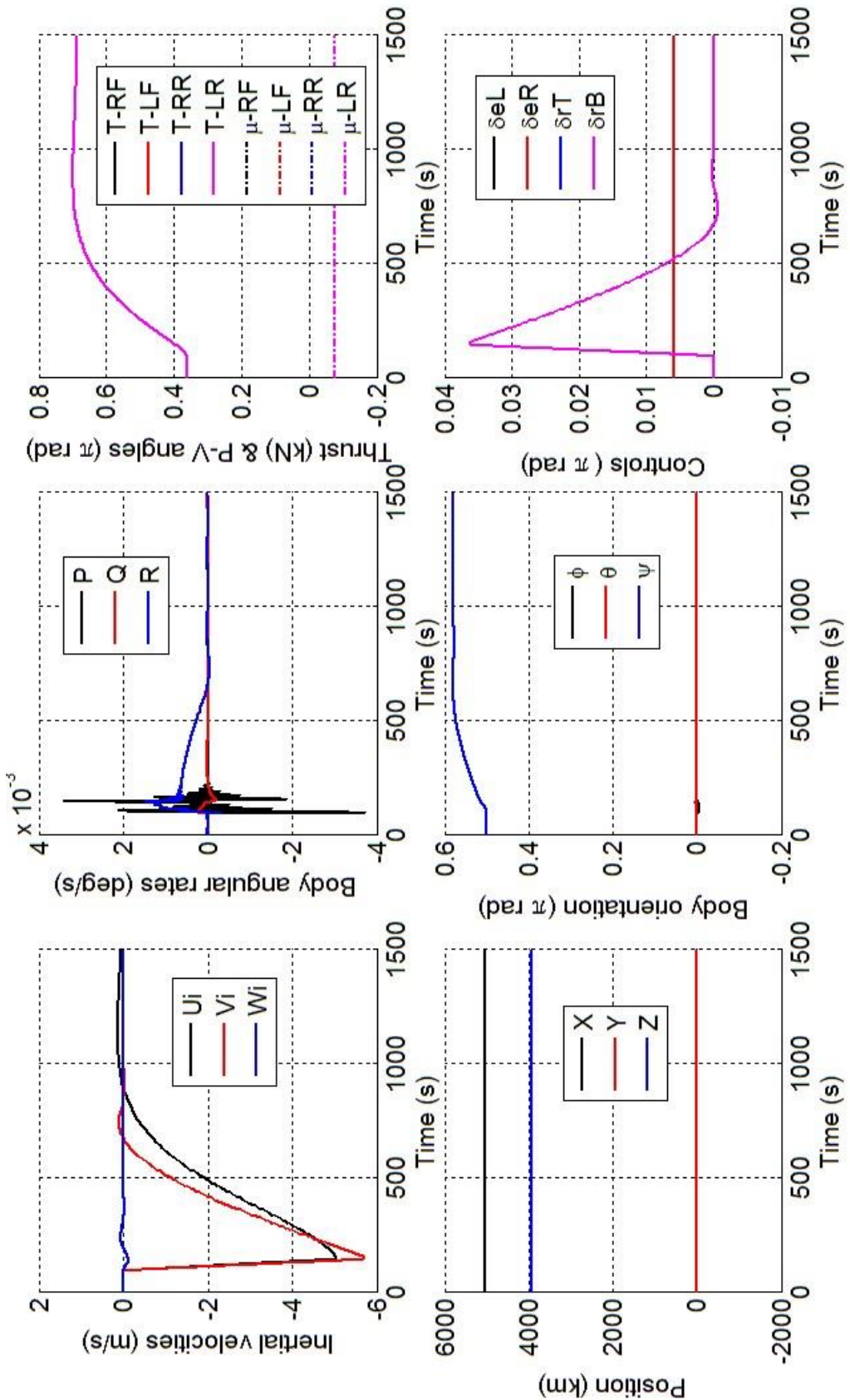


Figure 99: Closed-Loop Flat-Earth airship flight dynamics; results from combined axial and lateral wind velocity perturbations. Euler angles, control actuator angles and thruster pitch-vectoring angle are plotted in terms of π rad.

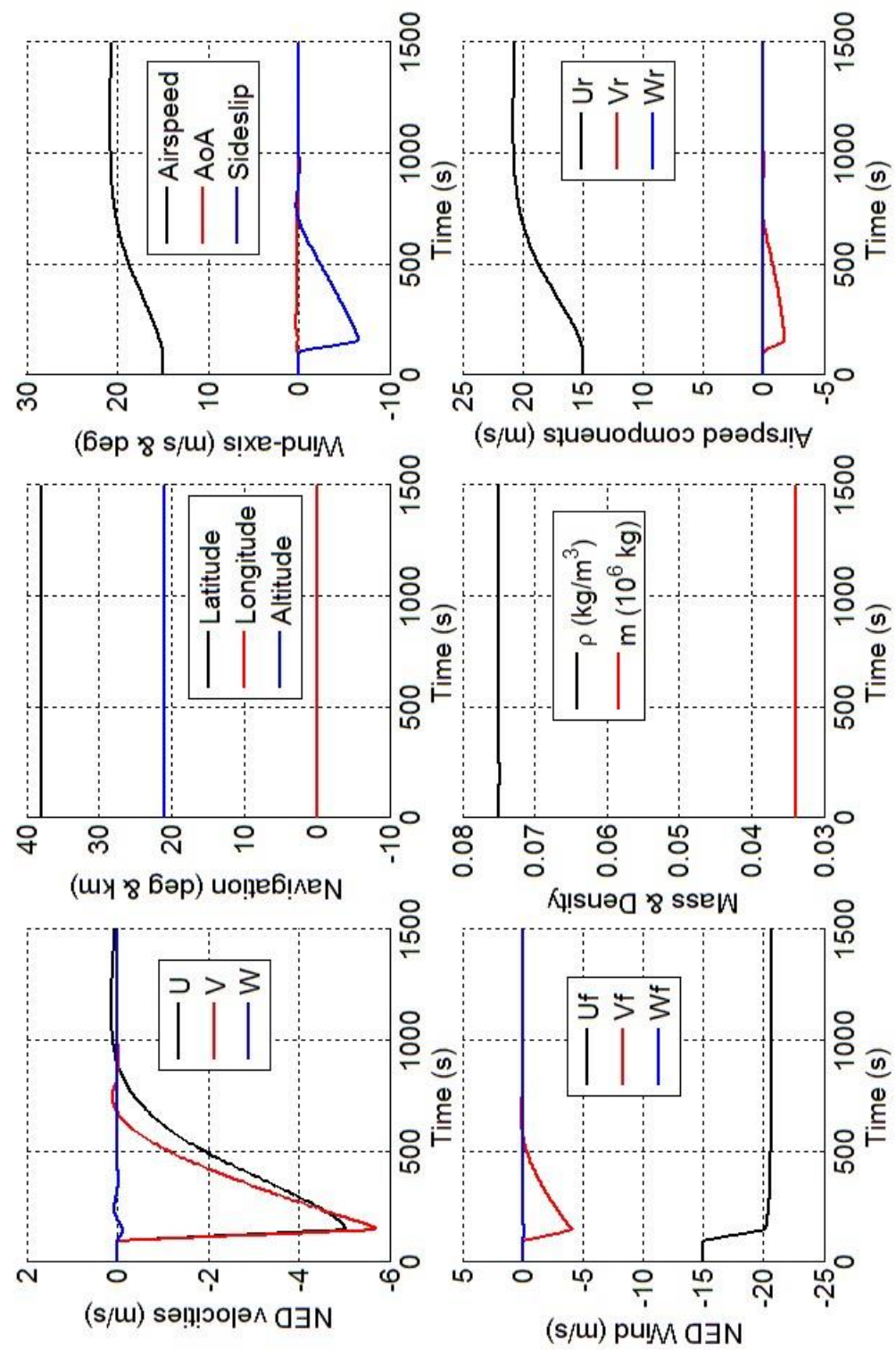


Figure 100: Closed-Loop Flat-Earth airship flight dynamics; results from combined axial and lateral wind velocity perturbations. Airspeed parameters, inertial velocities and navigation variables are shown.

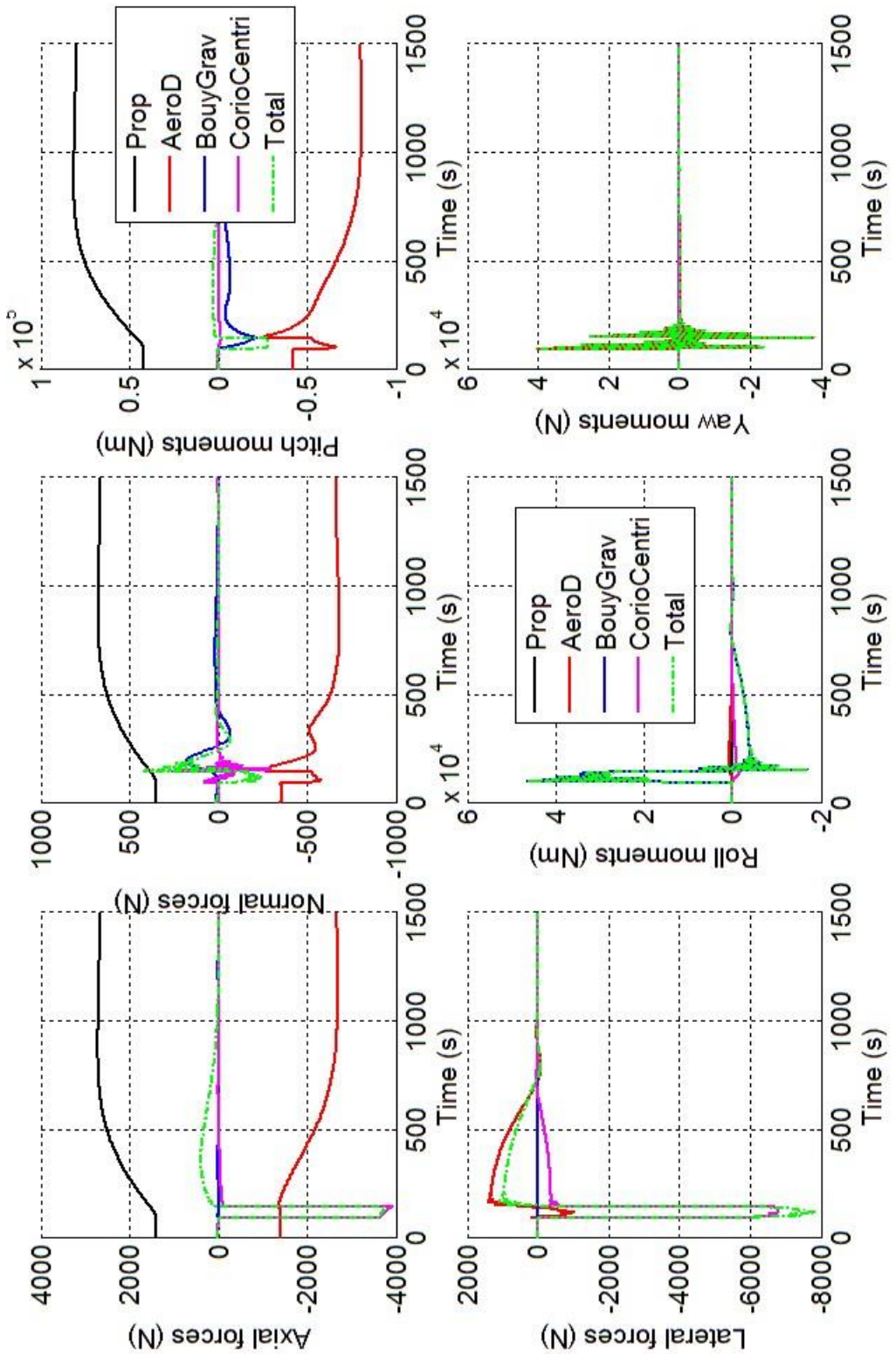


Figure 101: Closed-Loop Flat-Earth airship flight dynamics; results from combined axial and lateral wind velocity perturbations. Different components of the longitudinal, lateral and directional forces and moments are plotted.

In Figure 102 to Figure 104, results from a simulation run of the Open-Loop Geodetic flight dynamics model of the airship are shown. Here the Earth's rotational speed is considered while deriving the airship equations of motion with respect to the Earth-Centered Inertial (ECI) frame. The nominal trim solution is the same as that used for the closed-loop results described above, i.e. the airship hovering at 38° latitude, 0° longitude and 21 km altitude with heading $\psi = 90$ deg and facing a wind of speed 15 m/s. It appears that the open-loop system is unstable which starts with the initial divergence of roll and yaw angular rates.

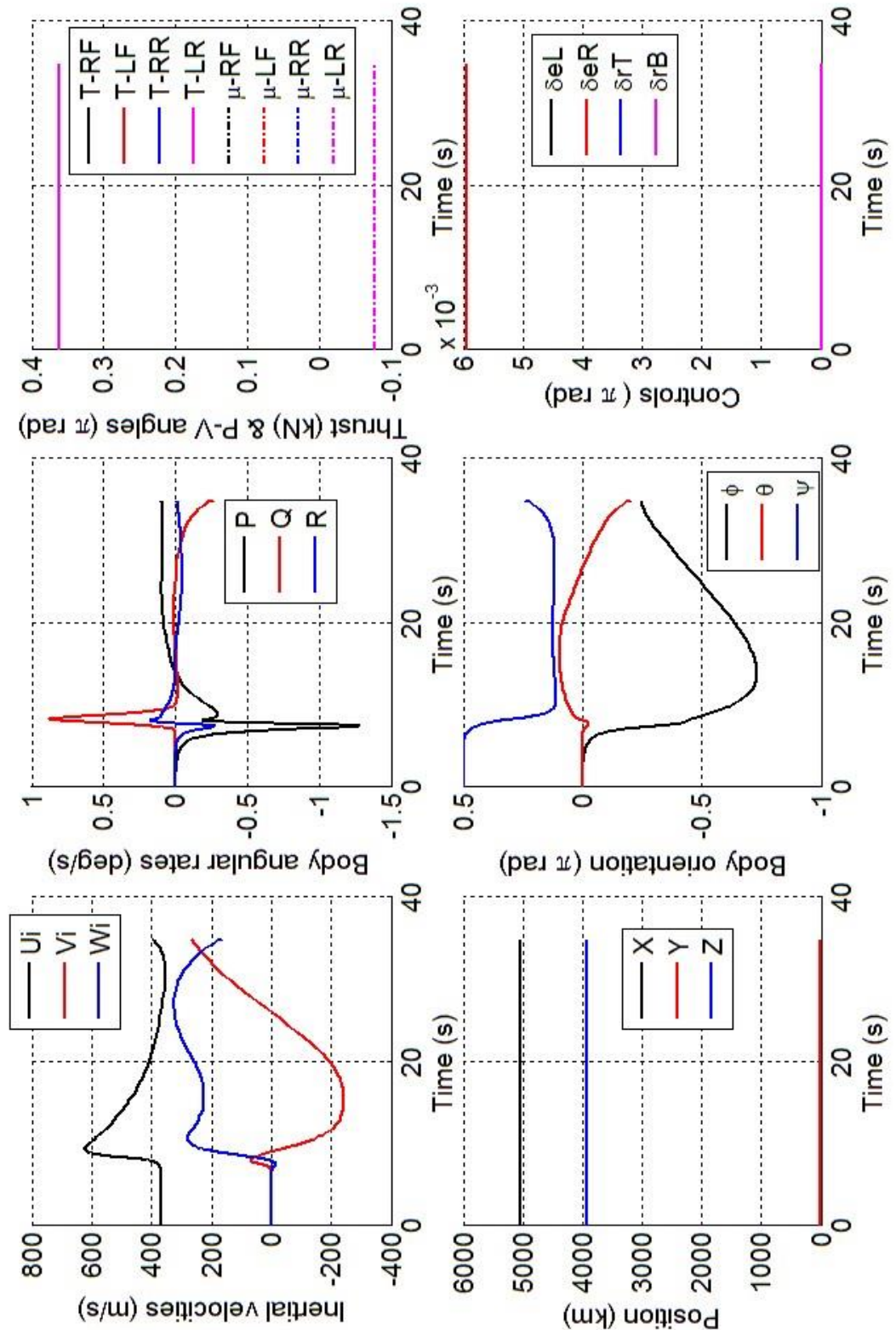


Figure 102: Open-Loop Geodetic flight dynamics of the airship considering Earth's rotational speed. Inertial frame is ECI. Euler angles, control actuator angles and thruster pitch-vectoring angle are plotted in terms of π rad.

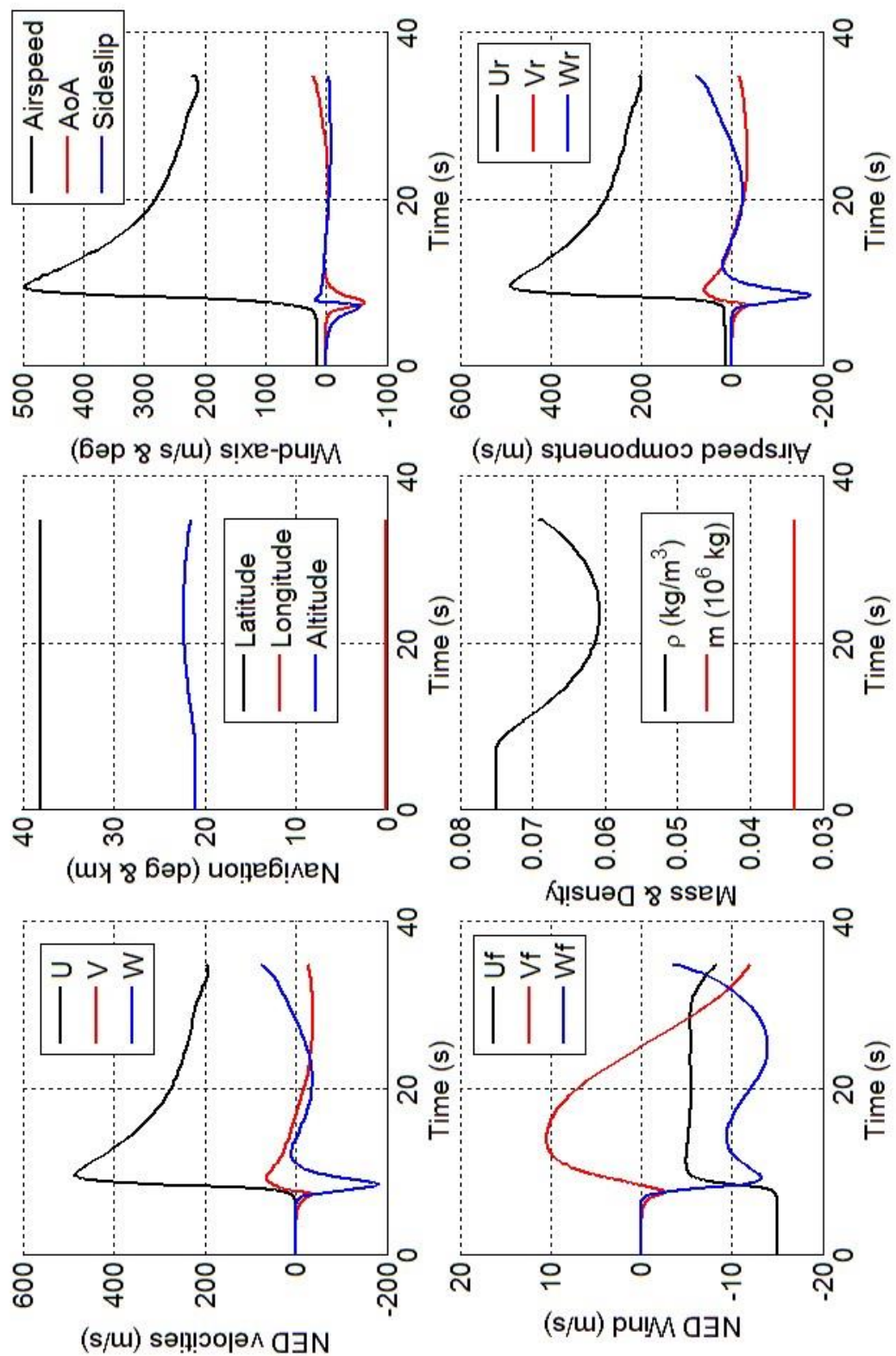


Figure 103: Open-Loop Geodetic flight dynamics of the airship considering Earth's rotational speed. Inertial frame is ECI. Airspeed parameters, inertial velocities and navigation variables are plotted.

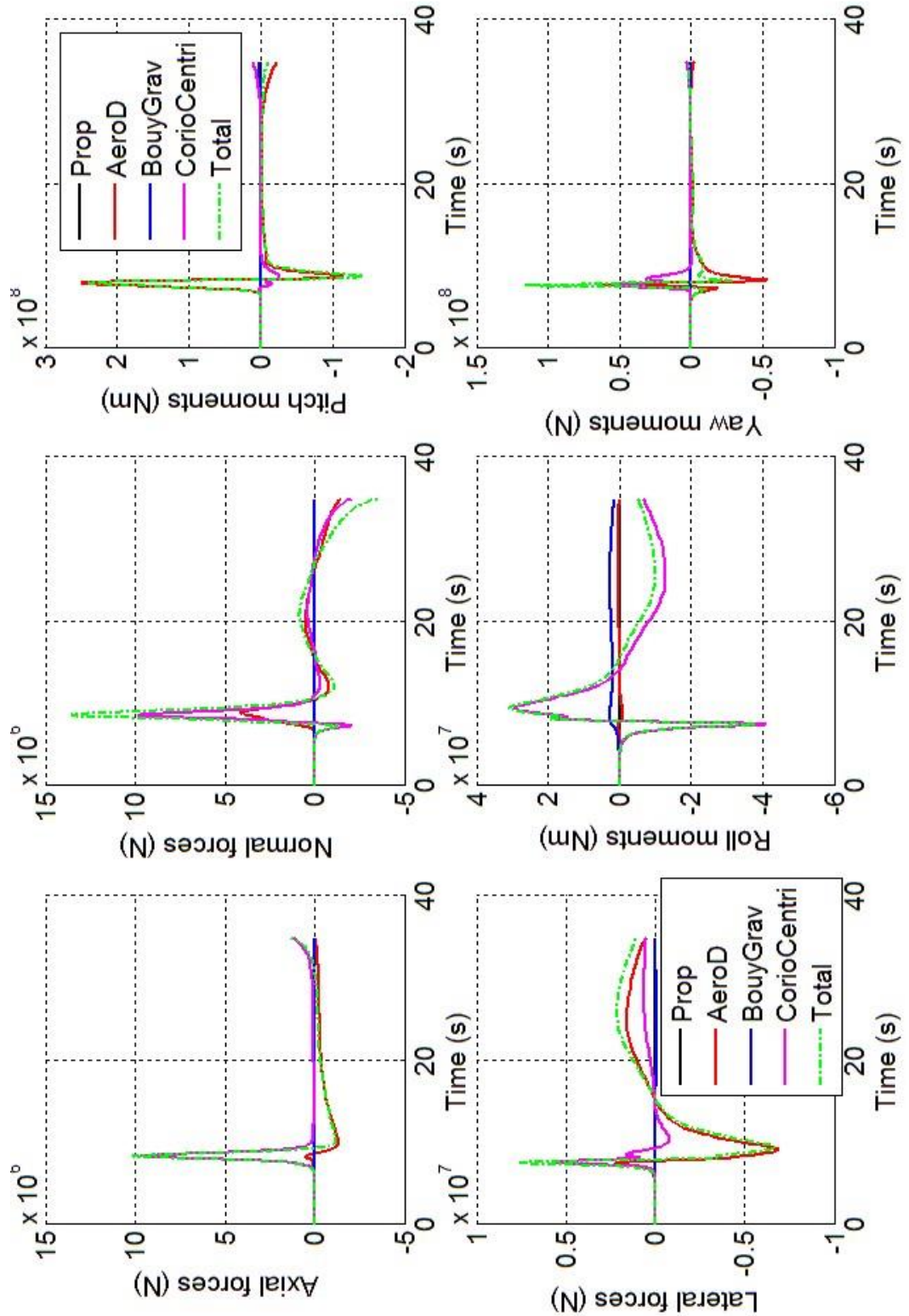


Figure 104: Open-Loop Geodetic flight dynamics of the airship considering Earth's rotational speed. Inertial frame is ECI. Different components of the longitudinal, lateral and directional forces and moments are plotted.

5. Conclusions and Future work

Mathematical models of different components required to develop a system-level dynamic simulation of a High Altitude Airship (HAA) have been identified and studied.

Simulink models of these components have been developed and successfully implemented in the Matlab/Simulink software environment. These subsystems have been integrated to build the three main dynamic components of the HAA system: Power generation, Propulsion system and Flight Dynamics.

Equilibrium solutions or level trims for the Flat-Earth Flight Dynamics model of the airship have been obtained at airship speeds of 15 m/s and 30 m/s. Longitudinal and lateral-directional stability characteristics have been studied by obtaining the Jacobian matrices at these trim conditions.

The power and propulsion subsystems have been integrated with this Flat-Earth flight dynamics subsystem to obtain the full HAA system dynamic model. A typical forward motion of this airship system has been demonstrated for 0.43 throttle command.

A control system has been developed for the Flat-Earth flight dynamics system. It consists of an axial velocity controller and a lateral velocity controller. Closed-loop performance of the airship has been demonstrated for a case in which it recovers from axial and lateral wind perturbations.

A Geodetic Flight Dynamics model of the airship has been developed by including the effect of Earth's rotation and the ellipsoidal shape of the Earth. In this case, the equations of motion are derived with respect to an Earth-Centered Inertial (ECI) frame. Simulation results of this open-loop model show instability in the lateral-directional mode. The Coriolis force that is acting on the airship due to the Earth's rotation seems to be driving force for this instability.

As part of future work, appropriate control logic has to be implemented to stabilize the Geodetic Flight Dynamics model. Subsequently, the power, propulsion, geodetic flight dynamics, and control systems have to be put together to demonstrate a stable hover of the HAA system in the presence of winds with respect to the ECI frame.

6. Appendix

An airship design with a fineness ratio of 4

Dimensions

```
b = 30;
c = b;
a1 = 80;
a2 = 160;
a = (a1 + a2)/2;
Lh = a1 + a2;
xCV = a1 + 3*(a2-a1)/8;
```

Aerodynamics

Drag

```
CDho = 0.025;
CDfo = 0.006; % 25% of hull drag
CDgo = 0.01;
CDch = 0.252;
CDcf = 2.91;
CDcg = 1;
```

Lift

```
cl_alphaaf = 2.3696;
cl_deltaf = 1.24;
```

Geometry

```
Vol = 4*pi*a*b*c/3;
Sh = Vol^(2/3);
Sf = Sh*0.5;
Sg = 202;
df1 = 0.96*Lh - xCV; % From CV, which is the origin
df2 = 1.014*Lh - xCV;
df3 = 16;
dgx = -2.05;
dgz = 33;
```

Hull-Fin interference

```
etaf = 0.6092;
etah = 1.15;
Ione = 0.146;
Ithree = -0.1912;
Jone = 1.80;
Jtwo = 0.79;
```

Damping derivatives

```
CZq = -2;
CYr = -2;
CLp = -1;
CMq = -1;
CNr = -1;
```

Atmosphere

Mean sea level conditions

```
P0 = 101.325;
T0 = 15;
a0 = 340.294;
g0 = 9.80665;
d0 = 1.225;
h0 = 0;
R = 287.04;
```

```

Tropopause
    lambdat = -6.5;
    Tt = -56.5;
    pt = 22.632;
    ht = 11;
Between lower and upper stratosphere
    Ts = -56.5;
    ps = 5.4749;
    lambdas = 1;
    hs = 20;

Buoyancy and Gravity
Acceleration due to gravity
    g = g0;
Mass of fluid displaced
    rho = 0.07488;
% 0.075 (high altitude, 21000 m)
% 0.5 (8425 m)
% d0 (sea level)
    vol = 4*pi*a*b*c/3;
    m_de = rho*vol;
CG and CB positions
    bx = 0;
    bz = 0;
    az = 8;
    ax = 0;

Equations of Motion
Lower off-diagonal terms of Mass and Inertia Matrix, Ma
    Lvdot = 0;
    Mudot = 0;
    Mwdot = 0;
    Nvdot = 0;
Upper off-diagonal terms of Mass and Inertia Matrix, Ma
    Xqdot = 0;
    Ypdot = 0;
    Yrdot = 0;
    Zqdot = 0;
Mass and Inertia
Mass
    m = m_de;
Moment of Inertia
    Ix = 15268140;
% Ix = m * (b^2 + c^2) / 5;
    Iy = 65178400;
% Iy = m * (c^2 + a^2) / 5;
    Iz = 49179000;
% Iz = m * (a^2 + b^2) / 5;
Product of Inertia
    Izx = 31808625;
Added moment of inertia in roll
    Lpdot = 0;
Added product of inertia
    Lrdot = 0;
    Npdot = 0;

Propulsive F&M
Front
    d_fx = 20;
    d_fy = 31;
    d_fz = 31;

```

```

Rear
d_rx = 20;
d_ry = 29;
d_rz = 29;

Earth parameters (fixed)
epsE = 0.0818191908426;
epsEsq = epsE^2;
Requator = 6378137;
% omegaE = 7.29e-5;
omegaE = 0;

Initial conditions
Euler angles
phi0 = 0; Cphi = cos(phi0); Sphi = sin(phi0);
theta0 = 0; Ctheta = cos(theta0); Stheta = sin(theta0);
psi0 = pi/2; Cpsi = cos(psi0); Spsi = sin(psi0);

% Transformation matrix; NED to Body
DCMn2b0mat = [1 0 0; 0 Cphi Sphi; 0 -Sphi Cphi]*...
[Ctheta 0 -Stheta; 0 1 0; Stheta 0 Ctheta]*...
[Cpsi Spsi 0; -Spsi Cpsi 0; 0 0 1];

Quaternions
q0i = cos(phi0/2)*cos(theta0/2)*cos(psi0/2) +
sin(phi0/2)*sin(theta0/2)*sin(psi0/2);
q1i = sin(phi0/2)*cos(theta0/2)*cos(psi0/2) -
cos(phi0/2)*sin(theta0/2)*sin(psi0/2);
q2i = cos(phi0/2)*sin(theta0/2)*cos(psi0/2) +
sin(phi0/2)*cos(theta0/2)*sin(psi0/2);
q3i = cos(phi0/2)*cos(theta0/2)*sin(psi0/2) -
sin(phi0/2)*sin(theta0/2)*cos(psi0/2);

LLA and other Earth parameters
lat0 = 38*pi/180;
Clat = cos(lat0+pi/2); Slat = sin(lat0+pi/2);

latC0 = atan( (1-epsEsq) * tan(lat0) );
long0 = 0;
Clong = cos(long0); Slong = sin(long0);
alt0 = 21000;

Rnorm0 = Requator / sqrt(1 - epsEsq * (sin(lat0))^2);
Rmeri0 = Requator*(1 - epsEsq) / (1 - epsEsq*(sin(lat0))^2) ^ (3/2);
lambda0 = 0;
Clamb = cos(lambda0); Slamb = sin(lambda0);

% Transformation matrix; ECI to NED
DCMi2n0mat = [Clat 0 Slat; 0 1 0; -Slat 0 Clat]*...
[Clong Slong 0; -Slong Clong 0; 0 0 1]*...
[Clamb Slamb 0; -Slamb Clamb 0; 0 0 1];

% Transformation matrix; ECEF to NED
DCMe2n0mat = [Clat 0 Slat; 0 1 0; -Slat 0 Clat]*...
[Clong Slong 0; -Slong Clong 0; 0 0 1];

DCM2b0mat = DCMn2b0mat * DCMi2n0mat;
DCMe2b0mat = DCMe2n0mat * DCMe2n0mat;

```

```

ECEF position
    R0 = Requator / sqrt(1 - epsEsq * (sin(lat0))^2);
    x0 = (R0 + alt0) * cos(lat0) * cos(long0);
    y0 = (R0 + alt0) * cos(lat0) * sin(long0);
    z0 = (R0*(1-epsEsq) + alt0) * sin(lat0);
Air-reference speed's components
    u0 = 0;
    v0 = 0;
    w0 = 0;
    Vr0vec = [u0 v0 w0].';
    p0 = 0;
    q0 = 0;
    r0 = 0;
    omegaNB0vec = [p0 q0 r0].';
Inertial (ECI) speed's components
% Initial wind speed w.r.t. local NED frame has to be considered here
    uf0 = 2;
    vf0 = 0;
    wf0 = 0;
    Vfn0vec = [uf0 vf0 wf0].';
    Vfned0vec = DCMn2b0mat.' * Vfn0vec;

Initial conditions (Vectors)
    rECEF0vec = [x0 y0 z0].';
    omegaIEvec = [0 0 omegaE].';
    Vn0vec = Vfn0vec + Vr0vec;
    Vned0vec = DCMn2b0mat.' * Vn0vec;
    omegaEN0vec = [Vned0vec(2,1)/(Rnorm0 + alt0);
                   -Vned0vec(1,1)/(Rmeri0 + alt0);
                   -Vned0vec(2,1)*tan(lat0)/(Rnorm0 + alt0)];

    Vi0vec = Vn0vec + DCMe2b0mat * cross(omegaIEvec,rECEF0vec);
    ui0 = Vi0vec(1,1);
    vi0 = Vi0vec(2,1);
    wi0 = Vi0vec(3,1);

    omegaIB0vec = omegaNB0vec + DCMi2b0mat*omegaIEvec + DCMn2b0mat*omegaEN0vec;
    pi0 = omegaIB0vec(1,1);
    qi0 = omegaIB0vec(2,1);
    ri0 = omegaIB0vec(3,1);

Control parameters
    LongitudeC = long0;
    LatitudeC = lat0*180/pi;
    AltitudeC = alt0;
    HeadingC = psi0*180/pi;

Solar radiation and PV arrays
    rorbm = 1.4960e+11;
    epsilon = 0.017;
    SIm = 1352;
    daynumber = 172;
    phiE = 38*pi/180;
    gammaE = 0.98*(daynumber-1)*pi/180;
    tau = 0.15;
% Declination angle (NH)
    dele = asin(sind(23.45)*sind(360*(daynumber-81)/365));
    riseT = 12 - acosd(-tan(phiE)*tan(dele))/15;
    riseT = round(riseT*100)/100;

```

```

Solar PV - Colozza data
% Cylindrical geometry
lsc = 150; % Length of each solar strip
b = 30; % Maximum hull radius
dbeta = 0.01; % Width of each solar strip
eta_sc = 0.1; % Solar cell efficiency

Solar PV - Air-mass and Altitude effects
Q = 10340;
rhosL = 1.225;
c3 = -0.11159;
c2 = 0.71537;
c1 = -1.45854;
c0 = 0.99523;
dc = 15892;

Storage and Propulsor subsystem
% basic constants
gasconst = 1.4;
R = 287.04;
TinK = 216.5;
% small propeller and motor
% motor parameters
InductanceS = 0.1;
ResistanceS = 1.7;
KbS = 3.22;
KtS = 18.11;
gearRS = 6;
% propeller parameters
diaPropsmall = 8;
JpropmotorS = 25;
bpropmotorS = 2.5;
tausPphi = 0.5;
% large propeller and motor
% motor parameters
InductanceL = 0.2;
ResistanceL = 1.7;
KbL = 0.9045;
KtL = 6.564;
gearRL = 5.5;
% propeller parameters
diaProplarge = 12;
JpropmotorL = 70;
bpropmotorL = 5;
tauLPphi = 0.7;

Initial conditions
% storage system
initPenergy = 500;
initUenergy = 0;
% small propeller and motor
initSParmCur = 0;
initSPradps = 0;
initSPBpitch = 0;
% large propeller and motor
initLParmCur = 0;
initLPradps = 0;
initLPBpitch = 0;

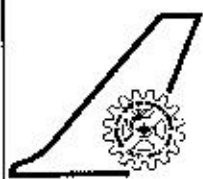
```

7. References

- [1] Kukillaya, R.P., “Mathematical models for system simulation of High Altitude Airship (HAA)”, PD-FMC/2015/1000, National Aerospace Laboratories (NAL), 2015.
- [2] Mueller, J. B., Paluszek, M. A., and Zhao, Y., “Development of an aerodynamic model and control law design for a high altitude airship,” AIAA Unmanned Unlimited Conference, Chicago, IL, US, September 2004.
- [3] Lamb, H., “The inertia coefficients of an ellipsoid moving in fluid,” British Aeronautical Research Committee Report and Memoranda, No. 623, October 1918.
- [4] Khoury, G. A. and Gillett, J. D., Airship Technology, Cambridge Aerospace Series: 10, 1999.
- [5] Gomes, S. B. V. and Ramos, J. Jr. G, “Airship dynamic modeling for autonomous operation,” IEEE International Conference on Robotics and Automation, Leuven, Belgium, May 1998.
- [6] Jones, S. P. and DeLaurier, J. D., “Aerodynamic estimation techniques for aerostats and airships,” AIAA Lighter-than-Air Systems Conference, Annapolis, MD, 1981.
- [7] Tuckerman, L. B., “Inertia factors of ellipsoids for use in airship design,” NACA, Report no. 210, 1926.
- [8] Lamb, H., Hydrodynamics, Dover, New York, 6th ed., 1945.
- [9] Milne-Thomson, L. M., Theoretical Hydrodynamics, Macmillan & Co, London, 4th ed., 1962.
- [10] Imlay, F. H., “The complete expressions for ‘added mass’ of a rigid body moving in an ideal fluid,” Report 1528, David Taylor Model Basin (DTMB), Bethesda, MD, 1961.
- [11] Perrault, D., Bose, N., O’Young, S., and Williams, C. D., “Sensitivity of AUV added mass coefficients to variations in hull and control plane geometry,” Ocean Engineering, Vol. 30, pp. 645–671, 2003.
- [12] Bateman, H., “The inertia coefficients of an airship in a frictionless fluid,” NACA, Report No. 164, 1923.
- [13] Azouz, N., Chaabani, S., Lerbet, J., and Abichou, A., “Computation of the added masses of an unconventional airship,” Journal of Applied Mathematics, Hindawi Publishing Corporation, Article ID 714627, 2012.
- [14] Munk, M. M., “The aerodynamics forces on airship hulls,” NACA, Report No. 184, 1924.
- [15] Munk, M. M., “Aerodynamics of airships,” Aerodynamics Theory, Vol. 6, Julius Springer, Berlin, 1936.
- [16] Thomasson, P. G., “Motion of a rigid body in an unsteady non-uniform heavy fluid,” College of Aeronautics, Report No. 9501, 1995.
- [17] Thomasson, P. G., “Motion of a rigid body in an unsteady non-uniform heavy fluid; an extension,” College of Aeronautics, Report No. 9610, 1996.
- [18] Thomasson, P. G., “Equations of motion of a vehicle in a moving fluid,” Journal of Aircraft, Vol. 37, No. 4, pp. 630-639, 2000.
- [19] Azinheira, R. J., de Paiva, E. C., and Bueno, S. S., “Influence of wind speed on airship dynamics,” Journal of Guidance, Control and Dynamics, Vol. 25, No. 6, pp. 1116-1124, 2002.

- [20] Colozza, A., "Initial feasibility assessment of a high altitude long endurance airship," NASA, CR-2003-212724, December 2003.
- [21] Colozza, A., "High altitude propeller design and analysis overview," NASA, CR-1998-208520, March 1998.
- [22] Colozza, A. J. and Maloney, T., "Initial design and construction of a mobile regenerative fuel cell system," NASA, CR-2003-212539, September 2003.
- [23] Reinhardt, K. C., Lamp, T. R., Geis, J. W., and Colozza, A. J., "Solar-powered unmanned aerial vehicles," Proceedings of the 31st Intersociety Energy Conversion Engineering Conference (IECEC), Vol. 1, pp. 41–46, IEEE, 1996.
- [24] Petrone, F. J. and Wessel, P. R., "High Altitude Super-pressured Powered Aerostat (HASPA)," Naval Ordnance Lab, 8th AFCRL Scientific Balloon Symposium, Hyannis, MA, Sep-Oct 1974, pp. 9-39.
- [25] Dunlap, P. H. Jr., Daniels, C. C., Wasowski, J. L., Garafolo, N. G., Penney, N., and Steinetz, B. M., "Pressure decay testing methodology for quantifying leak rates of full-scale docking system seals," NASA, TM – 216244, 2010.
- [26] Noll, J. R., "Determination of lift gas leakage rate for a stratospheric airship hull," 11th AIAA Aviation Technology, Integration, and Operations (ATIO) Conference, AIAA 2011 – 6995, Virginia Beach, VA, September 2011.
- [27] U. S. Military Handbook, MIL-HDBK-1797, December 1997.
- [28] Justus, C. G., Campbell, C. W., Doubleday, M. K., and Johnson, D. L., "New atmospheric turbulence model for shuttle applications," NASA, TM – 4168, 1990.
- [29] Azinheira, J. R., Paiva, E., Ramos, J. J. G., Bueno, S. S., and Bergerman, M., "Extended dynamic model for AURORA robotic airship," AIAA Lighter-Than-Air Technology Conference, Akron, 2001.
- [30] Richardson, J. R., "Quantifying and scaling airplane performance in turbulence," Ph.D. Thesis, University of Michigan, 2013.
- [31] Gawale, A. C., Raina, A. A., Pant, R. S., and Jahagirdar, Y. P., "Design, fabrication and operation of remotely controlled airships in India," 18th AIAA Lighter-Than-Air Systems Technology Conference, AIAA 2009 – 2855, Seattle, Washington, May 2009.
- [32] Modica, G. D., Nehrkorn, T., and Meyers, T., "An investigation of stratospheric winds in support of the High Altitude Airship," 13th Conference on Aviation Range and Aerospace Meteorology, Poster presentation, New Orleans, LA, January 2008.
- [33] Christensen, R., Fogh, N., Cour-Harbo, A., and Bisgaard, M., "Inertial navigation system," Master's Thesis, Aalborg University, Denmark, 2008.
- [34] Li, Y., Nahon, M., and Sharf, I., "Dynamic modeling and simulation of flexible airships," AIAA Journal, Vol. 47, No. 3, March 2009.
- [35] Gottlieb, I. M., Electric motors and control techniques, TAB Books, 1994.
- [36] Li, Y., Nahon, M., and Sharf, I., "Airship dynamics modeling: A literature review," Progress in Aerospace Sciences, Vol. 47, pp. 217-239, 2011.
- [37] Kraska, M., "Structural analysis of the CL-160 airship," 14th AIAA Lighter-than-air Technical Committee Convention and Exhibition, Akron, OH, July 15-19, 2001.
- [38] Chen, W. J., Xiao, W. W., Kroplin, B., and Kunze, A., "Structural performance evaluation procedure for large flexible airship of HALE stratospheric platform conception," Journal of Shanghai Jiatong University, Vol. E-12(2), 293-300, 2007.

- [39] Burgess, C. P., *Airship Design*, The Ronald Press Company, 1927, pp. 109-152.
- [40] Talay, T. A., "Introduction to the aerodynamics of flight," NASA SP-367, National Aeronautics and Space Administration, Washington, D.C., 1975, pp. 6-9.
- [41] Manual of the ICAO standard atmosphere, International Civil Aviation Organization, Doc 7488/3, 3rd edition, 1993.
- [42] Getting to grips with aircraft performance, Airbus, Customer Services, January 2002.
- [43] Strganac, T. W., "Wind study for high altitude platform design," NASA Reference Publication 1044, National Aeronautics and Space Administration, December 1979.
- [44] Selig, M. S., Donovan, J. F., and Fraser, D. B., *Airfoils at Low Speeds*, Soartech 8, H. A. Stokely Publisher, 1989.
- [45] Britting, K. R., *Inertial Navigation Systems Analysis*, John Wiley & Sons, 1971.
- [46] Rogers, R. M., *Applied Mathematics in Integrated Navigation Systems*, AIAA Education Series, 3rd edition, 2007.
- [47] Li, Y., and Nahon, M., "Modeling and simulation of airship dynamics," *Journal of Guidance, Control, and Dynamics*, Vol. 30, No. 6, 2007, pp. 1691-1700.
- [48] Meirovitch, L., and Tuzcu, I., "Unified theory for the dynamics and control of maneuvering flexible aircraft," *AIAA Journal*, Vol. 42, No. 4, 2004, pp. 714-727.
- [49] Main, J. A., Perterson, S. W., and Strauss, A. M., "Load-deflection behavior of space-based inflatable fabric beams," *Journal of Aerospace Engineering*, Vol. 7, No. 2, 1994, pp. 225-238.
- [50] McTavish, D. J., and Davidson, K., "Practical large-motion modeling of geometrically complex flexible vehicles," *47th AIAA/ASME/ASCE/AHS/ASC Structures, Structural Dynamics, and Materials Conference*, AIAA, Reston, VA, May 1-4, 2006.
- [51] Damaren, C., and Sharf, I., "Simulation of flexible-link manipulators with inertial and geometric nonlinearities," *Journal of Dynamic Systems, Measurement, and Control*, Vol. 117, No. 1, 1995, pp. 74-87.
- [52] Li, Y., "Dynamics modelling and simulation of flexible airships," Ph.D. Thesis, McGill Univ., Montreal, Jan. 2008.

DOCUMENTATION SHEET**National
Aerospace
Laboratories**Class: Unrestricted
No. Copies: 8**Title:** Simulink model development, validation and analysis of high altitude airship**Authors:** Raghavendra Kukillaya, Abhay Pashikar**Division:** FMC **Project No:** D-1-164**Document No:** PD-FMC/2017/1000 **Date of Issue:** March 2017**Contents:** Pages: 128 **Figures:** 104 **Tables:** 7 **References:** 52**External Participation :** NIL**Sponsor :** AR&DB**Approval :** Head, FMC*Tatinder Singh***Remarks :****Keywords :** High altitude airship, system modeling, system simulation, station keeping

Abstract : This report describes the design and development of the Matlab/Simulink model of the high altitude airship. The model consists of sub-system models of the airship hull geometry, aerostatics, aerodynamics, apparent mass and inertia, equations of motion in the Earth-Centered Inertial (ECI) frame, solar radiation, atmosphere, wind and turbulence, power and propulsion system (consisting of electrolyser, storage, fuel cell, motor and propeller dynamics). These models have been individually validated and integrated into a system model of the high altitude airship. The integrated model is then used for simulation of station keeping against wind disturbances.